Machine Learning for Composite Material Analysis and Optimization

by

Haotian Feng

A dissertation submitted in partial fulfillment of
the requirements for the degree of

Doctor of Philosophy

(Mechanical Engineering)

at the

UNIVERSITY OF WISCONSIN–MADISON

2023

Date of final oral examination: 05/04/2023

The dissertation is approved by the following members of the Final Oral Committee:

Pavana Prabhakar, Associate Professor, Mechanical Engineering
Yingyu Liang, Assistant Professor, Computer Sciences
Tim Osswald, Professor, Mechanical Engineering
Shiva Rudraraju, Assistant Professor, Mechanical Engineering
Krishnan Suresh, Professor, Mechanical Engineering

To my mom and dad, June Cui and Wenliang Feng, for their unwavering support and for instilling in me the values of hard work and dedication. Your love and encouragement have been a constant source of strength throughout my academic journey, and I am forever thankful for everything you have done for me.

To my maternal grandmother, Chanyu Li, who raised me and protected me in my childhood. Although she cannot join me for my PhD graduation due to her advanced age, her influence and love have shaped me into the person I am today.

To my paternal grandparents, Xiying Li and Jinyu Feng, and maternal grandpa, Tingfu Cui, who have all passed away but whose love and support have been a vital part of my journey, Though they are no longer with me, I hope this accomplishment serves as a testament to their impact on my life.

To all my family members and everyone who help and support during my whole journey, I could not have achieved this milestone without all of you.

ACKNOWLEDGMENTS

I would like to express my gratitude to several individuals who have provided invaluable support and guidance throughout my doctoral studies.

First and foremost, I would like to thank my advisor Dr. Pavana Prabhakar, for her unwavering support, encouragement, and guidance. Her expertise, enthusiasm, and willingness to provide constructive feedback have been instrumental in shaping my research and ensuring its success.

I would also like to thank my committee members Dr. Tim Osswald, Dr. Suresh Krishnan, Dr. Shiva Rudraraju and Dr. Yingyu Liang, for their invaluable feedback, suggestions, and constructive criticism, which have helped me refine my research and strengthen my arguments.

My sincere thanks also go to my lab mates Sabarinathan P. Subramaniyan, Hridyesh Tewani, Guanjin Yan and Vinay Damodaran for their constant support, collaborations and encouragements. Their enthusiasm, insight, and friendship have made my doctoral journey a truly enjoyable and fulfilling experience.

Finally, I am extremely grateful to my family and my girlfriend, for their unconditional love, unwavering support, and unwavering faith in my abilities. Their encouragement, patience, and understanding have been my pillars of strength throughout my doctoral journey.

Thank you all for your support, encouragement, and guidance. I am truly grateful for your help and could not have accomplished this without you.

— Haotian Feng (2023)

CONTENTS

LIST OF TABLES

LIST OF FIGURES

ABSTRACT

My PhD research aims to develop Machine Learning methods for the analysis and optimization of composite materials. Specifically, I focus on two key areas: composite material property prediction and composite material optimization. To enhance the accuracy of Machine Learning models in composite material prediction, I explore the incorporation of practical knowledge into the Machine Learning framework, which can be achieved through various approaches such as input layer, Neural Network, or loss function. My research demonstrates that incorporating existing knowledge can improve the prediction accuracy of Machine Learning models, which can be applied to both data-based and function-based machine learning problems. In addition to prediction, I also investigate optimization strategies for discovering optimal composite material designs using Machine Learning. These findings highlight the great potential of Machine Learning in composite material analysis and offer insights for future research in other applications such as medical image analysis, time-series data analysis, and image segmentation and classification.

1 INTRODUCTION

Composite materials are hybrid materials created by combining two or more constituent materials with different physical or chemical properties, resulting in a material with unique properties. They are widely used in structural applications across various industries, including aerospace, defense, automotive, and marine. Typically, these materials consist of stiff and strong reinforcements at the micron scale bound together by a softer polymer matrix material. They provide design flexibility, as the orientation and mixture of reinforcements can be customized for specific applications. However, modeling these materials computationally is challenging due to the presence of multiple materials and features at the micrometer scale that exhibit multi-scale behaviors. Micro-mechanical models, such as repeated unit cell (RUC) models, are often used in composite analysis, and the Finite Element Method (FEM) is commonly employed to analyze these RUCs. However, FEM can be computationally expensive when used for multi-scaling or optimization, where several models need to be solved iteratively. Therefore, my PhD research focuses on using Machine Learning techniques to predict composite material properties and responses without having to perform FEM analysis with varying input parameters.

Machine Learning is a field of study that focuses on computer algorithms that can improve automatically through experience and data. These algorithms are built based on training data and can make predictions without explicit programming. Regression analysis, which is a statistical approach for estimating relationships between dependent and independent variables, is a widely used Machine Learning algorithm in composite material analysis. With regression analysis, we can build the connection between input features and corresponding mechanical properties. However, in many cases, the target model in composite material analysis is not easily described by a simple feature vector. In such cases, we can use Deep Learn-

ing, which is a family of machine learning methods based on artificial neural networks with multiple layers to extract a large number of features and make predictions based on these features.

Therefore, my research focuses on analyzing composite materials using Machine Learning, with a focus on making predictions and optimizing designs using Knowledge-based Machine Learning. Knowledge-based Machine Learning refers to Machine Learning or Deep Learning frameworks that incorporate our existing knowledge for providing better prediction accuracy or requiring less training data. Each composite material model can be treated as a graphical matrix, where we utilize Convolutional Neural Network (CNN) to extract high level features from each model and predict corresponding mechanical properties or discovering optimal geometric parameters.

2 OVERVIEW

The diagram in Figure 2.1 summarizes the research framework of this study, which mainly focuses on prediction and optimization problems related to composite materials. Due to limited available data, especially in engineering, it is essential to embed existing knowledge into Machine Learning algorithms to achieve better predictions with less data. To address this challenge, two groups of prediction problems were identified: data-based and function-based prediction. The former relies on experimental or computational data, while the latter relies on governing equations. To embed knowledge into these approaches, various methods were explored, such as input-based, Neural Network-based, and output-based embedding.

In terms of optimizing problems, the research focuses on finding the optimal design among a large number of design variations. To efficiently achieve this goal, the study explores two main approaches: physically-meaningful optimization and data-driven optimization. Physically-meaningful optimization aims to establish the relationship between physically meaningful features and the target variables through statistical learning. This relationship serves as the governing equation to discover the optimal solution. On the other hand, data-driven optimization seeks to identify the optimal design through heuristic searching or reinforcement learning methods.

2.1 Prediction problem

The prediction problem mainly consists of predicting the mechanical properties from targeting composite material geometries (forward-direction prediction) or predicting composite material geometries from targeting mechanical properties (inverse-direction prediction).

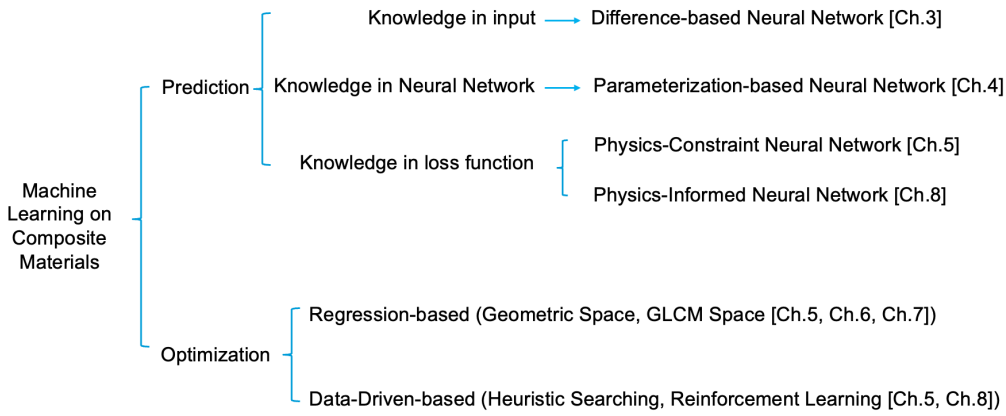

Figure 2.1: Overview of PhD research framework

Knowledge in input - Difference-based Neural Network (DiNN)[Chapter 3]

We proposed the Difference-based Neural Network (DiNN)[31] for predicting stress distributions in different composite micromechanical models by embedding knowledge in the input layer. Our approach takes the average of the geometric matrix and corresponding stress contour in the training dataset as our 'reference model'. The Deep Neural Network focuses on predicting the difference between the target model and reference model. Our results demonstrate that DiNN can significantly improve stress contour prediction accuracy, particularly for RUCs with simple geometric changes, such as changing reinforcement diameter or thickness, and with limited dataset. However, this method has limitations when the RUCs undergo significant changes, as it may restrict the model variance. To overcome this limitation, we used an Autoencoder framework to reduce the dimensionality of input models and predict stress distributions for models with large variances. Our results show that this approach enhances prediction accuracy, especially when the training data is limited.

Knowledge in Neural Network - Parameterization-based Neural Network [Chapter 4]

Besides embedding knowledge in the input layer and using dimension reduction techniques, my research also investigates methods to incorporate knowledge within the Neural Network. In predicting stress-strain curves, we propose a framework called Parameterization-based Neural Network (PBNN)[34], which predicts nonlinear stress-strain curves described as a parameterized function. Since the function parameters are nonlinearly related to each point on the curve, the predicted parameters may capture the shape of the function, but not the precise location. To improve prediction accuracy, PBNN includes an additional prediction to guide the predicted nonlinear stress-strain curve, as the knowledge embedded within the Neural Network. Our research demonstrates that PBNN produces smoother and more accurate stress-strain curves.

Knowledge in loss function - Physics-Constraint Neural Network and Physics-informed Neural Network

Physics-Constraint Neural Network [Chapter 5] In addition to embedding knowledge in the input layer and within the Neural Network, we also investigate embedding knowledge in the loss function to improve the prediction. Specifically, we propose the Physics-Constraint Neural Network (PCNN)[35], which embeds physics knowledge in the loss function. This approach is used to predict woven composite geometry based on targeting mechanical properties. Our results demonstrate that PCNN significantly improves the prediction accuracy of woven architecture for a specified composite modulus, which is a difficult prediction to make for woven composites when compared to existing methods.

Physics-informed Neural Network Data-driven modeling methods heavily rely on the input models, meaning that they cannot be generalized to unseen composite materials or unseen boundary conditions. To overcome this limitation, my research also focuses on function-based prediction, which considers the fundamental boundary value problem (BVP) that is usually defined as a Partial Differential Equation (PDE). My research aims at developing more robust Physics-informed Neural Network to: (1) solve the heterogeneous Poisson equation and (2) discover hidden parameters in the heterogeneous Poisson equation from experimentally measured data.

2.2 Optimization problem

Regarding optimization problems, my research is concentrated on two distinct approaches: regression-based and data-driven-based optimization.

Regression-based Optimization

Directional Origami Structures - Geometric Regression Analysis [Chapter 6] Origami structures are a fascinating class of structures that offer flexibility in modifying their mechanical properties through the choice of different geometric parameters. In contrast to origami structures made of isotropic material, our research focuses on origami structures made of directional materials, such as Carbon Fiber Reinforced Composites (CFRC). These structures have multiple parameters that govern the shape of their unit cells and folding angles. Our aim is to investigate the effect of geometric parameters and CFRC directionality on the mechanical properties of the origami structures and identify optimal geometric designs. To achieve this, we employ regression analysis to identify the relationship between each geometric parameter and the mechanical properties. Subsequently,

the regression model can be used as a governing equation to determine the optimal geometric parameters[36].

Syntactic Foam Densification Mechanics [Chapter 7] The method of optimization based on regression can also be extended to solve the optimization problem for syntactic foam composites. Syntactic foams consist of closed cell composite foams, where microballoons with thin walls are dispersed within a matrix (resin) to provide exceptional mechanical properties, such as high strength and low density. This study considers various parameters that govern the geometry of syntactic foams, and aims to find the optimal design using the regression model[109].

Data-Driven-based Optimization [Chapter 8]

In addition to using regression-based analytical optimization, my research also investigates the use of data-driven methods to discover optimal solutions. The effectiveness of regression analysis is largely dependent on the choice of model. A model that is too simplistic may not capture the true relationship, while a model that is too complex may lead to overfitting. As a result, my research examines the application of data-driven methods to identify optimal solutions. To illustrate, my work employs genetic algorithm and deep reinforcement learning techniques to discover optimal designs for composite materials[33].

2.3 Structure of the Dissertation

The dissertation chapters are individual manuscripts that are either peer-reviewed publications or under review. The chapter numbers corresponding to each topic is illustrated in Figure 2.1.

3 DIFFERENCE-BASED DEEP LEARNING FRAMEWORK FOR STRESS PREDICTIONS IN HETEROGENEOUS MEDIA

Haotian Feng, Pavana Prabhakar, Difference-based deep learning framework for stress predictions in heterogeneous media, Composite Structures, Volume 269, 2021.

Abstract

Stress analysis of heterogeneous media, like composite materials, using Finite Element Method (FEM) has become commonplace in design and analysis. However, determining stress distributions in heterogeneous media using FEM can be computationally expensive in situations like optimization and multi-scaling. To address this, we utilize Deep Learning for developing a set of novel Difference-based Neural Network (DiNN) frameworks based on engineering and statistics knowledge to determine stress distribution in heterogeneous media, for the first time, with special focus on discontinuous domains that manifest high stress concentrations. The novelty of our approach is that instead of directly using several FEM model geometries and stresses as inputs for training a Neural Network, as typically done previously, we focus on highlighting the differences in stress distribution between different input samples for improving the accuracy of prediction in heterogeneous media. We evaluate the performance of DiNN frameworks by considering different types of geometric models that are commonly used in the analysis of composite materials, including volume fraction and spatial randomness. Results show that the DiNN structures significantly enhance the accuracy of stress prediction compared to existing structures, especially for composite models with random volume fraction when localized high stress concentrations are present.

3.1 Introduction

Stress analysis is an important discipline within engineering, where the primary objective is to determine stresses and strains in structures and materials subjected to external loads.

Within stress analysis, we typically start with a geometrical description of a structure or material and the expected load acting on it. Typical output of stress analysis is the quantitative distribution of stresses, strains and deformations. There are several approaches for stress analysis of solids, like classical mathematical closed form solutions for partial differential equations, computational simulation, experimental testing or a combination of these methods. Among these, Finite Element Method (FEM)[58, 149] is a commonly used computational tool for stress analysis and for designing structures and materials. By reformulating governing partial differential equations (PDE) from strong form to weak form, and implementing these in discrete form within FEM, the response of solids subjected to external loads and boundary conditions can be determined.

FEM is used extensively for analyzing composite materials[8], which are heterogeneous and usually made of individual constituent materials with unique properties that are combined together to result in improved physical properties as compared to the individual materials. Composite materials typically consist of matrix and reinforcing constituent materials, where the reinforcing material is stiff and strong, and matrix is made

of homogeneous and monolithic material that binds the reinforcements together. Typically, several length scales exist within composites, with reinforcements at the micrometer scale and composites at the meter scale. Detailed FEM analyses at multiple length scales are widely used to analyze and design these composites[28, 56, 8]. Although commonly used for stress analysis, FEM can be expensive when used for optimization and multi-scale analysis of structures and materials, especially within composite materials. Hence, the past few years have witnessed a few attempts for substituting traditional FEM with Neural Network (NN), a method within Machine Learning (ML) framework, for structural optimization[138, 137] and multi-scale analysis[95, 136].

Past researchers have shown great potential for ML and Deep Learning (DL) methods as surrogates for predicting mechanical properties in Computational Solid Mechanics and Computational Fluid Dynamics, without performing Finite Element Analysis (FEA). Earlier attempts to integrate ML techniques into FEA focus on updating model[93][1], defining material constitutive relationship[76] and approximating nonlinear constitutive behavior[61]. With limitations of ML techniques in modelling complex nonlinear models, researchers have resorted to DL method as a surrogate to FEA in the field of stress prediction. Liang et al.[80] introduced image-to-image DL model to substitute FEA for stress distribution estimation in human tissues and proved the feasibility of estimating the linkages between shape features and FEA-predicted results. Guo et al.[44]

proposed Encoder-Decoder[20] structure in CFD to predict non-uniform steady laminar flow in vehicle aerodynamic analysis and showed that it is considerably faster than traditional LBM solvers. Khadilkar et al.[5] proposed two-stream deep learning framework for stress field prediction in 3D printing, by combining extracted 2D features with 3D point clouds using CNN and PointNet[135]. Yang et al.[103] proposed an artificial neural network (ANN) to approximate yield function under given boundary conditions. Bhatnagar et al.[3] improved Encoder-Decoder structure's capability for predicting velocity and pressure field in unseen flow conditions and geometries. More in line with our work, Nie et al.[102] introduced Stress-Net by implementing Residual Network (ResNet)[52] into Encoder-Decoder structure and validated their framework using 2D linear elastic cantilevered structural analysis. This significantly improved the accuracy of von Mises stress field prediction in their models.

Inspired by the ability of CNN to extract high-level features[9] and several previous successful Encoder-Decoder models[133], we introduce a new Difference-based Neural Network (DiNN) structure in this paper that focuses on geometric and associated stress differences between different samples for stress prediction in composite (heterogeneous) materials. Instead of directly using several Finite Element model geometries and stresses as inputs, DiNN focuses on highlighting the differences in stress distribution between different input samples by using the geometry and stress differences between training samples and a reference model (de-

termined based on training samples) as input data for training the NN. Highlighting these differences in the input sample data is expected to improve the prediction accuracy. This is the first attempt, to our best knowledge, towards predicting stress distributions in heterogeneous media like composite materials that possess severe stress concentrations.

3.2 Overview of the Proposed Machine Learning Framework

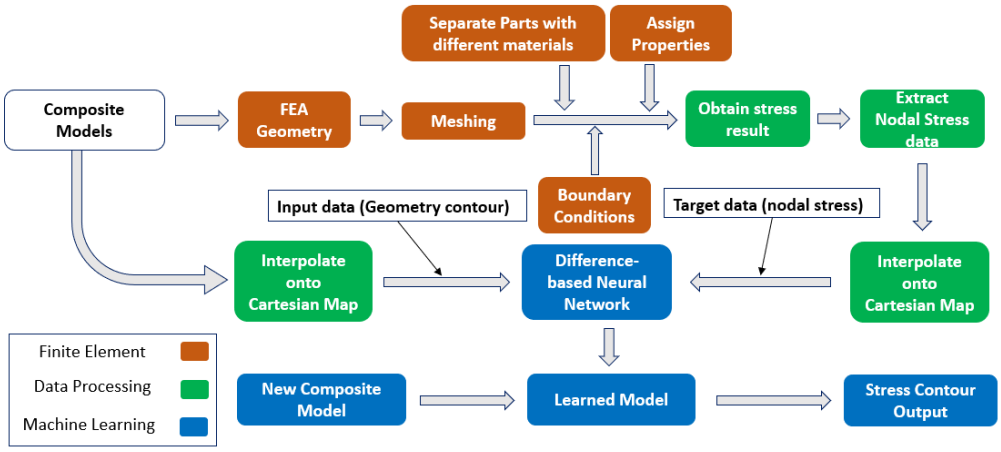

Figure 3.1: An overview of the proposed ML framework: Composite models are first generated and solved using Finite Element solver to obtain stress distribution contours. The meshed geometry and stress contours are interpolated onto Cartesian Maps and further used for training the DiNN structure. Finally, the trained DiNN is used for predicting stress distribution contours for new composite models.

In Figure 3.1, we present an overview of the proposed machine learning framework for composite structures and materials. Throughout the paper, we have used Intel Core™ i7-9700 Processor for performing FEA and post-processing. We perform the machine learning step on NVIDIA GeForce RTX 2080 SUPER with 3072 CUDA cores. First, several target composite geometries are randomly generated and meshed, and are solved numerically under quasi-static loading and linear elasticity using Finite Element software ABAQUS[134] to obtain the spatial stress distribution for each geometry.

Next, the meshed geometries and their nodal stress distribution contours are interpolated onto a uniform global map called Cartesian Map (CM)[3]. This enforces the interpolated geometry and the stress models to be of the same size in order to facilitate NN training and parameter learning through the training steps. Upon training the NN structure, the learned model is used for predicting spatial stress distribution contours and evaluating its performance.

3.3 Model Definition

Introduction to Different Geometric Models Considered

We consider composite micromechanical models in two categories: volume fraction randomness (VR) and spatial randomness (SR). To account for these variables, we analyze eight different structures shown in Fig-

ure 3.2 as the geometric models in this study: 1) plate with a circular cutout model(PC-VR), 2) square packed fiber reinforced model(SP-VR), 3) hexagonal packed fiber reinforced model(HP-VR), 4) hollow particle reinforced model(HPR-VR), 5) plate with controlled random circular cutout model(PC-SR-C), 6) plate with uncontrolled random circular cutout model(PC-SR-UC), 7) square with controlled random packed fiber reinforced model(SP-SR-C), 8) square with uncontrolled random packed fiber reinforced model(SP-SR-UC). VR models have fixed cutout or fiber centers and random radius, while SR models have random cutout or fiber centers but fixed radius. Overall external dimensions of each model is 10 x10 μm.

Importance and Relevance of Each Model Considered

We consider two dimensional plane stress analysis in this paper and focus on predicting von Mises stresses as both matrix and reinforcement regions have in-plane isotropic properties. In VR models, we vary the geometries by choosing different fiber or cutout radius r, which is calculated based on different volume fractions V_f using the equation $r = \sqrt{\frac{A_{square} * V_f}{\pi}}$. V_f describes the volume percentage of one part to the whole model. We randomly generate different values of V_f within a target range, where A_{square} is the area of the bounding square region. In SR models, we choose four cutouts or fibers in each model for investigation and validation purposes. Controlled randomness implies that each circle is randomly

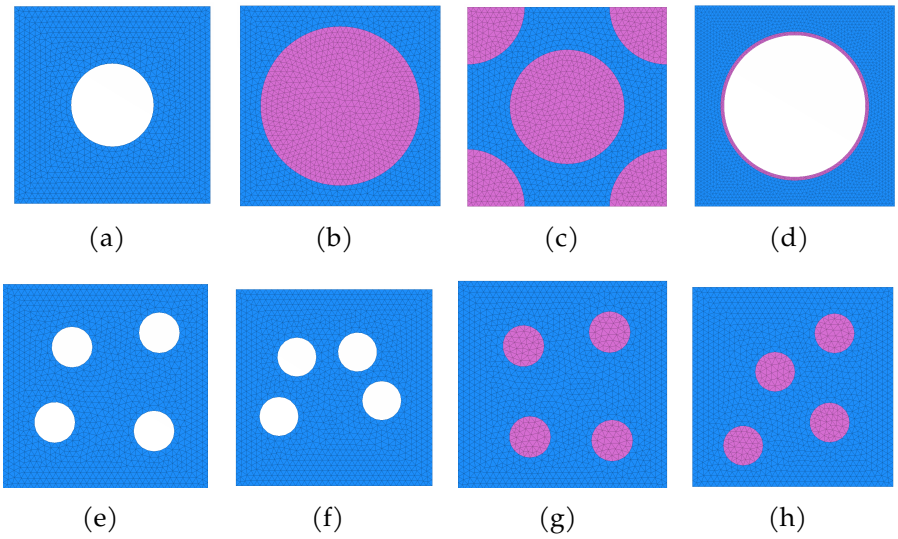

Figure 3.2: Meshed composite geometry with volume fraction randomness (top row) and meshed composite geometry with spacial randomness (bottom row): (a) PC-VR (b) SP-VR (c) HP-VR (d) HPR-VR (e) PC-SR-C (f) PC-SR-UC (g) SP-SR-C (h) SP-SR-UC. Blue and pink regions in the geometry models are different materials and the white regions are hollow.

assigned within each quarter with minimum spacing between circles to be held at 1/2 of circle radius, while uncontrolled randomness implies that only the minimum spacing constraint of 1/2 of circle radius exists.

Plate with circular cutout models

Plate with cutout designs are widely used in mechanical industries, for example airplane cabin window and screw-bolt designs. Under externally applied loads, plate with a cutout experiences high stress concentrations in the vicinity of the cutout. These high stress regions are candidate for localized damage and failure under external loads, and largely affect the

mechanical performance of structures.

A range between 5% to 25% for volume fraction is considered for circular cutout models due to relatively small cutout size. Sample meshed models are shown in Figure 3.2(a).

In addition to volume fraction, the spatial arrangement of cutout regions in the micromechanical models has a significant factor on the mechanical properties. To investigate Neural Network's performance on models with different spatial arrangements, we consider four random cutouts with controlled and uncontrolled randomness, as shown in Figure 3.2(e,f).

Fiber reinforced polymer composite micromechanical models

Fiber reinforced polymer composite (FRPC) materials are widely used in aerospace, automotive, marine and construction industries due to its higher strength comparing to pure polymer matrix. FRPCs typically consist of two parts: stiff reinforcing fibers and a less stiff binding matrix. In this paper, we choose FRPCs as a model system. One key design feature in FRPCs is the fiber volume fraction V_f, which contributes directly to their mechanical properties. Fibers within FRPCs typically have diameters in the range of few micro meters, for example, carbon fibers are approximately 6 μm in diameter. Since a structure made of composite is in the order of few meters, representing each fiber in a computational domain is not practical. Often, we resolve to micromechanics for analyzing such composites.

In micromechanical analysis of composites, a large composite domain can be represented by arrays of small repeating unit cells (RUC). Here, we consider two RUCs: square packed and hexagonal packed models of fibers embedded in matrix with fibers having their actual diameter and the entire fiber-matrix domain has a fiber volume fraction equal to that of the macro scale composite domain. Thus, the micromechanics models are in the order of micrometers while effectively capturing the mechanical behavior of large composites. Square-packed RUC of FRPCs has fiber in the center and a square-shaped matrix surrounding it as shown in Figure 3.2(b), while hexagonal packed RUC has a full fiber in the center and four quarter fibers in each corner of the square matrix domain as shown in Figure 3.2(c). For validation purposes, we simply assume hexagonal packed composite to be a square shaped domain as in the case of a square fiber packed model. Fiber volume fraction of 40% to 60% are most common in real FRPC materials. Hence for this paper, we consider the same volume fraction range to generate RUC models with random fiber diameters.
Similar to plate with random cutout model, to account for the effects of spatial arrangement, we further consider square packed composites with randomly distributed fibers as shown in Figure 3.2(g,h).

Hollow Particle Reinforced Composite

Hollow particle reinforced composites, also referred to as syntactic foams, are gaining traction in lightweight applications due to their low den-

sity, high compressive energy absorption capability and large strains to failure[13, 122, 40, 64]. Syntactic foams typically consist of stiff hollow particles (often at the micro-scale) randomly dispersed in a softer matrix region, which results in lightweight closed cell foams. A unit cell representation of hollow particle reinforced composite consists of a square block with circular cutout and a thin reinforced ring layer at inner surface of the cutout that represents the cut section of a reinforcing particle. The reinforced layer is typically made of stiffer materials, like glass or ceramics, as shown in Figure 3.2(d).

We choose the wall thickness of the reinforcing ring to be approximately 1/22.5 of the inner diameter (hole diameter) based on prior experimental research performed by Jayavardhan et al.[64]. In this paper, we consider the volume fraction of the cutout region to be in the range from 40% to 60% with a ring thickness of 0.18 μm.

Finite Element Analyses for Training Data Generation

All the domains mentioned above are 2D plane stress models with the same external dimensions. Linear elastic mechanical properties of polymer matrix ($E = 3.2$ GPa, $\upsilon = 0.31$)[71] are assigned, which are typical of epoxy resin used in fiber reinforced polymer matrix composites. For reinforced composites, linear elastic carbon fiber properties ($E = 8.0$ GPa, $\upsilon = 0.35$)[110, 111, 112, 130] in the plane perpendicular to the fiber direction are assigned. The external boundaries of each domain are defined as Γ_1,

Γ_2, Γ_3 and Γ_4, respectively, for the top, left, bottom and right edges. The boundary conditions on each boundary is described below in terms of horizontal (u) and vertical (v) displacements as Equation 3.1. Essentially, each model is subjected to a positive displacement along the vertical direction subjecting them to compression.

$$\begin{aligned} v &= -0.1\,\mu\text{m} \quad \text{on} \quad \Gamma_1 \\ u &= 0 \quad \text{on} \quad \Gamma_2 \\ v &= 0 \quad \text{on} \quad \Gamma_3 \\ u &= \text{constant} \quad \text{on} \quad \Gamma_4 \end{aligned} \tag{3.1}$$

Using the above mentioned inputs to each domain, we perform mesh convergence analysis to determine the maximum (max) mesh size that provides converged stress predictions. From this analysis, we identify that the hollow particle reinforced composite model requires a max mesh size of $0.2\,\mu$m and the other three models require a max mesh size of $0.3\,\mu$m. By assigning material properties along with above-mentioned boundary conditions, we generate stress distribution contours using FEM static solver.

3.4 Difference-based Neural Network Framework

An Encoder-Decoder Neural Network[20] is typically trained using geometry and stress contours directly as inputs. Past researchers have demon-

strated that embedding residual learning into Encoder-Decoder structure can significantly improve the accuracy of prediction. Nie et al.[102] proposed Stress-Net structure based on residual learning algorithm, which was shown to improve the accuracy of stress distribution prediction. However, the existing Stress-Net structure does not provide high prediction accuracy when localized high stresses exist, like stress concentration, especially within composite materials. In this paper, a novel NN structure is developed that embeds engineering and statistical knowledge for stress prediction. During engineering design iterations, engineers typically use an initial design as the reference model and then refine the subsequent designs. Similar to this idea, a known geometry model and corresponding stress distribution contour are chosen as the reference model when training the target NN. Then, the differences between different geometry contours are used to guide NN to focus on training stress difference contours σ. We refer to this as a Difference-based Neural Network (DiNN) structure shown in Figure 3.3. The DiNN structure consists of three modules: sample processing, Encoder-Decoder and stress prediction. Difference-based Neural Network with normalization (DiNN-N) is built upon DiNN by adding additional normalization and de-normalization blocks (orange color). Further, Difference-based Neural Network with normalization and clean module (DiNN-NC) is developed based on DiNN-N structure by adding two additional clean modules (blue color).

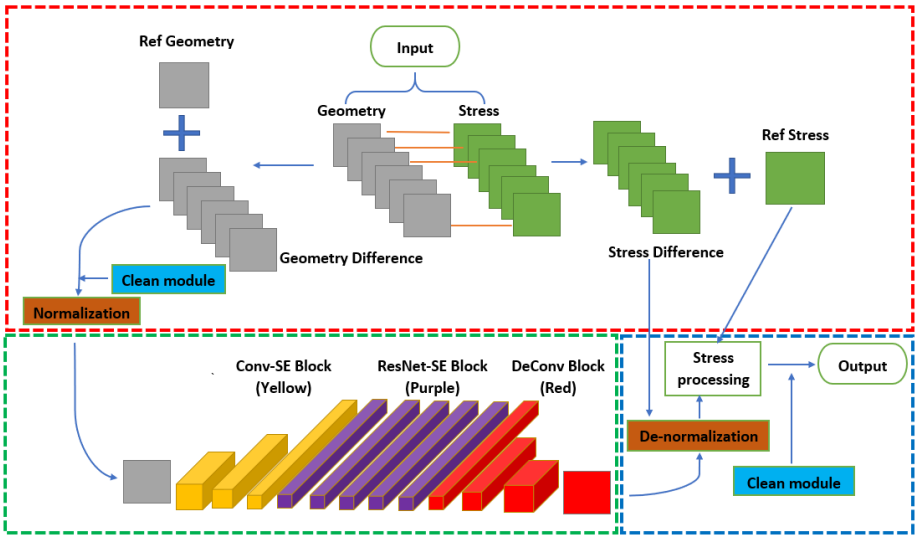

Figure 3.3: Difference-based Neural Network Framework: sample processing module (red dash line), Encoder-Decoder module (green dash line), stress prediction module (blue dash line). Two orange blocks are added for DiNN-N structure and two blue blocks are added in addition for DiNN-NC structure.

Sample processing module

Sample processing module mainly extracts geometry and stress contour information from the training data. Mean geometry and stress contours across training models are extracted as reference sample (labelled as Ref Geometry and Ref Stress). Geometry difference contours, stress difference contours and mean stress contours are used further for training the NN. To avoid covariate shifting and improve training efficiency, a pair of normalization and denormalization modules are added. Denormalization module is defined in section 3.4. Normalization block is developed based on Min-Max feature scaling function[72] described in Equation 7.2, where

G refers to the labelled geometry difference contour.

$$\text{Normalization} : \text{output} = \frac{\text{input} - \min(G)}{\max(G) - \min(G)} \tag{3.2}$$

Encoder-Decoder module

Encoder-Decoder module consists of three types of blocks: Conv-SE (yellow), ResNet-SE (purple) and DeConv (red) blocks: (1) Each Conv-SE block, as shown in Figure 3.4(a), consists of one 2D convolutional layer with ReLU and Batch-normalization, and one Squeeze-and-Excitation (SE) block[57]. The convolutional layer extracts high level key features of geometry difference contours and SE block adaptively re-calibrates channel-wise feature responses by modelling inter-dependencies between different channels. (2) ResNet-SE block is constructed based on ResNet architecture and consists of two convolutional blocks and one SE block to enhance the extracted inter-dependent high level features, as shown in Figure 3.4(b). (3) DeConv blocks follow ResNet-SE blocks, and each consist of one 2D deconvolutional layer[151] with Batch-normalization, as shown in Figure 3.4(c). The DeConv blocks expand key features and finally back to the original input dimensions. Since the differences between the original and mean contours generally have a zero mean and certain variations, we assume that it follows a Gaussian distribution, and hence use Glorot initialization for weight initialization[150].

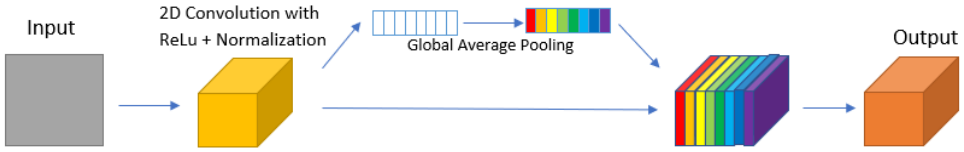

(a)

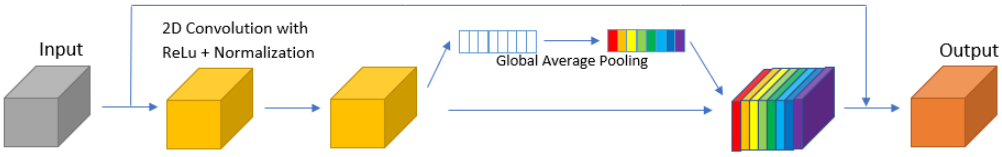

(b)

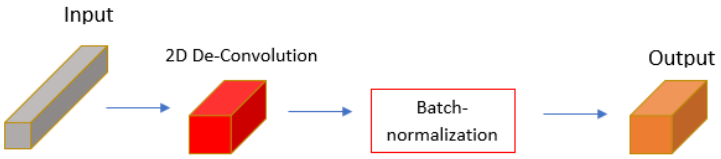

(c)

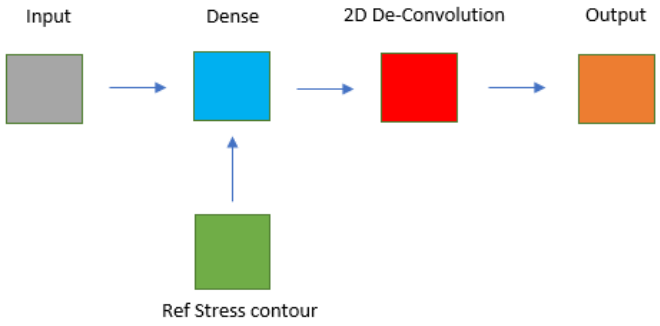

(d)

Figure 3.4: Inner structures of (a) Conv-SE block; (b) ResNet-SE block; (c) Deconv block; (d) Stress processing block

Stress prediction module

Stress prediction module shown in Figure 3.3 follows the Encoder-Decoder module. The De-normalization block reverts the effect of normalization, as defined in Equation 3.3. Here, σ represents the stress difference contour. A stress processing block is added after the De-normalization block, which generates the predicted stress contours as shown in Figure 3.4(d). It consists of one dense block for combining the predicted stress differences (input) and the reference stress contour, followed by 2D De-Convolution block to smooth the prediction. The kernel size of the De-convolution layer is selected based on the uniformity in stress distributions. A kernel size of [2,2] is used for the De-Convolution block if large stress concentrations occur (DiNN-NC) and a kernel size of [1,1] is used otherwise (DiNN-N). Using [2,2] kernel size is beneficial in models with large stress concentrations as the differences between pixel values are higher. Here, we consider that large stress concentration exists if the stress ratio defined as $R_\sigma = \sigma_{max}/\sigma_{mean}$ is larger than 2.

$$\text{Denormalization} : \text{output} = \text{input} * (\max(\sigma) - \min(\sigma)) + \min(\sigma) \quad (3.3)$$

Clean module (Only for geometry with cutout region)

For geometric models that have regions of no material, like in the case of plate with circular cutout model and hollow particle reinforced model, varying the size or position of the cutout regions can introduce undesired

negative values during subtraction with the reference contours (refer to section 3.5). Hence, we introduce an additional module called "clean module". This module performs element-wise multiplication between the target contour and material contour M, whose regions with material are labelled as '1' and regions without material (cutout) as '0'. The multiplication can be represented with Hadamard product[131] shown in Equation 3.4, manually forcing regions without material to be zero valued. Here, A_{ij} represents the input contour and C_{ij} represents the output contour after passing through the clean module.

$$C_{ij} = (A \circ M)_{ij} = A_{ij} M_{ij} \tag{3.4}$$

$$M_{ij} = \begin{cases} 1, & \text{if material exists at a node} \\ 0, & \text{if material is absent at a node} \end{cases}$$

DiNN-N versus DiNN-NC

The key difference between DiNN-N and DiNN-NC is the addition of a clean module within DiNN-NC. Specifically, DiNN-N structure can be viewed as a special case of DiNN-NC, where the material contour M in Equation 3.4 is a matrix with all-ones as no cutout region exists. Besides, to account for the presence of a clean module, we choose difference kernel sizes, as discussed in section 3.4.

3.5 Interpolation on Cartesian Map

Data Pre-processing: Barycentric Coordinate Interpolation

Meshed geometries and corresponding stress contours are used for training and evaluating different NN frameworks. Each training sample has a unique shape due to geometry randomness considered, resulting in different meshes in the domain. This poses difficulty for NN training. To render the geometry as well as stress contour trainable for NN, these contours are further interpolated onto a global Cartesian Map (CM), such that all contours have the same size. CM has the same dimensions as that of the geometric models, which are 10 μm-by-10 μm.

Triangulation-based linear interpolation[4] is widely used for map-to-map interpolation due to its simplicity and efficiency. With known position of each node in the CM, this algorithm searches for three nearest nodes in the original FEM mesh to form a triangle. This could introduce large artificial errors due to matrix illness in FEM meshed models when complex boundaries or stress concentrations are present that may require non-uniform mesh with smaller mesh size. To avoid this in the DiNN framework, we use Barycentric Coordinate (BC) system[55], also known as area coordinates, which normalizes each axis and generates homogeneous coordinates. Due to this characteristic, BCs are extremely useful in rendering the interpolation more stable within triangular sub-domains. BC can accurately determine nodal location with respect to triangular

mesh, as well as interpolation coefficient with three vertices. Each node in the CM is projected onto FEA mesh model to find the triangle it falls within. Then, the target value of each node on the CM is calculated using corresponding values of three vertices of the triangle. Relative positions between a node and a triangle are determined by three Barycentric parameters $\lambda_1, \lambda_2, \lambda_3$, which are determined using Equation 3.5. Here, $\{x_i, y_i\}$ represents the coordinate of each vertex of the triangle and $\{x, y\}$ represents the coordinate of a target node on the CM.

$$\lambda_1 = \frac{(y_2 - y_3)(x - x_3) + (x_3 - x_2)(y - y_3)}{(y_2 - y_3)(x_1 - x_3) + (x_3 - x_2)(y_1 - y_3)} \tag{3.5a}$$

$$\lambda_2 = \frac{(y_3 - y_1)(x - x_3) + (x_1 - x_3)(y - y_3)}{(y_2 - y_3)(x_1 - x_3) + (x_3 - x_2)(y_1 - y_3)} \tag{3.5b}$$

$$\lambda_3 = 1 - \lambda_1 - \lambda_2 \tag{3.5c}$$

Interpolated nodal values on the CM can be determined by Equation 3.6:

$$S = \lambda_1 S_1 + \lambda_2 S_2 + \lambda_3 S_3 \tag{3.6}$$

where, S is the nodal value on the CM containing geometry label or physical information like stress. S_i is the i^{th} nodal value of the triangular element within which the node on the CM falls.

Next, we perform a comparison between von-Mises stress contours obtained using linear interpolation (with nearest three nodes and nearest five nodes) and Barycentric coordinate interpolation on a square packed model. It is observed that the nearest three nodes linear interpolation

generates negative values, while nearest five nodes linear interpolation also manifests several noisy points with minimum stress approximately equal to zero. On the other hand, BC interpolation does not cause illness and singularity, and successfully represents the stress distribution contour and stress ranges after interpolation.

In addition to the interpolation method, CM density is a key factor that contributes towards interpolation values. To ensure that the CM captures important statistical features of the geometry and stress distribution contours, we perform stress interpolation analysis to establish the CM density that gives reasonable interpolation accuracy and efficiency. From this analysis, we observe that the interpolation accuracy increases with increasing CM density, while the interpolation speed decreases. To strike a balance between accuracy and efficiency, especially accounting for large sample sizes, we select a CM density of 79-by-79, which has the shape of 80-by-80 after converting to nodal matrix. Such CM density can provide an interpolation accuracy above 99% in max stress and a reasonable interpolation speed of 26 samples/minute. Examples of geometry and stress contour interpolation onto CM for PC-VR and SP-VR models are shown in Figure 3.5.

Statistical Property Analysis

As compared to the existing Stress-Net structure, the objective of our proposed DiNN structure is to improve the accuracy of prediction based

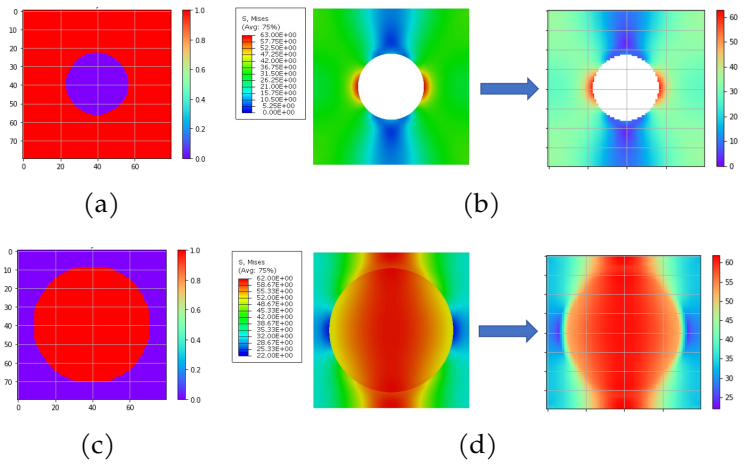

Figure 3.5: Geometry contour labelling and Stress interpolation from FEA output to Cartesian Map for PC-VR (a and b) and SP-VR model (c and d).

on a reference data set and render the training process more statistically stable. To that end, we calculate the mean and skewness in the training samples by considering a subset of the data points in the regions where the geometry of the models change, that is in the vicinity of cutout or fiber. We consider nine points (A-I) in this region and calculate skewness values based on Pearson's second skewness coefficient shown in Equation 3.7 [74].

$$\text{skewness} = \frac{3(\text{mean} - \text{median})}{\text{standard deviation}} \tag{3.7}$$

Skewness in training data can cause imbalance problem and eventually reduce the prediction accuracy of NN by introducing unbalanced data [62, 91]. There are typically two ways of reducing skewness: 1) model-oriented (reduce skewness in the structure) and data-oriented (reduce skewness by

pre-processing)[132]. To reduce the skewness in data, element-wise root operation on the training samples is performed for positive skewed data and element-wise power is used to deal with negative skewed data[30]. In this section, we use three models for illustration: PC-VR, SP-VR and PC-SR.

Since geometry labels are constant for individual regions of heterogeneous media, nodal stress values are the main source of skewness. DiNN structures make the training data more zero centered and symmetric. For models with cutout, DiNN-NC reduces the max-min range that can increase due to the presence of cutout region. DiNN-NC is more effective for models with significant stress concentration near the cutout edges. For SP-VR, since DiNN only performs mean contour subtraction (a linear operation), the data has a zero mean value and skewness value will not change. For PC-VR and PC-SR-UC models, by adding clean module within DiNN, DiNN-NC alters the statistical properties for cutout regions, resulting in few nodes with non-zero mean values. On the other hand, clean module switches all skewness values to positive as compared to the original sample. This helps in improving the accuracy of DiNN prediction, and facilitate further steps to reduce the effect of skewness if needed.

3.6 Machine Learning Model Inputs

As discussed in the previous section, both nodal stress contours and geometry contours for different models are interpolated onto CM for training the NN. Unique labels are assigned to each region, including cutout region, fiber region, particle ring region and matrix region. In this paper, same boundary conditions and loads are maintained in all analyses, and hence, the effects of boundary condition labelling are not discussed.

To train the NN and test its performance, we randomly generate a total of 2000 samples for each model based on different cutout or fiber volume fractions. When training for each model, the total samples are randomly split into 80% for training with 10% for cross-validation and 10% for testing. Random split seed is controlled based on the pseudorandom number generator[92] developed in scikit-learn[107] for comparison purposes.

Geometry labelling method

To identify different regions in each model and facilitate machine learning process, we need to assign different labels to each region. Overall labelling method is summarized in Equation 3.8, where G_{ij} represents the label for a target geometry,

$$G_{ij} = \begin{cases} 0, & \text{if any material is absent at CM node} \\ 1, & \text{if matrix material exists at CM node} \\ 2, & \text{if reinforcement material exists at CM node} \end{cases} \tag{3.8}$$

Analyzing the Effect of Skewness

We previously discussed the effect of skewness in training data on the prediction accuracy of NN in section 3.5. We noticed that all the skewness values become positive after adding the clean module to DiNN. To determine the optimal solution for reducing the effect to positive skewness and enhancing the prediction accuracy, we introduce a skewness correction factor p. By considering different root 'p' over the stress contour values prior to training the NN, our goal is to reduce the influence of skewness on the accuracy of prediction. Element-wise root values are calculated before extracting the mean stress contour and correspondingly element-wise power is introduced after obtaining the prediction from the Deconv block. The predicted stress contour can be expressed using Equation 3.9a, where the original input geometry contour to the NN is G, $NN(w, b)$ is the NN with parameters w and b. $\sigma_{average}$ is the average stress contour used as the reference contour during training, which is calculated using Equation 3.9b. Different values of p are considered for investigating the hidden relationships within DiNN using HP-VR model.

$$\sigma_{output,ij} = [(G * NN(w, b))_{ij} + \sigma_{average,ij}]^p \qquad (0 < p \leqslant 1) \tag{3.9a}$$

$$\sigma_{average,ij} = \frac{1}{N} \sum_{n=1}^{N} \sqrt[p]{\sigma_{n,ij}} \tag{3.9b}$$

3.7 Results and Discussion

We construct NN frameworks within Tensorflow 2.0.0 and train it on GPU as discussed in section 4.2. To test the prediction capability of different NN frameworks for eight different geometric models considered, we use the Stress-Net structure for comparison. The accuracy of stress prediction within each component of composite materials, NN training duration and training loss are used for evaluating each model.

Prediction error definition

We evaluate the prediction accuracy of max stress based on the max stress error rate (MER) as defined in Equation 3.10a and evaluate the training loss based on the mean squared error (MSE) in stress prediction as defined in Equation 3.10b. Here, N is the total number of samples in the testing set and n is the total number of nodes in the CM. Y_i is the nodal stress predicted using the NN and $\hat{Y}_i$ is the ground truth nodal stress mapped onto the CM from FEA. $Y_{i,j}$ and $\hat{Y}_{i,j}$ represent the j^{th} nodal stress values in

i^{th} sample obtained from the NN and FEA, respectively. MER estimates the maximum stress prediction error within a model, which is relevant for evaluating composite model's fracture or plasticity initiation. MSE evaluates the accuracy of the stress distribution contour prediction in the entire model, which is important for estimating effective properties, such as the effective stiffness. Training accuracy and efficiency of different NN structures on eight geometric models considered in this paper are summarized in Section 3.7.

$$MER = \frac{1}{N}\sum_{i=1}^{N}\frac{|\max(\hat{Y}_i) - \max(Y_i)|}{\max(\hat{Y}_i)} \times 100\% \tag{3.10a}$$

$$MSE = \frac{1}{N}\sum_{i=1}^{N}(\frac{1}{n}\sum_{j=1}^{n}(Y_{i,j} - \hat{Y}_{i,j})^2) \tag{3.10b}$$

Neural Network prediction results

We evaluate different NN frameworks, including a baseline model (Stress-Net) and three types of difference-based structures developed by us: DiNN, DiNN-N and DiNN-NC, on all geometric models considered in this paper. DiNN-NC structure was used only when cutout region exists in the target geometry.

We train each NN framework with a total of 1000 and 2000 samples separately, and use stochastic gradient descent (SGD)[11] as the optimizer with learning rate set as 0.001. We choose the training epoch number and steps when prediction accuracy has converged. Figures 3.6 to 3.9 show

examples of predicted stress contours compared to that generated by FEA for each geometric model as well as the errors (MER and MSE) and training duration while considering 1000 total number of samples. Prediction results for 1000 total samples are used for illustration purposes. Based on the training results obtained from these eight geometric models, we conclude the following:

1. Prediction accuracy for models without cutout regions:

- Table 3.1 shows the prediction performance comparing DiNN-N and baseline model Stress-Net for 1000 samples. We observe that DiNN-N increases the prediction accuracy in both MER and MSE for SP-VR and HP-VR models. Figures 3.6 and 3.7 show the predicted stress contours and the difference between NN prediction and FEA. In Figures 3.6(b) and 3.7(b), we observe large stress differences in Stress-Net prediction (in dark red and blue) while this difference is reduced when DiNN-N is used for both models.

Table 3.1: Prediction error rate of 1000 samples for models without cutout regions

Prediction Error comparing to Baseline	SP-VR composite	HP-VR composite
	DiNN-N	DiNN-N
Fiber MER reduction	38%	41%
Matrix MER reduction	20%	43%
Contour MSE reduction	21%	15%

- In general, DiNN-N significantly reduces the max stress error rate in both fiber and matrix, as well as lowers the MSE value compared

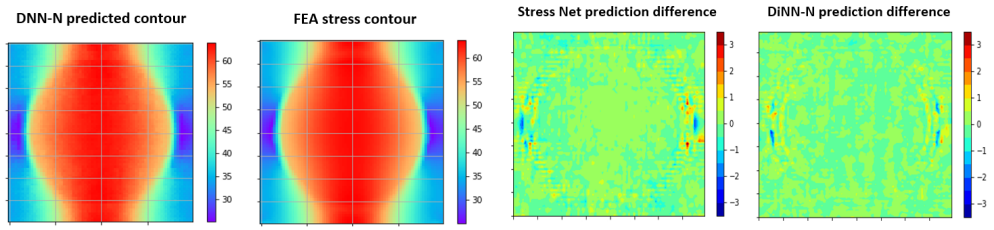

Figure 3.6: SP-VR model: (a) Comparison of DiNN-N prediction and FEA stress output (b) Comparison of difference in predicted stress distribution of Stress-Net and DiNN compared to FEA stress output

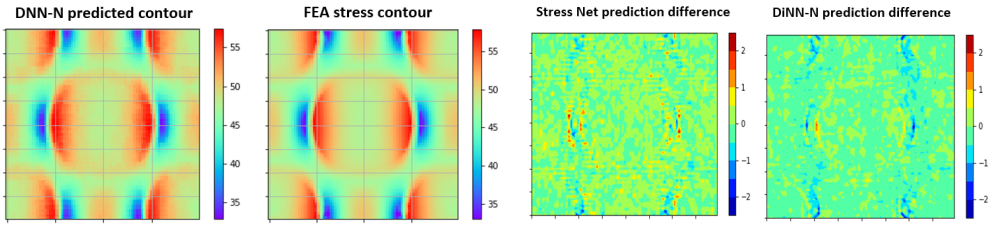

Figure 3.7: HP-VR model: (a) Comparison of DiNN-N predicted and FEA stress output contours (b) Comparison of difference in predicted stress distribution of Stress-Net and DiNN compared to FEA stress output

to the baseline model. Hence, our proposed DiNN-N structure is shown to be a better structure for stress prediction in composite models without cutout region.

2. Prediction accuracy for models with cutout regions:

- Table 3.2 shows the prediction performance comparing DiNN-N, DiNN-NC and baseline model Stress-Net for 1000 samples. DiNN-NC is proposed for models with cutout and severe stress concentration. Here, we show that DiNN-NC improves the performance in

such cases. That is, for PC-VR composite model, DiNN-N reduces MER, however, MSE value increases compared to the baseline model. This is attributed to extra noise from cutout region during mean contour subtraction. By adding the clean module, DiNN-NC manifests the lowest MER and MSE values with significant reduction compared to the baseline model. For HPR-VR composite model, prediction accuracy of DiNN-N for maximum stress in the ring region is worse compared to baseline model due to severe stress concentration ($R_\sigma > 4$) around cutout and within the ring (particle) region. The negative influence of noise in the cutout region is more significant as compared to the PC-VR model. Hence, by introducing the clean module, DiNN-NC shows higher prediction accuracy. Figure 3.8(b) and Figure 3.9(b) similarly show that DiNN-NC significantly reduces large prediction differences in stress distribution as highlighted by dark red and blue colors compared to baseline and DiNN-N models.

Table 3.2: Prediction error rate of 1000 samples for models with cutout regions (red color means worse prediction comparing to baseline)

Prediction Error comparing to Baseline	PC-VR composite		HP-VR composite	
	DiNN-N	DiNN-NC	DiNN-N	DiNN-NC
Ring MER reduction	—	—	-1%	39%
Matrix MER reduction	46%	76%	6%	75%
Contour MSE reduction	-105%	86%	-142%	89%

- In general, we have shown that DiNN-NC structure has the best performance in terms of accurate stress prediction compared to Stress-Net (baseline) and DiNN-N for heterogeneous media with dis-

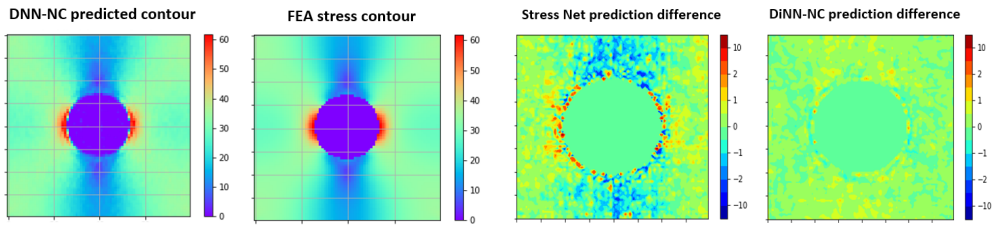

(a) (b)

Figure 3.8: PC-VR model: (a) Comparison of DiNN-NC predicted and FEA stress output contours (b) Comparison of difference in predicted stress distribution of Stress-Net and DiNN compared to FEA stress output

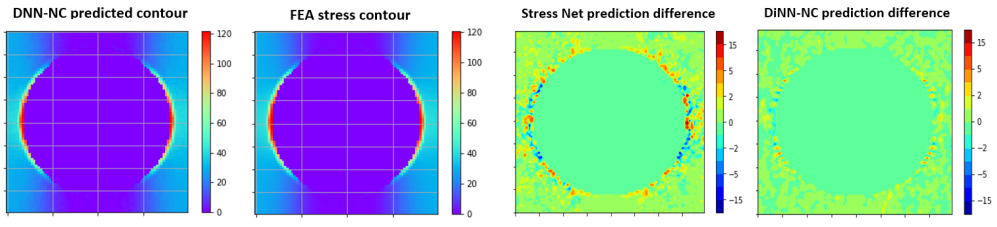

(a) (b)

Figure 3.9: HPR-VR composite: (a) Comparison of DiNN-NC predicted and FEA stress output contours (b) Comparison of difference in predicted stress distribution of Stress-Net and DiNN-NC compared to FEA stress output

continuities, especially when significant stress concentrations exist ($R_\sigma > 2$).

3. Prediction accuracy for models with spatial randomness:

- Table 3.3 shows the prediction performance comparing DiNN-N, DiNN-NC and Stress-Net baseline model for test models with spatial randomness. Within this category, the performance of DiNN frameworks (DiNN-N, DiNN-NC) compared to baseline model is

mixed. For SP-SR models (SP-SR-C and SP-SR-UC), DiNN-N performs better compared to baseline model except in the case of fiber MER. That is, the fiber MER is relatively larger for uncontrolled randomn SP-SR model. As for PC-SR models (PC-SR-C and PC-SR-UC), the prediction performance of DiNN-NC is worse in terms of MER, but better in terms of MSE, for both controlled spatial randomness and uncontrolled spatial randomness. This is attributed to the concept of reference contour representing an initial guess of stress distribution contour within our approach that gives a general guideline to stress distribution contour. In that case, if our model has large spatial randomness, the reference contour cannot fully represent the geometric variations and highlight the key areas, thus posing additional challenge in predicting the difference stress contour and adversely affecting the MER. For square packed model, since no cutout or severe stress concentration exists, advantages of reference contour as initial guideline plays a positive role. Whereas, for PC-SR models, cutout regions and localized stress concentration are averaged over the reference contour, which makes the stress difference contour more unbalanced. Hence, this results in poor performance of DiNN-NC for plate with cutout models with spatial randomness which requires further analyses and is beyond the scope of this paper. Figure 3.10(b) and Figure 3.11(b) highlight the prediction difference (error) of baseline model Stress Net and DiNN-NC with respect to

corresponding FEA predictions shown in Figure 3.10(a) and Figure 3.11(a), respectively, corroborating that DiNN-NC has much lower prediction MSE.

Table 3.3: Prediction error rate of 1000 samples for models with spatial randomness (red color means worse prediction comparing to baseline)

Prediction Error comparing to Baseline		PC-SR composite		SP-SR composite
		DiNN-N	DiNN-NC	DiNN-N
Controlled randomness	Fiber MER reduction	—	—	47%
	Matrix MER reduction	-72%	-23%	13%
	Contour MSE reduction	-112%	60%	28%
Uncontrolled randomness	Fiber MER reduction	—	—	-10%
	Matrix MER reduction	-173%	-38%	12%
	Contour MSE reduction	-494%	45%	17%

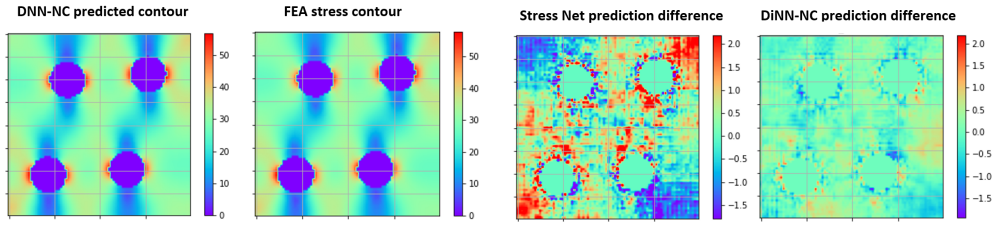

(a) (b)

Figure 3.10: PC-SR-C: (a) Comparison of DiNN-NC predicted and FEA stress output contours (b) Comparison of difference in predicted stress distribution of Stress-Net and DiNN-NC compared to FEA stress output

- To summarize, with limited data size, DiNN frameworks enhance MSE in their prediction for all models but could have larger MER in certain models and certain areas compared to baseline model. Further research is needed for investigating solutions to address this challenge in spatially random models.

4. Comparison of training and prediction duration between NN frame-

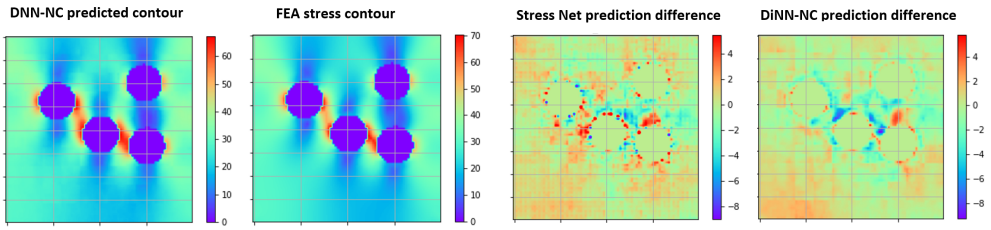

Figure 3.11: PC-SR-UC: (a) Comparison of DiNN-NC predicted and FEA stress output contours (b) Comparison of difference in predicted stress distribution of Stress-Net and DiNN-NC compared to FEA stress output

works: Baseline model Stress-Net in general has lower training duration compared to DiNN structures presented in this paper. This is because the difference-based structures are built based on Stress-Net. DiNN frameworks only have marginally longer training duration in a reasonable range. We observe that DiNN increases the training duration by ≈27% and DiNN-NC increases the training duration by ≈58%, which is around 200 seconds more for 800 samples. Among the DiNN structures presented in this paper, adding DiNN-N marginally reduces the training duration as it forces the input and output of the Encoder-Decoder module to stay within similar limits. On the other hand, adding the clean module (DiNN-NC) introduces additional computational cost. However, it should be noted here that the NN training stage is only for establishing the parameters and is a one-time event. Whereas, the prediction duration per sample for DiNN-N and DiNN-NC is on average only 0.2 seconds more

compared to Stress-Net.

5. Comparison of prediction duration between proposed NN and FEM: The goal of substituting FEM with NN is to accelerate the speed of stress prediction. Our DiNN frameworks (DiNN-N, DiNN-NC) have similar prediction speed as the baseline model, while both frameworks are in average more than 6 seconds faster for making a single prediction compared to FEM. The time saving is significant for micromechanical models and the prediction efficiency of DiNN will become more significant as model becomes increasingly complex or more design iterations are required to be tested.

3.8 Conclusions

In this paper, we have presented a novel NN framework as a surrogate for traditional FEM approach to predict stress distribution in heterogeneous media, like composite materials. Our approach consists of a set of DiNN frameworks capable of predicting stress distributions with very high accuracy for different types of composite materials. Two main types of composites are considered: models with volume fraction randomness and models with spatial randomness. Eight different composite micromechanical models were considered for validating the performance of our NN structures. For models with volume fraction randomness, the proposed DiNN structure included a normalization module (DiNN-N) for all

geometries considered, while we additionally introduced a clean module with DiNN-N, named DiNN-NC, for geometries with discontinuities.
For models with spatial randomness, DiNN frameworks perform well in terms of prediction MSE, but can have mixed performance in terms of MER. Further research effort is needed to resolve unstable MER for spatially random distributed models.
The DiNN frameworks presented in this paper for stress prediction in heterogeneous media can be used in future studies including mechanical property prediction and composite structure optimization at multiple length scales.
Key contributions of this paper are:

1. This is the first attempt to our best knowledge that brings Convolutional Neural Network based Machine Learning for stress distribution prediction for heterogeneous media like composite materials considering volume fraction and spatial randomness.
2. We introduce a novel Difference-based Neural Network framework which utilizes a set of reference models from the training set and focuses especially on training the difference contours between the target model and the reference set. This is shown to improve stress prediction accuracy when high stress concentrations manifest within heterogeneous media, with or without discontinuities like cutouts.
3. We show that the Difference-based Neural Network framework improves the stress prediction accuracy significantly compared to existing

baseline structures, especially on models with volume fraction randomness and large local stress concentrations. For models with spatial randomness, our framework guarantees a reliable prediction in terms of Mean-Squared-Error. Moreover, our proposed framework has a faster prediction speed compared to traditional Finite Element Method.

4 PARAMETERIZATION-BASED NEURAL NETWORK: PREDICTING NON-LINEAR STRESS-STRAIN RESPONSE OF COMPOSITES

Haotian Feng, Pavana Prabhakar, Parameterization-based Neural Network: Predicting Non-linear Stress-Strain Response of Composites, arXiv preprint arXiv:2212.12840 (2022).

Abstract

Composite materials like syntactic foams have complex internal microstructures that manifest high-stress concentrations due to material discontinuities occurring from hollow regions and thin walls of hollow particles or microballoons embedded in a continuous medium. Predicting the mechanical response as non-linear stress-strain curves of such heterogeneous materials from their microstructure is a challenging problem. This is true since various parameters, including the distribution and geometric properties of microballoons, dictate their response to mechanical loading. To that end, this paper presents a novel Neural Network (NN) framework called Parameterization-based Neural Network (PBNN), where we relate the composite microstructure to the non-linear response through this trained NN model. PBNN represents the stress-strain curve as a parameterized

function to reduce the prediction size and predicts the function parameters for different syntactic foam microstructures. We show that compared to several common baseline models considered in this paper, the PBNN can accurately predict non-linear stress-strain responses and the corresponding parameterized functions using smaller datasets. This is enabled by extracting high-level features from the geometry data and tuning the predicted response through an auxiliary term prediction. Although built in the context of the compressive response prediction of syntactic foam composites, our NN framework applies to predict generic non-linear responses for heterogeneous materials with internal microstructures. Hence, our novel PBNN is anticipated to inspire more parameterization-related studies in different Machine Learning methods.

4.1 Introduction

This paper presents a Neural Network (NN) framework for predicting the non-linear stress-strain behavior of heterogeneous materials like composites under mechanical loading. We relate the composite microstructure to the non-linear response through this trained NN model. In particular, we build this framework in the context of the compressive response prediction of polymeric foams called 'syntactic foams' with their microstructure as the inputs. Syntactic foams have complex internal microstructures with high-stress concentration regions and macroscale non-linear compressive

stress-strain responses, making them more challenging to understand and predict their stress-strain responses. In that direction, the NN presented in this paper applies to predicting generic non-linear responses for composites with internal microstructures.

Syntactic foams, specifically polymer ones, are closed-cell composite foams with hollow spheres or particles called 'microballoons' embedded in a polymer matrix. The presence of hollow spheres results in several excellent mechanical properties, including lower density, higher specific strength, lower thermal expansion coefficient, and lower moisture absorption[45, 41]. Due to these properties, syntactic foam materials are widely used as buoyancy materials for marine applications as a component of sea-related products and offshore products[21, 47]. Moreover, syntactic foams have been extended to other applications like the aerospace and automotive industry. For effective design and optimization, such extended applications require an in-depth understanding of their mechanical properties, especially the stress-strain responses.

Past researchers have focused on understanding the mechanical properties of syntactic foams through experimental testing and numerical studies. Gupta et al.[46] performed compression tests and showed that compressive strength and modulus would increase when the microballoon radius decreases. Shahapurkar et al.[123] experimentally showed that compressive strength decreased with increasing cenosphere volume fraction for both modified and unmodified surfaces. Moreover, the au-

thors showed a reduction in the compressive modulus but an increase in the compressive strength for arctic-conditioned samples. Jayavardhan et al.[65] conducted quasi-static compressive testing of glass microballoon reinforced high-density polyethylene syntactic foams with different densities. The authors showed that the compressive modulus increased as the microballoon volume fraction increased, but the yield strength, densification stress, and overall energy absorption were reduced. Exploring the influence of many parameters of syntactic foams experimentally is challenging and time-consuming. Thus later, Prabhakar et al.[109] developed the computational modeling to establish a fundamental understanding of densification mechanics of polymeric syntactic foams under compressive loading accounting for microballoon volume fraction, microballoon wall thickness, bonding between the microballoons and the matrix, and the crushing strength of microballoons. The authors further utilized multiple linear regression to understand the influence of structural and material parameters on its densification properties. Wang et al.[139] investigated how the strength distribution of a batch of hollow glass microspheres (HGM) influences the compression strength of syntactic foams. The authors discovered that the compressive strength of syntactic foams improved with an increase in HGM's strength.

The above research explored the syntactic foam composite's time-independent (**quasi-static**) mechanical properties. However, analyzing how mechanical properties of syntactic foam composite change under different strains

or loading rates is also essential, i.e., the strain-dependent (**dynamic**) mechanical properties. Woldesenbet et al.[148] analyzed the effect of density and strain rate on the properties of syntactic foam and showed a considerable increase in peak strength of syntactic foams for higher strain rates and higher density. Song et al.[128] investigated the dynamic compressive properties of an epoxy syntactic foam at various strain rates under lateral confinement with a split Hopkinson pressure bar. The authors discovered that the quasi-static and dynamic stress-strain behavior has an elastic-plastic-like shape, whereas an elastic-brittle behavior was observed under uniaxial loading. Li et al.[83] experimentally analyzed the compressive responses of glass microballoon epoxy syntactic foams within a range of strain rates. The authors combined testing results with finite element stress analysis to determine the foam's localized damage and failure modes. Shunmugasamy et al.[124] utilized microCT-scanning and scanning electron microscopy to understand the effect of high strain rate loading on the deformation and fracture characteristics of syntactic foams and further understand the strain rate dependence of failure mechanisms. Zhang et al.[160] investigated the compressive response of epoxy syntactic foam with strain rate and temperature dependency. The authors also developed a non-linear phenomenological model to describe the responses of syntactic foam and its temperature-strain rate equivalence. These works have shown the different approaches (experimental and analytical) to obtaining the strain-dependent mechanical properties of syntactic foam

composites. However, these analyses only focus on limited microballoon distributions by considering only a few samples. A detailed understanding of how stress-strain response relates to microballoon properties and distributions is needed to design these syntactic foams effectively. To achieve this, we will utilize Deep Learning methods to determine how the volume fraction and wall thickness of randomly distributed microballoons affect the mechanical properties of syntactic foams.

The emergence of Machine Learning methods facilitates research to predict the mechanical properties of composite materials with the graph neural network as an essential tool. Graph Neural Network is developed based on Deep Convolutional Neural Network[78] (DCNN) and Generative Adversarial Network[23] (GAN). Researchers have been focusing on solving engineering design and analysis problems with Graph Neural Networks, like [165, 67]. Regarding composite materials, Chen et al.[14] compared how different Machine Learning techniques, like regression model, DCNN, and Gaussian process, can accelerate the composite material design. Feng et al.[31] proposed a Difference-based Neural Network to enhance the stress distribution prediction within different composite micromechanical models, especially for models with stress concentrations in the stress distribution contours. Sepasdar et al.[121] proposed a modified U-Net framework to predict the damage and failure within microstructure-dependent composite materials. Feng et al.[35] further proposed a Physics-Constraint Neural Network to understand the forward

and inverse predictions of woven composite models in the mesoscale. Besides predicting the linear elastic mechanical properties with Machine Learning, researchers also utilized Machine Learning to predict the nonlinear constitutive behaviors and mechanical responses of composite materials, like the entire stress-strain curve. Hashash et al.[51] developed a Neural Network constitutive model to replace the commonly used integration procedures in Finite Element Analysis. Then a consistent material stiffness matrix is derived based on the Neural Network constitutive model instead of conventional plasticity-based models. This new model leads to efficient convergence of the Finite Element Newton iterations. Bos et al.[27] developed a Neural Network-based constitutive model to capture the elastic-plastic stress-strain curve. The authors proposed to sub-sample the stress-strain curve at several discrete points and then predicted the stress values at different discrete strain values. The final curve was obtained by interpolating the discrete points. However, this approach still needs several discrete points for prediction, and there are errors during interpolation. Yang et al.[152] combined principal component analysis (PCA) and convolutional neural networks to predict the entire stress-strain behavior of binary composite materials. The authors showed that the PCA could effectively transform the stress-strain curve into a latent space and the prediction error is less than 10%. Kosmerl et al.[77] proposed a Neural Network by combining a convolutional neural network and residual neural network to predict the stress-strain curve for single-walled car-

bon nanotube configurations. These methods have shown the promising aspect of Neural Networks in obtaining the non-linear stress-strain behaviors of a targeting model. However, one key drawback of the above methods is that we need a large training dataset to better predict and represent the latent space features. Such massive training datasets are usually extremely challenging to generate as they come from experiments or numerical simulations.

In this paper, we propose a **Parameterization-based Neural Network** (**PBNN**) where we represent the non-linear stress-strain response of the chosen composite (here hollow particle reinforced geometries) with a parameterized function space. The parameters in the function can be different for different stress-strain curves. Then, we utilize the concepts of self-supervised learning[69] and transfer learning[143] to effectively extract the latent features from the composite geometric model using an Encoder-Decoder Neural Network. The key benefits of our approach are:

1. We use an Encoder-Decoder Neural Network for latent feature extraction from composite geometries (named Feature Extraction module). This Feature Extraction module reduces the input dimension from a 256-by-256 image to a 128-by-1 vector, simplifying the following Neural Network prediction task. It is easier to generate different matrices to represent the composite geometries, while it is time-consuming to solve each model numerically.

2. We use a parameterized representation of the stress-strain curve to capture the shape of the true stress-strain response. Otherwise, we usually need a 'physically meaningful' or higher-order smooth function to represent the stress-strain curve. This parameterized representation vastly reduces the prediction size as it requires fewer data during training to achieve a relatively good prediction.

3. We propose a module named 'Modification module' that predicts an auxiliary term to increase the stress-strain curve prediction accuracy. This Modification module serves as a constraint by predicting an extra data point on the stress-strain curve. Then it modifies the stress-strain curve predicted through Neural Network by adding a carefully constructed polynomial equation.

4. Our proposed PBNN is not limited to the stress-strain curve prediction with a known function but works for other response prediction problems. For example, we can fit any arbitrary curve with a polynomial function, which will be the targeting parameterized function for our proposed PBNN.

4.2 Overview of the Machine Learning Framework

The PBNN framework consists of two key modules: 1) the Feature Extraction module and 2) the Curve Prediction module, as shown in Figure 4.1. The Feature Extraction module extracts a high-level feature vector from the syntactic foam geometry. Then the feature vector is brought into the Curve Prediction module, consisting mainly of a Dense module and a Modification module, to predict the final stress-strain curve. We perform the Machine Learning training on NVIDIA GeForce RTX 2080 SUPER with 3072 CUDA cores.

Feature Extraction Module

The framework for the Feature Extraction module is shown in Figure 4.2, which is constructed based on the Encoder-Decoder structure. The Encoder will extract the high-level features from the input model, and the Decoder will expand the extracted high-level features back to the input model. Here the Decoder is needed to train the Feature Extraction Module, as the loss function of the Feature Extraction Module is defined based on the input model. The module simplifies the Neural Network training problem by reducing the complex 256-by-256 image input into a 128-by-1 vector. This feature vector can be treated as a high-level equivalence of the corresponding input geometry. Then the prediction is simplified into

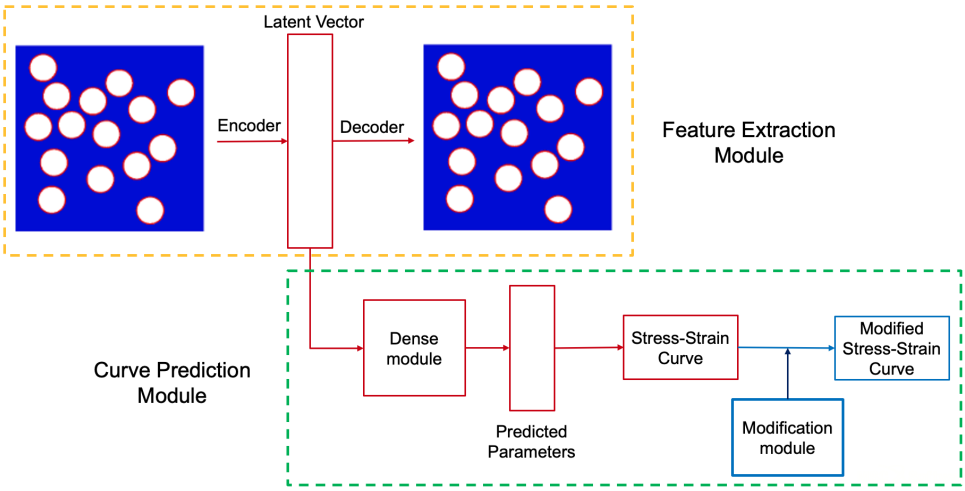

Figure 4.1: Overall framework for predicting the non-linear mechanical responses with PBNN: (1) Orange block is the Feature Extraction module, which extracts the high-level features (Latent Vector) of the syntactic foam geometry using an Encoder-Decoder structure. (2) Green block is the Curve Prediction module, which predicts the stress-strain curve from the extracted high-level features using a Dense module and a Modification module.

a problem as predicting the stress-strain curve from a 128-by-1 feature vector instead of a 256-by-256 image matrix.

Curve Prediction module and Modification module

The Curve Prediction module predicts the stress-strain curve from the extracted feature vector. This module consists of two main sub-modules: the Dense and Modification modules. The Dense module consists of three dense layers. The first two dense layers have 64 neurons at each layer, with a tanh activation function. A linear activation function follows the

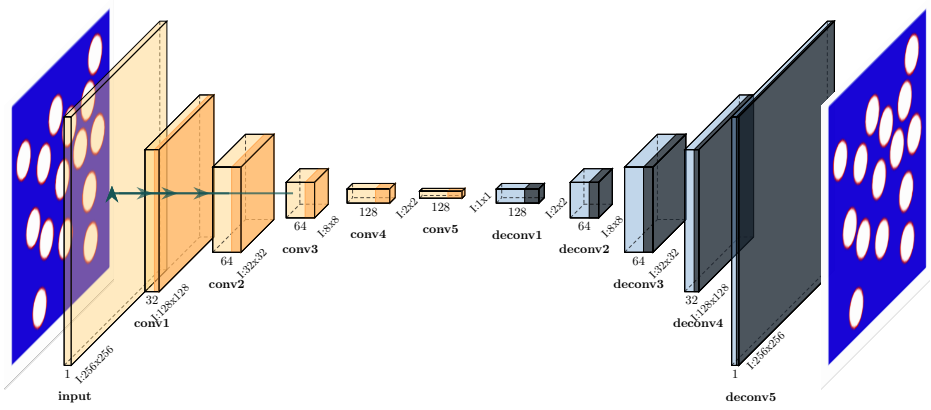

Figure 4.2: Feature Extraction module framework: the yellow color blocks belong to the Encoder module, and the blue color blocks belong to the Decoder module, as shown in Figure 4.1. Light yellow and blue blocks are convolutional and deconvolutional layers, respectively. The dark yellow and dark blue colors are the ReLU activation layer. Block 'conv5' outputs a 'Latent Vector,' the high-level feature vector of the syntactic foam geometry. It will be further used in the Curve Prediction module.

last dense layer and has a neuron size equal to the prediction size, which equals the size of function parameters plus one. For example, if the size of targeting parameters is three, the last dense layer will predict four neurons; three are function parameters, and the last is the 'end stress'. The 'end stress' is an auxiliary term that refers to the stress value at the maximum strain considered (15% strain in this paper). Predicted function parameters will determine the initial expression of the stress-strain curve. The Modification module will utilize the predicted 'end stress' to form a 'Modification function', which will be further added to the initial expression to reconstruct the initial curve by shifting it closer to the true stress-strain

curve.

The Modification module is a critical component of this prediction framework. By predicting the function parameters, the value of each point on the curve will be a non-linear function of all coefficients, making it extremely challenging to add constraints to the values of these points. Moreover, the shape of the function can be sensitive to given parameters, so adjusting the function parameters might significantly change the curve shape. Thus, we need to add additional constraints to the predicted curve but simultaneously keep the prediction physically meaningful. So we incorporated the Modification function to serve as the constraint. The Modification function can be expressed as Equation 4.1.

$$g(\lambda) = (\sigma_{end} - P(\lambda = 1.15))(\lambda - 1)^2/0.15^2 \tag{4.1}$$

Where λ is the principle stretch defined as the ratio of the deformed length to the undeformed length along the principal axes. When a uniaxial stress is applied, λ is related to uniaxial strain ϵ as $\lambda = \epsilon + 1$. σ_{end} is the auxiliary prediction term, denoting the predicted 'end stress' from the dense module corresponding to stretch λ=1.15. $P(\lambda)$ denotes the fitting function we choose to represent the stress-strain curve. Detailed expression of function $P(\lambda)$ considered in this paper can be referred to in Section 4.4. $P(\lambda = 1.15)$ denotes the true value of 'end stress' obtained from the fitting function. The term $P(\lambda = 1.15)$ ensures the 'end stress' of

the final stress-strain curve matches the predicted 'end stress'. '0.15' is the normalization term, representing the maximum strain for the stress-strain response considered. This normalization term ensures that the $g(\lambda = 1.15)$ represents the gap between true 'end stress' and predicted 'end stress'. This $g(\lambda = 1.15)$ is effectively pulling the 'end stress' of the predicted curve to the 'end stress' of the true curve. Since this normalization term depends on the maximum strain considered, it needs to be updated accordingly for a different dataset used. We designed the Modification function as a quadratic function because the stress prediction error generally increases as the strain value increases and is easier to construct. The base term $\lambda - 1$ ensures the initial point of the curve is not shifted after adding the Modification function. When λ=1, there is no change to the final stress-strain curve. At the 'end stress', when λ=1.15, we only end up with $\sigma_{end} - P(\lambda = 1.15)$. Then the final stress-strain curve expression will be $F(\lambda) = P(\lambda) + g(\lambda)$.

4.3 Syntactic Foam Computational Modelling

The syntactic foam micromechanical models are modeled using the Finite Element Method. A description of computational modeling, including boundary conditions and materials, is presented in Section 4.3 and 4.3. The parametric space of syntactic foam models and corresponding stress-strain curves are shown in Section 4.3.

Modelling and Boundary Value Problem

This paper considers 2D micromechanical syntactic foam models with randomly distributed microballoons in a matrix region. All micromechanical model dimensions are maintained at 0.295 mm x 0.295 mm, and the microballoon outer radius is maintained at 0.0225 mm. These micromechanical models are implemented within Finite Element software ABAQUS[134] with a mesh consisting of linear plane stress elements (CPS3 and CPS4). The mesh size is determined through mesh convergence analysis such that results are within 10% of the converged solution to reach a balance between convergence and computational cost. Since we have not considered strain-softening material behavior in our models, there is no pathological mesh dependency.

A schematic representation of the syntactic foam micromechanical model is shown in Figure 4.3. Here, Ω_m represents the matrix region, Ω_p represents the microballoon wall region, and Ω_v represents the hollow region or void inside the microballoons. Γ_{1-4} are the external boundaries of the micromechanics domain, and Γ_i are the interfaces between each microballoon and the matrix region. The volume fraction of matrix is given by $V_m = \frac{\Omega_m}{\Omega}$. The volume fraction of microballoons, including that of the particle wall and void, in a syntactic foam composite, is $V_{mb} = 1 - V_m = \frac{\Omega_p + \Omega_v}{\Omega}$.

Compressive displacement $\Delta_{applied}$ is applied on Γ_4. Γ_1 is fixed from deforming only along the y-axis and Γ_2 only along the x-axis. A flat boundary condition is considered on Γ_3 to achieve uniform deformation along the

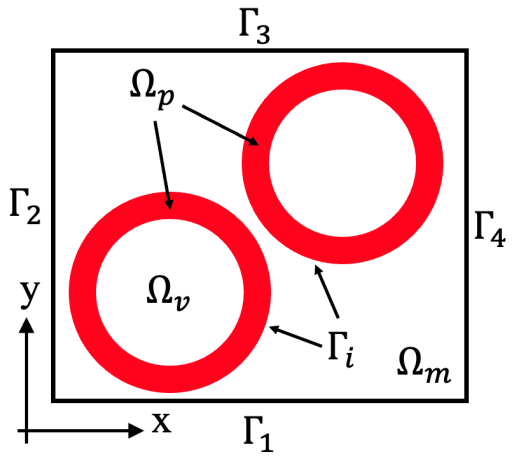

Figure 4.3: An example of 2D syntactic foam micromechanical model

y-axis. These boundary conditions are commonly used in micromechanics modeling of composites, and the corresponding boundary conditions are:

$$\begin{aligned} \hat{u}_x &= -\Delta_{applied} \quad \text{on} \quad \Gamma_4 \\ \hat{u}_x &= 0 \quad \text{on} \quad \Gamma_2 \\ \hat{u}_y &= 0 \quad \text{on} \quad \Gamma_1 \\ \hat{u}_y &= \text{constant on } \Gamma_3 \end{aligned} \tag{4.2}$$

Constitutive Materials Description

This paper considers High-Density Polyethylene (HDPE) as the material for the matrix. HDPE manifests a non-linear behavior under compression. The compressive stress-strain material data for HDPE is obtained from [65, 109], and is used as the input to fit an Ogden hyperelastic model.

Prabhakar et al.[109] has shown that the Ogden function effectively represents the stress-strain relationship for pure HDPE material. The glass microballoons (GMBs) are modeled as a linear elastic material. HDPE and GMB material properties can be found respectively in [109]. This study considers the interfacial behavior between the GMBs and HDPE matrix as perfectly bonded.

Parametric Space and Stress-strain Curves

The syntactic foam micromechanical model has several significant geometric parameters which govern the parametric space: (1) Number of microballoons: We consider the microballoon volume fraction to range from 10% to 50%. The volume fraction represents the ratio between the volume occupied by the microballoon and the whole model. A higher volume fraction implies more microballoons within a fixed matrix volume. (2) Position of microballoons: Each microballoon can be randomly located within the matrix. (3) Size of microballoons: We consider uniform microballoon outer diameters, but two different microballoon wall thicknesses are considered: 1.08 and 2.16 micrometers. The 1.08-micrometer thickness is denoted as 'thin-wall', and the 2.16-micrometer thickness is denoted as 'thick-wall'. The wall-thickness significantly affects the mechanical properties of syntactic foam composites, including stress-strain response, modulus, and failure modes [45]. Examples of different syntactic foam micromechanical models are shown in Figure 4.4.

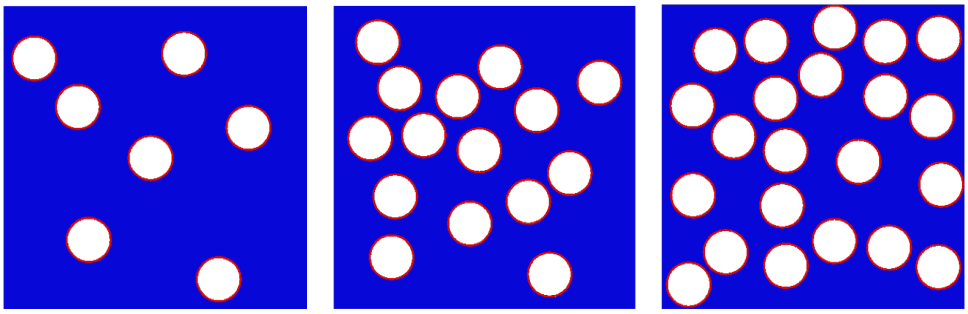

(a) (b) (c)

Figure 4.4: Example of 2D RUC models of thick-wall syntactic foam geometries with different volume fractions of (a) 10% (b) 30% (c) 50%: Blue color refers to the matrix, red color refers to the wall of microballoon, and white color refers to the hollow region.

This paper solves 6825 thin-wall and thick-wall syntactic foam models to obtain their stress-strain curves. Figure 4.5 shows sample stress-strain curves of thick-wall and thin-wall syntactic foam models with different microballoons volume fractions.

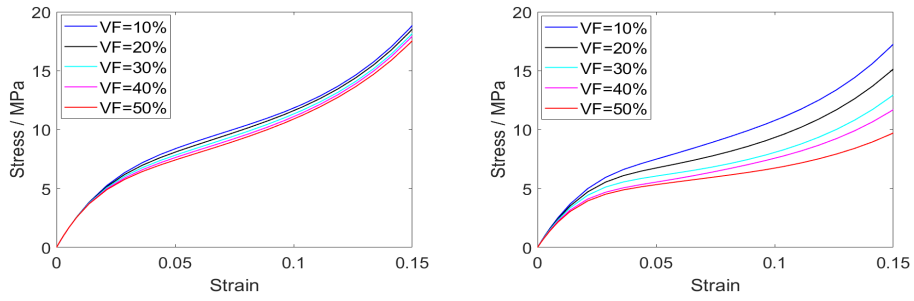

(a) (b)

Figure 4.5: Example of thick-wall and thin-wall syntactic foam stress-strain curves with different volume fractions: (a) thick-wall syntactic foam stress-strain curves; (b) thin-wall syntactic foam stress-strain curves. 'VF=10%' denotes 10% microballoon volume fraction

4.4 Machine Learning Model Inputs

Two inputs are used to set up the Machine Learning training process: the syntactic foam geometry and the corresponding stress-strain curve. We use 18,000 syntactic foam geometries, where 6825 models are solved to obtain their stress-strain responses. That is, 18,000 syntactic foam geometries were used to train the Feature Extraction module, and the 6825 syntactic foam models (thick-wall and thin-wall) were used to obtain stress-strain curves for further training the Curve Prediction module.

Syntactic Foam Geometry Representation

The 2D geometric representation of a syntactic foam includes three parts: the matrix labeled as '1', the microballoon wall labeled as '2', and the hollow region labeled as '0' shown in Figure 4.4 in blue, red, and white, respectively. Since the wall of the microballoon is very thin compared to the whole model, we construct a 256-by-256 Cartesian Map to ensure at least three layers of pixels along the microballoon wall thickness. Since boundary conditions are consistent for all models to calculate the stress-strain curve, boundary conditions are not considered part of the inputs.

Stress-Strain Curve Representation

The stress-strain curves for the syntactic foams are non-linear responses relating the compressive stresses with strains on the micromechanical

RUC models. To predict the stress-strain curves using Machine Learning algorithms, we can treat them as a piecewise function by connecting several discrete points or a smooth function with a particular expression. In this paper, we consider three different representations: (1) linear piecewise function, (2) cubic polynomial function, and (3) Ogden function. We utilize the Mean Squared Error (MSE), defined as Equation 4.3, to quantify the fitting errors of different representations.

$$\mathrm{MSE} = \frac{1}{n}\sum_{i=1}^{n}(Y_i - \hat{Y}_i)^2 \tag{4.3}$$

where n is the number of data points, Y_i is the i-th observed value and $\hat{Y}_i$ is the i-th predicted value.

Linear piecewise function representation

To balance the need between capturing the shape of the curve with a linear piecewise function and not making the Machine Learning prediction too difficult, we consider 21 uniformly distributed discrete strain values from 0 to 15%, corresponding to 21 discrete points along the stress-strain curve. Then the PBNN will attempt to directly predict these 21 discrete points to represent the stress-strain response. After obtaining the values for all 21 discrete points, the overall curve will be the union of several discrete linear piecewise functions in different subdomains. Each j-th subdomain consists of two points X_j and X_{j+1}, where X_j is the j-th discrete strain point

having the corresponding stress value of Y_j. The linear piecewise function in the j-th subdomain can be expressed as in Equation 4.4.

$$Y = F_j(X) = Y_j + \frac{Y_{j+1} - Y_j}{X_{j+1} - X_j}(X - X_j) \tag{4.4}$$

where $X \in [X_j, X_{j+1}]$. The ultimate linear piecewise function $P(\lambda)$ can be expressed as $P(\lambda) = \bigcup_j F_j(\lambda)$ $\mathtt{for}$ $\forall \lambda \in [X_j, X_{j+1}]$, $\lambda = \epsilon + 1$ is the principle stretch value in the defined domain of interest, as mentioned in Section 4.2 andϵ refers to the strain value. j is a collection of all subdomains.

Cubic polynomial function representation

A polynomial function can also be used to represent the stress-strain curve. By testing the fitting errors of polynomials with different order using polynomial regression[50], we pick the cubic polynomial function expression and calculate the fitting coefficients. Since we know the stress value is zero when strain is zero or λ is 1, we carefully constructed the cubic polynomial function as Equation 4.5.

$$P(\lambda) = a_3(\lambda - 1)^3 + a_2(\lambda - 1)^2 + a_1(\lambda - 1) \tag{4.5}$$

Here a_1, a_2, a_3 are the coefficients of the cubic polynomial function. The obtained coefficient values are shown in Figure 4.6. We notice that the cubic polynomial function representations have fitting mean squared errors between 0.41 to 0.92 for all models considered. As the stress value ranges

from 0 to around 20MPa, we believe such a fitting error is acceptable. Further, the cubic polynomial function can give a good representation of the stress-strain relationship.

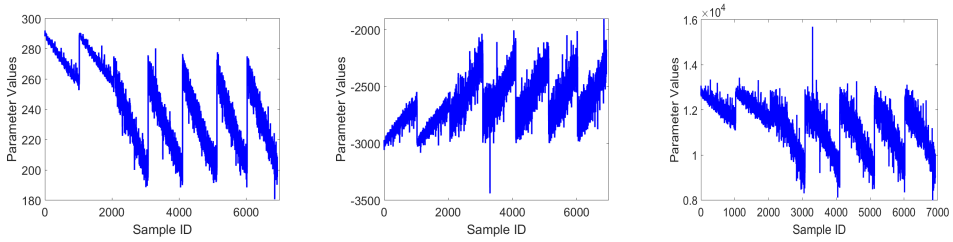

(a) (b) (c)

Figure 4.6: Values of parameters in the cubic polynomial functions for all stress-strain curves considered for: (a) a_1; (b) a_2; (c) a_3.

Ogden function representation

As the HDPE manifests a non-linear behavior under compression, the stress-strain curve can also be fitted using the Ogden function through the non-linear fitting[109]. We consider the incompressible case as shown in Equation 4.6. Detailed derivations of the expression can also be found in our prior work[109].

$$P(\lambda) = \sum_{i=1}^{n} \frac{2\mu_i}{\alpha_i}(\lambda^{\alpha_i - 1} - \lambda^{-\frac{1}{2}\alpha_i - 1}) \tag{4.6}$$

This paper considers the 3rd-order Ogden model, which has $n = 3$ in Equation 4.6. Through non-linear regression, we can obtain the values of coefficients in the Ogden function as shown in Figure 4.7. From non-linear

regression, we notice that the Ogden function fitting errors are between 0.02 to 0.54. Since α_i appears on the denominator, we want to keep the sign of α_i consistent for all models in the non-linear regression such that the Neural Network is less likely to predict a denominator value close to zero. This issue is avoided by adding constraints to the parameter values during non-linear regression, such that the sign of the regression coefficients will always be positive or negative. From Figure 4.7, the signs are consistent for all α_i. Consequently, the Ogden function can also represent the stress-strain curve.

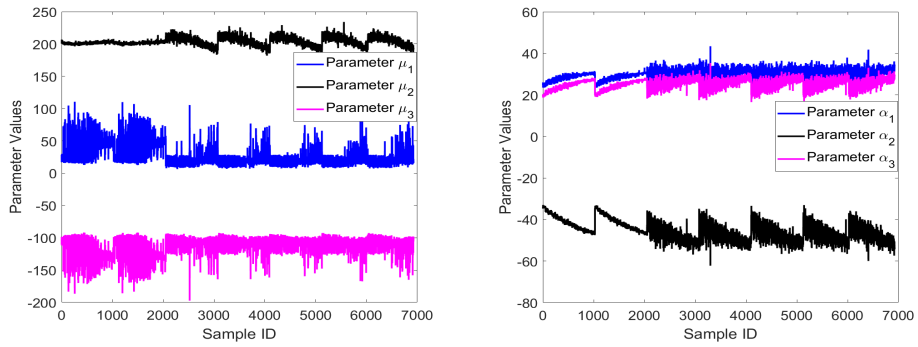

(a) (b)

Figure 4.7: Values of parameters in the Ogden functions for all stress-strain curves considered: (a) μ_1, μ_2 and μ_3; (b) α_1, α_2 and α_3.

Figure 7.9 shows how each representation compares with the true stress-strain data. Here we notice that the linear piecewise function (black curve) can accurately capture the trend of the stress-strain curve in a non-smooth manner. The cubic polynomial function (pink curve) gives a smooth representation of the curve but is less accurate than the linear piecewise

function. The Ogden function (red curve) gives the best approximation of true stress-strain curve, also a visually smoother solution than the linear piecewise function. This is because we use the Ogden hyperelastic model to fit the matrix material description for the FEA simulations that are used to generate the input composite stress-strain responses for this paper.

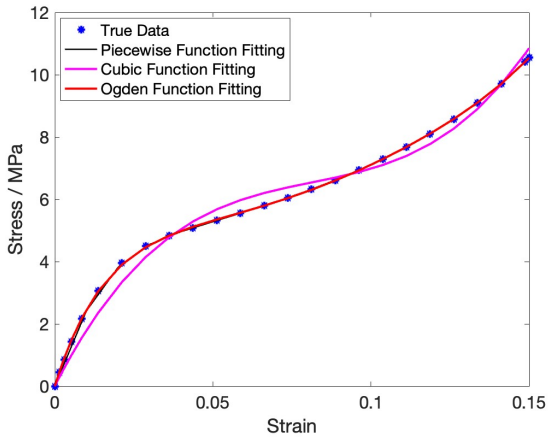

Figure 4.8: An example of stress-strain curve representation: blue dots are the true data, the black curve is fitted using linear piecewise function, the pink curve is fitted using the cubic polynomial function, and the red curve is fitted using the Ogden function.

Loss Function and Training Process

We propose different training processes for different curve representations. We utilize the Mean Squared Error (MSE) as the loss function for linear piecewise and cubic polynomial function representations. For both representations, The Neural Network uses MSE as a loss function

for both representations and is trained for 500 epochs, each with 30 steps. We propose a modified MSE loss function 'MMSE' for training the Ogden function representation. We know from the Ogden function that $P'(\lambda = 1) = \frac{dP}{d\lambda}$ at $(\lambda = 1) = \mu_1 + \mu_2 + \mu_3$. The term $P'(\lambda = 1)$ represents the slope at the initial point on the stress-strain curve and is independent of the choice of α_i. From our non-linear regression results in Figure 4.7, the value of μ_i is more spread out than α_i. Thus adding this constraint to the loss function is important to constrain the prediction of different μ_i and improve the prediction accuracy. Moreover, as the Modification function $g(\lambda)$ is a quadratic function of $\lambda - 1$, adding the Modification function will not change the value of $P'(\lambda = 1)$.
The MMSE can be written as Equation 4.7.

$$MMSE = MSE(y, \tilde{y}) + \alpha \cdot MSE[(P'(\lambda = 1) \mid y) - (P'(\lambda = 1) \mid \tilde{y})] \quad (4.7)$$

Where MSE is defined in Equation 4.3, α is a constant weight added to the loss term generated by initial slope $P'(\lambda = 1)$. In this paper, we use $\alpha = 0.01$. However, during the training process, we notice that directly training the Network with MMSE will lead to a blown-up prediction since the additional loss term creates more difficulty in finding the global minimum. So instead, we propose a '**hybrid**' training process: the Neural Network is trained for 500 epochs. For the first 300 epochs, we utilize MSE as the loss function. Then we utilize MMSE for the subsequent 100 epochs

and then use MSE again for the last 100. During this training process, MMSE tries to change the gradient descent direction from MSE and help avoid falling into saddle points or local minima.

4.5 Results and Discussion

In this section, we evaluate the performance of our Feature Extraction and Curve Prediction modules on different stress-strain curve representations. The Feature Extraction module is validated by checking if the 'Latent Vector' can effectively predict back to the original geometry. The Curve Prediction module is validated by checking how close the predicted curve is to the true curve. We randomly split the data into 60% training, 20% cross-validation, and 20% testing for all datasets used.

Feature Extraction Module Results

We first train the Feature Extraction module using 18000 syntactic foam geometries, with 60% training, 20% testing, and 20% cross-validation. Figure 4.9 shows the predicted syntactic foam geometries from the Feature Extraction module. We can see that the predicted syntactic foam geometries can capture most of the critical features of the syntactic foams, even for complex geometries with high volume fractions, like Figure 4.9(a) and (b).

Moreover, to quantitatively measure how the Feature Extraction Module

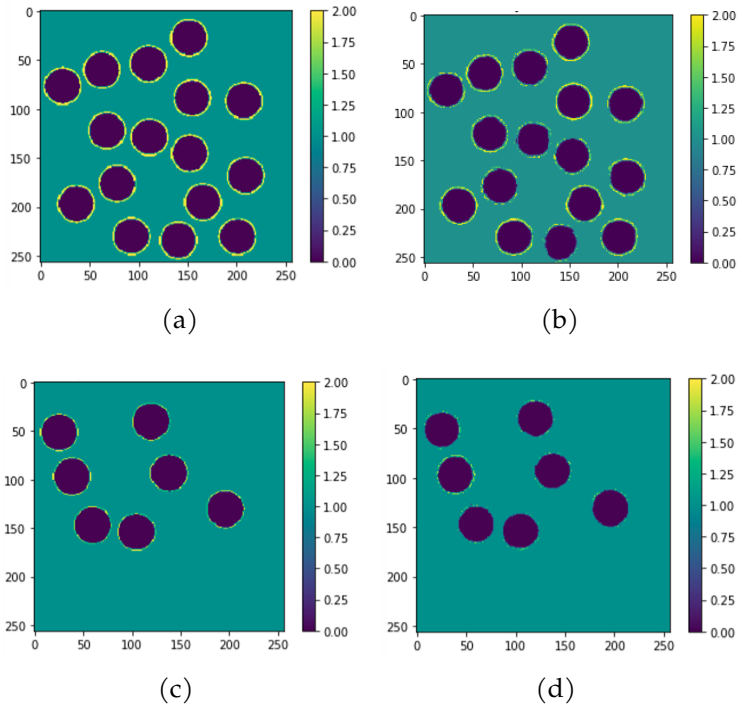

Figure 4.9: True syntactic foam geometry versus Predicted syntactic foam geometry obtained from the Feature Extraction module. Thick-wall syntactic foam - (a) real and (b) predicted geometry. Thin-wall syntactic foam - (c) real and (d) predicted geometry

performs, we define an error rate (ER) to measure the prediction accuracy, as:

$$ER = \frac{\sum_{i=1}^{N_x} \sum_{j=1}^{N_y} \mathbb{1}_{[G_o(i,j) \neq G_p(i,j)]}}{N_x * N_y} \tag{4.8}$$

where $N_x = N_y = 256$ is the size of the geometry Cartesian Map, mentioned in Section 4.4. G_o represents the original geometry Cartesian Map, and G_p represents the predicted geometry Cartesian Map. The error rate

calculates the ratio between incorrectly predicted node values in the Cartesian Map and the total Cartesian Map nodes ($N_x * N_y$). To evaluate how the training dataset affects the performance of the Feature Extraction Module, we first pick 2000 samples as the test set, and train the module with different training data sizes. We use three random split methods (we call random split seed) and calculate the error rate with different random splits to account for randomness.

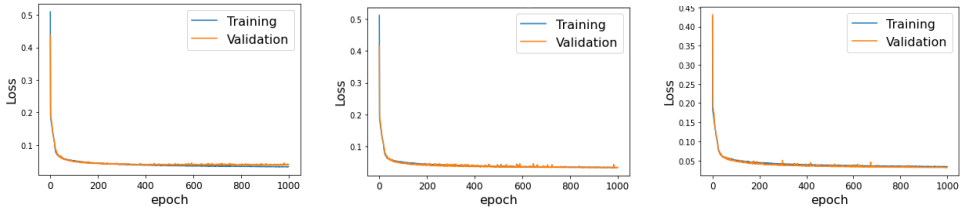

(a) (b) (c)

Figure 4.10: Training loss profile of Feature Extraction Module (a) using 7000 samples (b) using 10000 samples (c) using 12500 samples

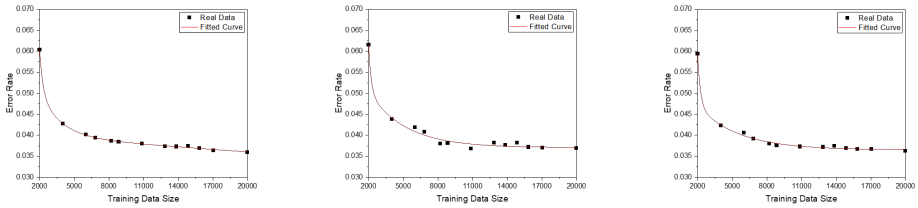

(a) (b) (c)

Figure 4.11: Prediction error rate of Feature Extraction Module, on 2000 testing samples (a) random split seed 1 (b) random split seed 2 (c) random split seed 3

Figure 4.10 shows how the training loss decreases as we increase the

training epochs (we run a total of 1000 epochs and each epoch has 40 steps) for training sample sizes of 7000, 10000, and 12500 each. We observe that the Feature Extraction Module optimization is converged within 1000 epochs. Further, Figure 4.11 shows how the prediction error changes with increasing training data size. Despite different random split methods, the prediction error rate decreases as we increase the training sample size. When the training data size is larger than 15000, we have a consistent prediction error rate below 3.5%. Thus in this paper, we choose a training data size of 18000 to train the Feature Extraction Module for extracting the corresponding high-level latent features of the syntactic foam geometries.

Curve Prediction Module Results

After fully training the Feature Extraction module, we can use the extracted feature vectors to predict the stress-strain curves using the Curve Prediction module. The prediction error is evaluated based on the errors at 21 uniformly distributed points along the curve (same as the discrete point locations when defining linear piecewise function). The errors are calculated based on Norm-2 Error (NE), defined in Equation 4.9.

$$NE = \sum_{i=1}^{n} (Y(i) - \hat{Y}(i))^2 \tag{4.9}$$

$n = 21$ represents the total size of the data points considered in one sample. The overall prediction errors are evaluated based on Mean Norm-2 Error

and Max Norm-2 Error, which calculates the average and maximum Norm-2 Error in the testing sample set. Table 4.1 shows the prediction errors of different stress-strain curve representation methods using PBNN. Besides, Figure 4.12 gives two examples of the Stress-Strain curve prediction using different representations.

Table 4.1: Curve Prediction Error for different curve representations with PBNN

	Mean Norm-2 Error	Max Norm-2 Error
Linear Piecewise Function	7.31	21.64
Cubic Polynomial Function	5.03	18.73
Ogden Function	5.89	14.89

Comparing the predictions for different representations, we can conclude that:

1. The Ogden function and cubic polynomial function representations give similar prediction accuracy by providing a smooth curve close to the true curve. The polynomial function representation has a lower Mean Norm-2 Error, but Ogden function representation has a lower Max Norm-2 Error. This is because the cubic polynomial function has fewer parameters to train, making obtaining a better prediction during the training process easier. However, as shown in Figure 7.9, the cubic polynomial function has fitting errors to the true curve.

2. The linear piecewise function representation gives a relatively worst prediction by having the most significant prediction error. Moreover,

the linear piecewise function gives a non-smooth prediction, and the relative relationship between adjacent points might not obey the physical truth (like the horizontal line at the beginning of the blue curve in Figure 4.12(a), which is not true). Furthermore, we potentially introduce an additional error if we attempt to smooth the prediction obtained from the linear piecewise function.

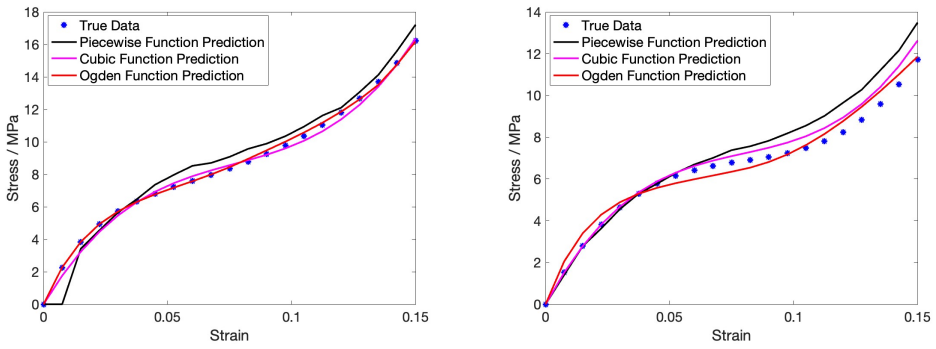

(a) (b)

Figure 4.12: Predicted stress-strain curves from the Curve Prediction module: (a) Example 1 (b) Example 2. The blue dots are the true data, the black curve is fitted using the linear piecewise function, the pink curve is fitted using the cubic polynomial function, and the red curve is fitted using the Ogden function.

Importance of Feature Extraction module, Modification module, and Hybrid Training Process

We introduce the ideas of different modules and training methods for PBNN. To understand the importance of the different aspects in PBNN,

like the Feature Extraction module, Modification module, and the hybrid training process (only for Ogden function representation), this section compares PBNN's prediction error with several baseline models. We use the Ogden function representation for illustration purposes.

Baseline model 0 We first choose a baseline model that always outputs the mean stress-strain curve from the training dataset. The norm-2 error for the Baseline model 0 represents the variance of the testing dataset. To show the improved efficacy of other baseline models proposed, their norm-2 error should be lower than that of the Baseline model 0. Figure 4.13 shows a comparison between the mean curve and the training (a) and testing (b) datasets.

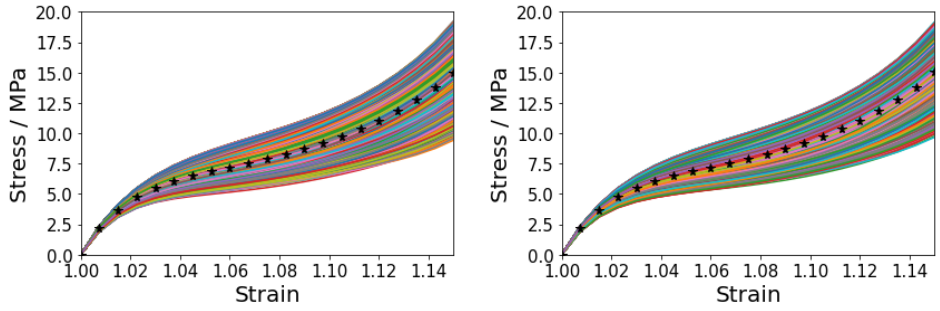

(a) (b)

Figure 4.13: Comparison between the mean curve of the Baseline model 0 (**black asterisk**) and (a) training dataset (b) testing dataset

Baseline model 1 As discussed in Section 4.2, we utilize the Feature Extraction module to extract latent space features using easily obtained

syntactic foam geometries. To validate the effectiveness of the Feature Extraction module, we consider a baseline model in which we directly use an Encoder structure (as discussed in Figure 4.2) to predict the Ogden parameters (named Baseline-1).

Baseline model 2 To validate how the Modification module performs, we choose another baseline model by removing the Modification module from PBNN (named Baseline-2). We compare the prediction between PBNN with and without the Modification module. The detailed frameworks for the two models are shown in Figure 4.14, with and without the blue dashed line modules.

Baseline model 3 (only for Ogden function representation) To understand how our proposed hybrid training improves the prediction accuracy, we consider another baseline model (named Baseline-3), which has the same structure as PBNN but only uses MSE as the loss function instead of MMSE.

Prediction results Here we show the prediction accuracy using our training data with 6825 syntactic foam models. Three different data-splitting methods are used, and the average error is calculated. The results are shown in Table 4.2. From the results, we notice that:

1. The Baseline-0 has the largest mean Norm-2 Error compared to all the other models, while the max norm-2 error is lower than Baseline-

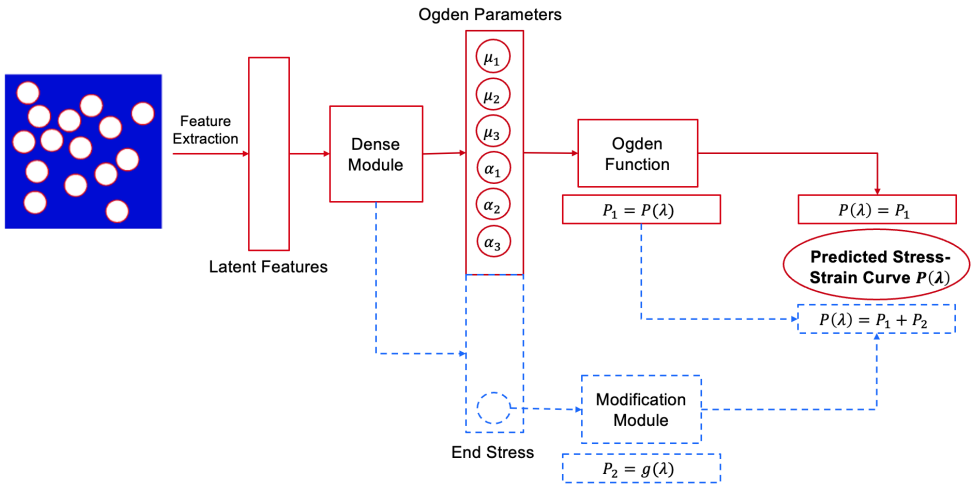

Figure 4.14: Stress-Strain curve prediction using PBNN framework without modification module (Baseline-2) is shown using red color. PBNN with modification module is shown by adding blue dashed line modules to Baseline-2. Baseline-2 directly predicts the Ogden parameters from extracted latent features and constructs the Stress-Strain curve with the Ogden function. While PBNN also uses the Modification module to generate the Modification function P_2 and constructs the Stress-Strain curve by adding the Ogden function and Modification function.

1 and Baseline-2. This means Baseline-1 and Baseline-2 could make predictions beyond the range of the test set curves. On the other hand, Baseline-3 and PBNN have better predictions than Baseline-0 for both mean norm-2 error and max norm-2 error.

2. Baseline-2 has slightly better prediction than Baseline-1, meaning that the Feature Extraction module can extract the high-level features better and improve the curve prediction accuracy.

3. Baseline-3 significantly improves the prediction accuracy compared

to Baseline-1 and Baseline-2, proving that the modification module is essential to achieving better prediction accuracy.

4. PBNN can give a better prediction than Baseline-3, proving that the hybrid training procedure improves the prediction accuracy.

Table 4.2: Curve Prediction Error for different frameworks

	Mean Norm-2 Error	Max Norm-2 Error
Baseline-0	8.14	18.26
Baseline-1	7.51	30.12
Baseline-2	6.69	30.08
Baseline-3	6.14	18.18
PBNN	5.89	14.89

Moreover, we can visualize the effect of the modification module in Figure 4.15, which validates the predictions of PBNN and Baseline-2 for two randomly picked test datasets (test set 1 and test set 2) from the total 20% test data set. The graph shows that the modification module could effectively push the initially predicted curve closer to the true curve and enhance the stress-strain curve prediction accuracy.

4.6 Conclusions

This paper proposes a Parameterization-base Neural Network (PBNN) framework to predict the non-linear stress-strain responses of composites. We choose syntactic foam composites to develop these frameworks due to their complex internal architecture and corresponding mechanical

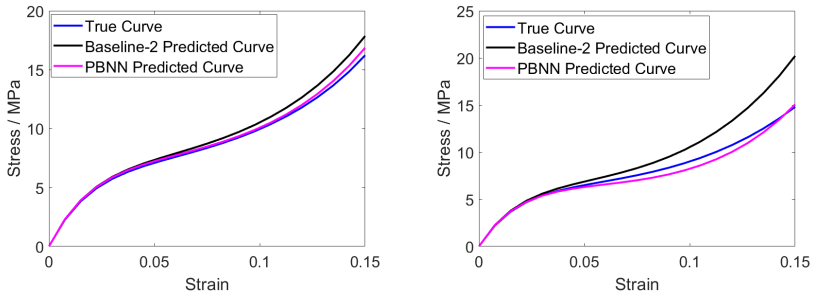

(a) (b)

Figure 4.15: Importance of the modification module: stress-strain curve prediction between Baseline-2 and PBNN on test set samples: (a) Curve prediction on test sample 1 (b) Curve prediction on test sample 2. The blue curve is the true Stress-Strain curve, the green curve is the predicted curve from Baseline-2, and the red curve is the predicted curve from PBNN.

responses. Instead of predicting discrete points along the stress-strain curve, we propose the stress-strain curve representations using the cubic polynomial function and Ogden function and utilize PBNN to predict corresponding function parameters. This vastly reduces the computational cost and data size needed for training. By comparing different baseline models, we further show that PBNN achieves a better prediction accuracy of the stress-strain curve than other baseline models.

The main conclusions and contributions of this paper are:

1. This is the first attempt to our knowledge to predict non-linear stress-strain responses by treating them as a parameterized function, especially for the complex composite material analysis.

2. We have shown that our method could simplify the Machine Learn-

ing problem and generate a 'physically meaningful' prediction by utilizing the Feature Extraction module and the Modification module. The Feature Extraction module extracts the high-level features from the microstructure geometry into a latent vector, serving as reduced-order input to the ML framework. The Modification module improves the prediction accuracy by referring to an auxiliary prediction and reconstructing the predicted stress-strain curve expression.

3. We have demonstrated that PBNN can predict general polynomial functions (like a cubic polynomial function) or complex highly nonlinear functions (like an Ogden function) from internal material microstructures.

4. Our method is not limited to syntactic foam or composite material stress-strain prediction, and we can use a similar approach for all curve-related predictions. Our method can also be extended to develop knowledge/physics-guided Machine Learning algorithms with the proposed Feature Extraction module and Modification module.

5 PHYSICS-CONSTRAINED NEURAL NETWORK FOR THE ANALYSIS AND FEATURE-BASED OPTIMIZATION OF WOVEN COMPOSITES

Haotian Feng, Sabarinathan P Subramaniyan, Pavana Prabhakar, Physics-Constrained Neural Network for the Analysis and Feature-Based Optimization of Woven Composites, arXiv preprint arXiv:2209.09154 (2022).

Abstract

Woven fabrics play an essential role in everyday textiles for clothing/sportswear, water filtration, and Geotech walls, to reinforcements in stiff composites for lightweight structures like aerospace, sporting, automotive, and marine industries. Several possible combinations of weave patterns and material choices, which comprise weave architecture, present a challenging question about how they could influence the physical and mechanical properties of woven fabrics and reinforced structures. In this paper, we present a novel Physics-Constrained Neural Network (PCNN) to predict the mechanical properties like the modulus of weave architectures and the inverse problem of predicting pattern/material sequence for a design/target modulus value. The inverse problem is particularly challenging as it usually requires many iterations to find the appropriate

architecture using traditional optimization approaches. We show that the proposed PCNN can effectively predict weave architecture for the desired modulus with higher accuracy than several baseline models considered. We present a feature-based optimization strategy to improve the predictions using features in the Grey Level Co-occurrence Matrix (GLCM) space. We combine PCNN with this feature-based optimization to discover near-optimal weave architectures to facilitate the initial design of weave architecture. The proposed frameworks will primarily enable the woven composite analysis and optimization process and be a starting point to introduce Knowledge-guided Neural Networks into the complex structural analysis.

5.1 Introduction

Woven fabric, a textile material, is formed by weaving or interlacing warp and weft fiber bundles in the orthogonal directions. Woven fabric has a wide range of applications, from everyday textiles for clothing and fashion to reinforcements in stiff composites for lightweight structures like aerospace, sporting, automotive, and marine industries [98, 73, 16, 39]. Possible combinations of weave patterns and choices of materials for the warp/weft fiber bundles present a promising yet challenging question about how they could influence corresponding physical and mechanical properties. To that end, we present a novel **Physics-Constrained Neural**

Network (PCNN) to predict the mechanical properties like the modulus of weave architectures (weave pattern, weave material sequence) and the inverse problem of predicting pattern/material sequence for a design/-target modulus value. Though these frameworks can be applied to any woven fabric, we consider **woven composites** as our case study to develop and demonstrate their phenomenal advantage.

Woven composites are stiff textile composites with woven fabrics with high-strength fibers like Carbon, glass, Aramid, etc., reinforced within polymers. These composites have drawn significant interest from industry and academia due to the flexibility to change mechanical properties, high strength-to-weight ratio, high production rate, and structural durability[90]. Due to these significant advantages, textile composites have been used in the aerospace, sporting, automotive, and marine industries. To better understand woven composites, many researchers have been focusing on exploring the mechanical properties of woven composites. Research to find woven composite's mechanical properties largely relies on analytical representation or numerical analysis like Finite Element Analysis (FEA). Research to understand woven composite first focuses on the analytical representation of the woven composite model. Naik et al.[100] utilize a shape function to define the woven fabric geometry by considering actual strand cross-section geometry, the possible gap between adjacent strands, and undulation and continuity of strands along the warp and fill directions. Jiang et al.[68] present a three-dimensional representative

volume-element model to study the micromechanical behavior of woven fabric composites. The model has been shown to agree with published experimental data very well. Moreover, the relationship between geometric parameters and the macro mechanical behavior of the composites can be obtained from the model. Khan et al.[75] propose a simplified mathematical micromechanics model for calculating the mechanical properties of the plain weave composite using FEA. The new model considers geometric parameters like yarn undulation and interactions between warp and fills tows to help generate an FEA mesh close to the actual fabric. Although the analytical approach is computationally efficient, it cannot accurately represent the model's complexity and mechanical responses. Thus several researchers focus on utilizing FEA to analyze the woven composite models numerically. Ishikawa et al.[60] conduct the one-dimensional micromechanical analysis on the woven composite to derive the upper and lower bounds of stiffness and compliance constants. The result is further validated with 2D FEA. Whitcomb et al.[146, 145, 144] utilize FEA to analyze the three-dimensional stress of plain woven composite and the boundary effect of woven composites. Gowayed et al.[42] present different types of fiber and fiber arrangements in fiber-reinforced polymer woven fabrics. The impact of fiber assembling into yarns and fabrics is also discussed in the paper. Dong et al.[26] utilize experimental and Finite Element analysis to find the plain weave composite's thermal conductivity and further compared the conductive behavior with unidirectional lamina. These methods

have shown the power of FEA in analyzing woven composite models by including much more geometric complexity than the analytical approach. However, using FEA to explore the mechanical properties of the woven composite is time-consuming as each woven model needs to be solved numerically. The time consumption is even more for optimizing the weave patterns for specified properties.

The emergence of Machine Learning (ML) methods research largely facilitates understanding composite materials and predicting the corresponding mechanical properties. Among existing ML algorithms, Deep Convolutional Neural Network[78] (DCNN) and Generative Adversarial Network[23] (GAN) are the most widely used. DCNN is a class of deep neural networks consisting of several convolutional, pooling, and fully connected layers. DCNN has been widely used in different fields, including image classification[78], recommender system[155], image segmentation[161], and natural language processing[22]. GAN is developed similarly to game theory, where Nash equilibrium is reached when the model converges. There is a generator and a discriminator Network in GAN. GAN has been used in different fields, including unsupervised learning[119, 12], semi-supervised learning[129], fully supervised learning[164], and reinforcement learning[156]. Regarding ML's application in composite material analysis, Wei et al.[141] demonstrate that machine learning methods like support vector regression, Gaussian process regression, and convolutional neural network (CNN) are useful tools

to predict the effective thermal conductivities of composite materials and porous media. Chen et al.[14] give an overview of how different Machine Learning algorithms can accelerate composite material research, including several different regression models, Neural networks (especially CNN), and the Gaussian process. Feng et al.[31] propose a Deep Learning method to predict composite micromechanical models' stress distribution contours using a Difference-based Neural Network, where the Neural Network focuses on predicting the differences to a reference sample. Bang et al.[7] propose a framework to identify the defects within composite material by integrating thermo-graphic images of composite with deep learning. Liu et al.[89] propose a new failure criterion for fiber tows in woven composite by combining mechanics of structure genome and a deep neural network model. Nardi et al.[101] utilize the Artificial Neural Network to predict the thermoforming process of thermoplastic composites. The authors focus on the glass fiber-reinforced polyetherimide woven composite and discuss the essential features needed for accurate predictions of the temperature fields over the thermoforming process. The authors further discuss the potentiality of using Machine Learning to determine the optimal range of the process parameters. Sepasdar et al.[121] propose the modified U-Net network to predict the damage and failure in microstructure-dependent composite materials. Gu et al.[43] use ML to analyze the strength and toughness of 2D checkerboard models for 2D printed bi-material composites. The authors used a single-layer convolutional neural network

with two binary classifiers. Further, Abueidda et al.[2] also focus on a 2D checkerboard model and utilized a genetic algorithm optimizer to optimize a checkerboard composite pattern to obtain a model with maximum strength and toughness based on different volume fractions. This research has proven the potentiality of accelerating woven composite design and analysis with ML.

Although insightful, these above frameworks are limited to predicting material properties for a given pattern or optimizing through heuristic searching, which is relatively easy to handle. On the contrary, the ability to solve the inverse design problem, which predicts patterns for target mechanical properties, can be more challenging and beneficial. Within woven composites, it could save a massive amount of time otherwise invested in testing weave design iterations. Feng et al.[32] considered 2D woven composite with a single material and proposed the GAN-based framework for the inverse design problem. The research has shown the potentiality of utilizing Neural networks with a relatively decent error rate of around 7%. Similarly, Chen et al.[19] consider the inverse design problem of the checkerboard composite model using generative inverse design networks called GIDN. GIDN consists of a predictor and a designer, like the idea of GAN. The predictor is first trained with training data, then trained weights in the predictor are directly assigned to the designer as non-trainable parameters. The designer further provides an optimized design from the initial Gaussian distributed design. GIDN has outperformed conventional

gradient-based topology optimization and gradient-free algorithms for a stiff-soft bi-material composite model. This method brings promising ideas to optimize the composite material, while this GAN-based approach does not build the connection between the mechanical properties of composite material to its geometry. Also, Neural Network-based optimization is hard to be understood in the physical space.

Thus, this paper aims to solve two problems related to 2D woven composite, whose pattern can also be represented as a checkerboard model: (1) How can we build a bi-directional bridge between woven composite architecture and its mechanical properties? (2) How to optimize the woven composite's mechanical properties using 'physically meaningful' features, so we can optimize the woven composite properties by directly manipulating physical and geometric parameters?

5.2 Motivation and Overview

This section presents an overview of the overall targets of the research presented in this paper and the general Machine Learning approaches that we use for woven composite prediction and optimization.

Motivation and Research Tasks

As mentioned before, we focus on solving two problems related to understanding woven composite mechanical properties and optimizing the

woven architecture to achieve better overall in-plane modulus. Woven composite architecture could be determined by different combinations of weave patterns and material sequences. For example, a 6-by-6 woven composite model will have 2^{36} different patterns and $2 * n^6$ different material sequences, where n is the number of materials to choose from. Thus, it is essential to quickly and accurately obtain the mechanical properties of different woven composite architectures to determine the woven architecture that fits the problem of interest. Besides understanding the mechanical responses of woven composites, optimization is also critical to minimizing the structure's stresses, weight, or compliance for a given amount of material and boundary conditions. Through optimization, we want to determine the most advantageous structure or material distribution inside the domain of interest for different design objectives, like having the lowest cost or highest mechanical properties.

In this paper, we consider two different woven composite models: single-material and bi-material woven composite. Single-material woven composite is made of one material for the whole model, and bi-material woven composite is made of two materials we consider. Specifically, we will consider three Machine Learning tasks (an overview of the three tasks is represented in Figure 5.1) as follows:

1. **Task 1**: Build the connection between woven composite architecture (pattern + material) and corresponding in-plane moduli. We will focus on the following tasks: (1) Forward Direction Prediction (FDP):

predicting from woven composite architecture to the corresponding modulus. (2) Backward Direction Prediction (BDP): predicting from woven modulus to its architecture. We decouple the BDP problem into two sub-problems: prediction from weave in-plane modulus and material sequence to its pattern (named as BDPa) and prediction from weave in-plane modulus and pattern to its material sequence (named as BDPb).

2. **Task 2**: Propose a feature-based woven composite optimization strategy to find the woven composite with the highest overall in-plane modulus. Specifically, the optimization strategy is developed based on regression analysis using Gray Level Co-occurrence Matrix (GLCM) features from weave patterns and physical space features from weave material sequences. From the regression analysis, we can determine whether each feature is positively or negatively correlated with the woven composite's overall in-plane modulus and further optimize the pattern based on the relationship.

3. **Task 3**: Discover the near-optimal woven composite design using the methods developed in Task 1 and Task 2.

For **Task 1**, to solve the FDP problem, we utilize Deep Convolutional Neural Network (DCNN) to extract high-level features from the woven composite model and predict the in-plane modulus from its architecture. The BDP problems are more challenging than the FDP problem since the in-

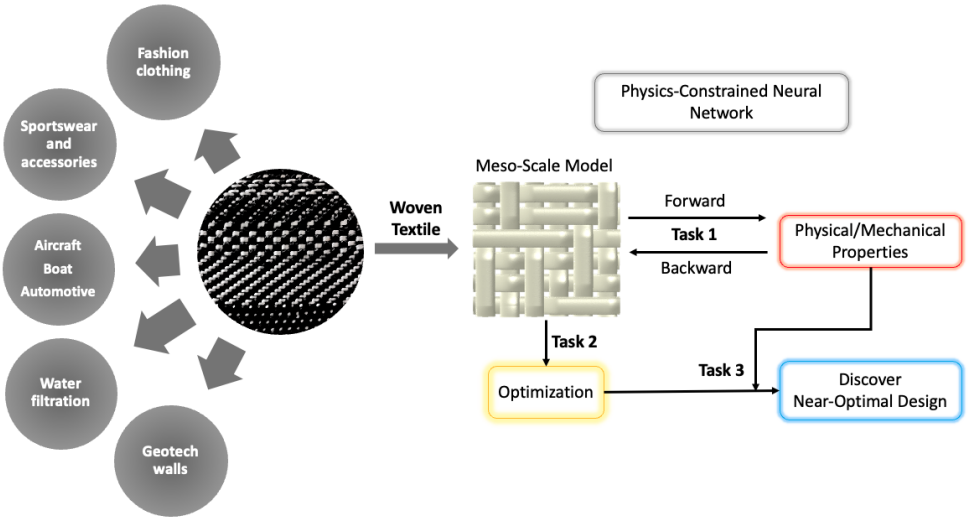

Figure 5.1: Overview of three Machine Learning tasks: (1) **Task 1** builds the bridge between woven composite and its physical/mechanical properties. Task 1 is split into Forward Direction Prediction (FDP) and Backward Direction Prediction (BDP) problems. BDP is further split into BDPa and BDPb, depending on predicting the weave pattern or predicting the weave material sequence. (2) **Task 2** proposes the optimization strategy on woven composite for achieving better physical/mechanical properties (like higher strength) (3) **Task 3** discovers the near-optimal woven composite design using the methods developed in Task 1 and 2.

plane modulus can be sensitive to weave patterns and material sequences. Incorrect prediction at a single position in the pattern or material sequence could significantly change in in-plane modulus. Moreover, we will show that woven composite with different patterns could have similar in-plane modulus. Such similarity forms one-to-many mapping for BDP problems. So a purely data-driven Neural Network is hard to achieve high accuracy in BDP problems. To constrain the predictions for BDP problems, we combine the idea of the existing Physics-Informed Neural Network (PINN)[94] and

transfer learning[104, 143], and then propose the **Physics-Constrained Neural Network (PCNN)**, which embeds the existing physics knowledge into the Neural Network to constrain the prediction. Specifically, PCNN will first utilize a similar structure as deep convolutional Autoencoder[6] to extract high-level features from the input data and make predictions based on these extracted features. Then, the PCNN will simultaneously embed our physics knowledge in the prediction layer and contribute certain losses to the loss function. Here, the physics knowledge refers to the relationship between woven composite architecture (pattern + material sequence) to its corresponding modulus, which comes from the trained DCNN in the FDP problem. We further validate that our proposed PCNN could enhance prediction accuracy compared to many widely used Machine Learning frameworks for BDPa and BDPb problems.

For **Task 2**, we first consider weave pattern optimization. Each weave pattern can be represented as a checkerboard model and can be treated as a type of texture. Then we extract texture features from the weave pattern. Texture features describe the spatial distribution of pixels (cells) which reflect objects' roughness, smoothness, granularity, and randomness. Common texture feature extraction methods include statistical, structural, and spectral methods. This paper utilizes the statistical method and proposes the GLCM feature-based optimization strategy. GLCM, referring to Gray-Level Co-Occurrence Matrix, is a statistical method of examining texture that considers the spatial relationship of pixels[120]. The GLCM features

characterize an image's texture by calculating how often pairs of pixels with specific values and in a specified spatial relationship occur in an image and then extracting statistical measures from the matrix. Since GLCM can measure the texture roughness, coarseness, and other properties in one calculation, it has been the primary method to describe texture-related methods in the field of medical sciences (CT scans, MRI)[168, 125], landscape analysis[48] and image-based defect detection[113]. In this paper, specifically, we use Haralick texture features[49]. The relationship between extracted GLCM-based Haralick features and the corresponding woven modulus can be determined through regression analysis to guide weave pattern optimization. Then we further consider weave material sequence optimization. Two vectors can represent the material sequence, and each vector describes the material sequence for horizontal and vertical yarns. We consider statistical features directly from the material sequence vector, including mean, median, and standard deviation. Similarly, from regression analysis, we can find out how each statistical feature is correlated with the in-plane modulus and find out the optimal material sequence from the regression model. Finally, the regression models from pattern and material sequence can be used to optimize a given woven architecture. The regression models can be combined with PCNN to provide optimal woven composite architecture at the initial design stage.

Overview of Proposed Machine Learning Framework

In Figure 5.2, we present an overview of the proposed Machine Learning framework for the two tasks considered in this paper. First, weave patterns and materials are picked such that each woven composite model is uniquely defined. Then by applying boundary conditions, we can calculate the corresponding in-plane modulus through FEA. After obtaining the weave pattern, material sequence, and corresponding in-plane modulus, we can start the Machine Learning process: (1) For FDP, we design a deep convolutional neural network that takes the weave pattern and material sequence as inputs and outputs the in-plane modulus. (2) For BDPa, we design the **Physics-Constraint Neural Network** (**PCNN**) that takes in-plane modulus and material sequence as inputs and predicts the pattern that matches the required in-plane modulus. For BDPb, we design another Physics-constraint Neural Network similar to BDPa, which takes the pattern and in-plane modulus as inputs instead and predicts the possible material sequence that matches the required in-plane modulus. In this paper, we consider single-material and bi-material woven composites. As a constant vector can represent the material sequence for the single-material woven composite, it will not serve as input to train the Machine Learning framework. For bi-material woven composite, both weave pattern, material sequence, and corresponding in-plane modulus will be inputs to Neural Network.

Throughout the paper, the machine learning framework is implemented

in TensorFlow 2.5.0 and trained on NVIDIA GeForce RTX 2080 SUPER with 3072 CUDA cores and 1815 MHz frequency. We provide access to our implemented Machine Learning code on our GitHub page, as mentioned in the "Data Availability" section at the end of this paper. The GitHub page provides implementations of our proposed Neural Networks, our baseline models used for comparison purposes, and the training data used in this paper.

5.3 Finite Element Method for Training Data Generation

As introduced in Section 6.1, the woven composites are formed by interweaved yarns impregnated with a resin matrix. The woven composite's effective mechanical property depends on the considered material's property, the cross-sectional geometry of yarn, and the weave pattern. In this paper, we utilize FEA to determine the in-plane modulus of woven composite (E_1, E_2, G_{12}) based on different combinations of weave pattern and material sequence. FEA is performed on a repeated unit cell (RUC) to understand the influence of weave patterns on the composite's in-plane effective properties. The weave is modelled using TexGen [87], where all the geometrical input parameters are listed in Table 5.1.

The FEA is divided into two stages: First, the influence of the weave pattern for single-material woven composites is analyzed. Second, the same pro-

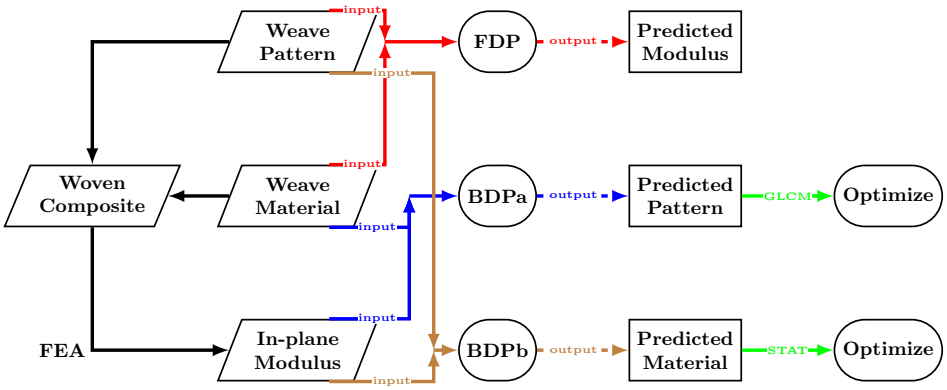

Figure 5.2: Overview of the proposed Machine Learning framework: (1) Black arrows represent the FEA process, (2) Red arrows represent the FDP problem, (3) Blue and Brown arrows represent two BDP problems: BDPa and BDPb. Trapezium blocks are inputs to the Machine Learning framework. Initially, we have weave patterns and material sequences; then, these models are brought into Finite Element solver ABAQUS[134] to find the corresponding in-plane modulus. Circular blocks represent different Machine Learning tasks: FDP, BDPa, and BDPb. Square blocks are the predictions for different Machine Learning tasks. Solid lines before circular blocks represent inputs to Neural Network, and dashed lines represent outputs. The solid green line and rounded corner blocks are the optimization modules. We introduce feature-based optimization for pattern and materials sequence, using GLCM and physical space statistical features.

Table 5.1: Geometrical parameters for finite element modeling

Length L	Width W	Height H	Yarn spacing	Yarn height	Yarn width
6mm	6mm	0.4mm	1mm	0.2mm	0.8mm

cess is extended to bi-material woven composites with two different fiber materials. The homogenized mechanical properties of the fiber bundles embedded in the polymer matrix are shown in Table 5.2, which are calculated using Chamis micro-mechanical model[18]. The volume fraction

of fiber is assumed to be 76% in this paper. Initially, the TexGen python scripting generates 9000 random weave patterns with carbon fiber yarns in woven composites. Later, another 9000 random weave patterns with random hybrid carbon-kevlar woven composites are generated. Each geometric model is exported as an input file with linear tetrahedron elements and periodic boundary conditions. In this paper, edge forces are applied in different directions. The corresponding displacement values are extracted from the applied tensile (shear) loading to evaluate the effective in-plane mechanical properties. A detailed explanation of boundary condition implementation can be found in Li et al.[84]. After preprocessing, the input file is imported into ABAQUS to determine the effective in-plane mechanical properties from the stress and displacement field.

Table 5.2: Homogenized material properties of fiber yarn embedded in polymer matrix

	E_1 (GPa)	E_2 (GPa)	E_3 (GPa)	G_{12} (GPa)	G_{13} (GPa)	G_{23} (GPa)	ν_{12}	ν_{13}	ν_{23}
Carbon yarn	183.1	9.67	9.67	5.66	5.66	3.37	0.23	0.23	0.43
Kevlar yarn	116.03	3.96	3.96	2.45	2.45	1.69	0.35	0.35	0.45

5.4 Machine Learning Model Inputs

We will focus on establishing the bridge between weave pattern, material sequence, and in-plane modulus (E_1, E_2, and G_{12}) through Deep Neural Networks. To transform these input data to fit Neural Network training, we conduct data pre-processing to convert weave patterns and material

sequences into matrices and vectors as described next.

Weave Pattern Representation

The yarn placed along the x-axis is called weft, whereas the yarn along the y-axis is called warp. A checkerboard model represents each weave pattern as a matrix with '0' or '1' binary values, where '1' means warp lies below the weft and '0' means warp lies above the weft. A weave pattern and material sequence representations are shown in Figure 5.3, using a bi-material woven composite as the example. This paper considers a woven composite unit cell size of 6-by-6. So, each model is formed by weaving together six warp and six weft yarns, and a 6-by-6 binary value matrix can represent each pattern.

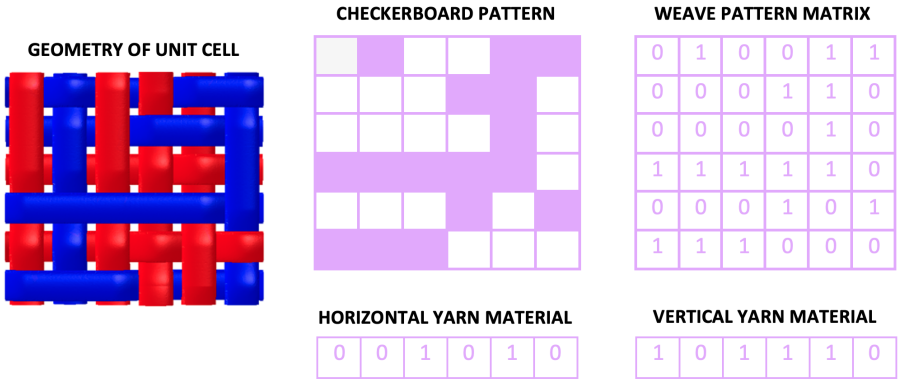

Figure 5.3: Weave pattern and material sequence representation for bi-material woven composite

Weave Material Representation

Since the material sequence for single-material woven composites will not serve as input to the Neural Network, only bi-material woven composites need the proper representation of their material sequences. As mentioned in Section 5.4, the woven composite is formed with six warp and six weft yarns, so the material sequence can be represented as two 6-by-1 binary vectors: the first vector represents warp materials, and the second vector represents weft materials. Here we denote Carbon yarn as material '0' and Kevlar yarn as '1'.

In-plane Modulus from FEA Results

From the outputs of 9000 single-material and 9000 bi-material woven composite models, we obtain the distributions of different in-plane modulus (E_1, E_2, G_{12}). Here we define the Identity Sum (IS) of woven composite to be: $IS = \sum_{i=1}^{n_1} \sum_{j=1}^{n_2} \mathbb{1}_{[W_{ij}=1]}$, where W is the weave pattern matrix, $n_1 = n_2 = 6$ as the pattern matrix is 6-by-6. IS of a model represents the total number of '1' regions within the matrix. Figure 5.4 and Figure 5.5 show the distribution of different in-plane modulus with respect to identity sum for single material and bi-material woven composites. Comparing these two figures, we discover that: (1) single-material and bi-material woven composites have similar ranges for tensile modulus E_1 and E_2; (2) in-plane shear modulus G_{12} distribution for single-material woven composites is

more concentrated compared to bi-material woven composites.

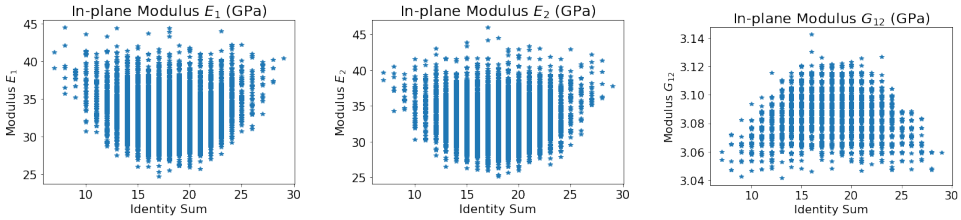

(a) (b) (c)

Figure 5.4: In-plane modulus of single material woven composite

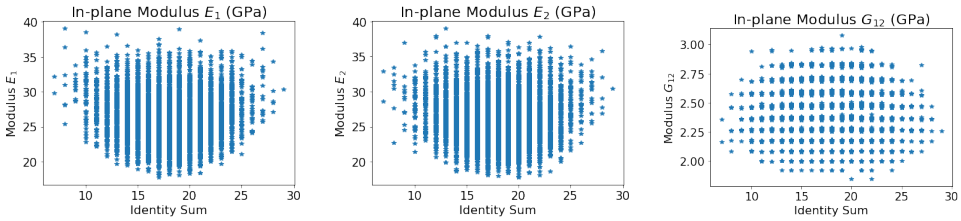

(a) (b) (c)

Figure 5.5: In-plane modulus of bi-material woven composite

Many-To-One Mapping

From Figure 5.4 and Figure 5.5, we can also observe that woven composites with the same IS could have a completely different in-plane modulus. Moreover, our FEA outputs show that different woven composite patterns could have the same in-plane modulus. The two single material woven composite models have the same tensile modulus E_1, although the patterns look entirely different. Such a conclusion can also be validated by

histogram plots counting numbers of models having the same in-plane modulus component E_1, E_2, or G_{12} for both single material and bi-material woven composite models. This many-to-one mapping poses challenges while predicting weave patterns for specified in-plane modulus (BDP problems), which is later addressed within the Deep Neural Network frameworks.

Mechanical Properties of Plain Weave Composites to Other Patterns

Among different patterns typically used in woven composites, plain weave, alternating '0' and '1' in its pattern, has been the most fundamental weave design in different areas including aerospace, fashion, and furnishing. However, this does not mean plain weave has the best mechanical properties. As shown in Figure 5.6, we can see that there are many patterns (28.7% of the 9000 samples) having better in-plane modulus in both E_1, E_2, and G_{12} compared to plain weave (orange dot). Thus it is crucial to explore weave patterns with better mechanical properties than plain weave.

Loss Functions Considered

This paper considers two types of commonly used loss functions: Mean Squared Error (MSE) and Binary Cross-Entropy (BCE). MSE measures how close the predicted value is to the true value. This paper uses MSE

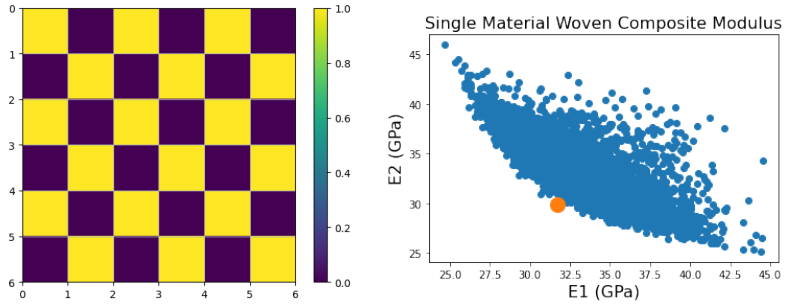

(a) (b)

Figure 5.6: (a) plain weave pattern (b) mechanical properties of plain weave VS all 9000 patterns for single material woven composite (the yellow dot denotes the mechanical properties of plain weave and blue dot denotes the mechanical properties of other weave patterns considered)

for in-plane modulus-related predictions, defined as Equation 5.1.

$$\mathrm{MSE}(y, \tilde{y}) = \frac{1}{3n} \sum_{i=1}^{n} \sum_{j=1}^{3} (y_{ij} - \tilde{y}_{ij})^2 \tag{5.1}$$

Where n is the total sample size, '3' means the size of the in-plane modulus vector, y_{ij} is the predicted value of i^{th} data sample, and j^{th} in-plane modulus. $\tilde{y}_{ij}$ is the corresponding true value. MSE can be widely used for different prediction tasks. However, it could be a wrong choice for binary classification problems as MSE generally assumes data with normal distribution, while binary classification can be viewed as a Bernoulli distribution. Moreover, the MSE function is non-convex for binary classification problems when using activation functions like Sigmoid. Thus we will use BCE defined as Equation 5.2 for predicting binary woven pattern matrix or binary material sequence vector.

$$BCE(y, \tilde{y}) = -\frac{1}{nm} \sum_{i=1}^{n} \sum_{j=1}^{m} \tilde{y}_{ij} log(y_{ij}) + (1 - \tilde{y}_{ij}) log(1 - y_{ij}) \quad (5.2)$$

Similar to the definition of MSE, n is the total sample size, and m is the target size. For example, $m = 36$ when predicting the 6-by-6 weave pattern and $m = 12$ when predicting the 6-by-2 weave material sequence. y_{ij} is the predicted value at j^{th} component in i^{th} model and $\tilde{y_i}$ is the corresponding true value.

5.5 Deep Neural Network Frameworks

This section will show the detailed Deep Neural Network frameworks we propose to solve the FDP and BDP problems. As briefly mentioned in Section 6.1, we utilize DCNN to solve the FDP problem, and we propose our PCNN to solve the BDPa and BDPb problems.

Forward Direction Prediction: Deep Convolutional Neural Network

For the FDP problem, we developed Deep Convolutional Neural Network (DCNN), with the overall framework shown in Figure 5.7. Initially, weave patterns and material sequences are fed into DCNN as inputs. Then for the weave pattern, we will use Convolutional layers with ReLU as the

activation function to extract high-level features from the pattern. At the same time, the material assignment vector will be expanded by fully connected layers. Then extracted features from the weave pattern and material sequence are concatenated into a new feature vector and further used to predict the in-plane modulus through fully connected layers with the ReLU activation function.

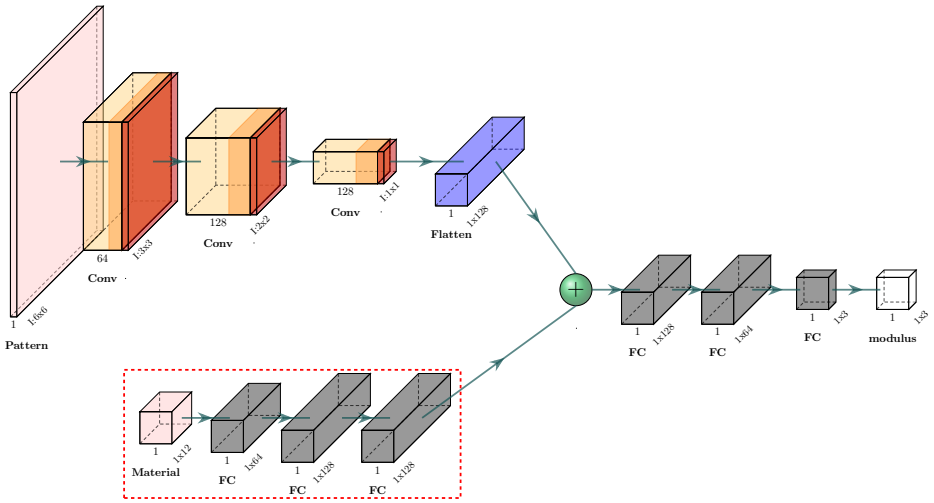

Figure 5.7: Deep Convolutional Neural Network (DCNN) for FDP: pink blocks are the inputs to the Neural Network; orange blocks are convolutional layers with ReLU activation function, and brown blocks are batch-normalization layers following Convolutional layers; the blue block is the Flatten layer that reshapes the input into a vector; gray blocks are Fully Connected layers with ReLU activation function; white blocks are the outputs of the framework. The green ball represents the Concatenation layer. The modules inside the red dashed block are only activated when the material sequence serves as the input for the bi-material woven composite.

Backward Direction Prediction: Physics-Constrained Network Framework

As mentioned in Section 6.1, the BDP problem is decoupled into two problems: BDPa and BDPb. We have shown there exists a many-to-one mapping, which makes BDP problems much more challenging to handle than FDP problems. This paper proposes two PCNNs for BDPa and BDPb, respectively. Although the two frameworks are slightly different due to different input data, both frameworks are developed based on **Physics-constraint** by using trained DCNN from the FDP problem to constrain the prediction.

Predicting weave pattern from in-plane modulus and material sequence (BDPa)

For single-material woven composite, the BDPa problem is to predict the weave pattern directly from the given in-plane modulus. In contrast, the problem is extended for bi-material woven composite to predict woven patterns from given in-plane modulus and material sequence. The whole framework to solve the BDPa problem is shown in Figure 5.8. In-plane modulus and material sequence in pink blocks are the inputs to the framework. The two inputs are expanded through several fully connected layers, concatenated into one vector, and brought into the Deconvolutional layers with LeakyReLU. The deconvolutional layers will expand the feature

vector into its original physical space of 6-by-6. Since each weave pattern is a binary matrix, thus the last Deconvolutional layer uses the Sigmoid activation function. To embed our existing knowledge into the prediction and enhance the prediction accuracy, we add the trained DCNN from Section 5.5 after the predicted woven pattern and further evaluate the prediction's accuracy in terms of in-plane modulus, as shown in the light green block. To improve the prediction accuracy, we control the weights of modulus-related loss three times larger than the weights of pattern-related loss. For the loss function, the pattern-related loss is calculated based on BCE, and the corresponding modulus-related loss is calculated based on MSE.

Predicting weave material sequence from in-plane modulus and pattern (BDPb)

Compared to the BDPa problem, the BDPb problem focuses on predicting weave material sequence from in-plane modulus and pattern. This framework concentrates only on bi-material woven composites as single-material woven composites have a constant material vector, as shown in Figure 5.9. Weave in-plane modulus and pattern serve as inputs to the framework, where the in-plane modulus is passed into several fully connected layers with the ReLU activation function. In contrast, the pattern is passed into several convolutional layers with ReLU activation function followed by batch-normalization. The extracted high-level features from the in-plane

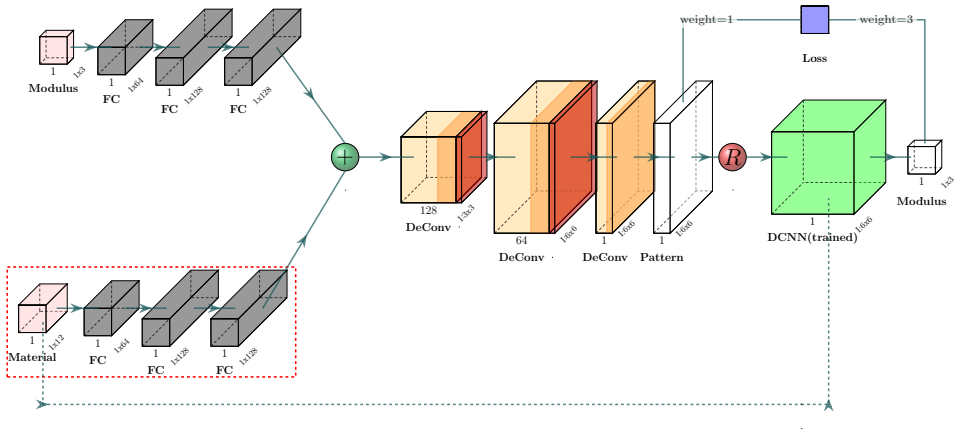

Figure 5.8: Physics-Constraint Neural Network framework for BDPa problem: pink blocks are inputs to the framework; gray blocks are fully connected layers; orange blocks are Deconvolutional layers with LeakyReLU activation function, and brown blocks are batch-normalization layers following the convolutional layers; white blocks are outputs of the framework; the red ball is the rounding layer that round the predicted probability vector into binary values to get the binary material vector; the dark green ball is the concatenation layer that concatenates extracted features from in-plane modulus and material assignment; Light green block refers to the previously trained DCNN framework. The modules inside the red dashed block and the green dashed arrow is only activated when material assignment serves as the bi-material woven composite input.

modulus and pattern are concatenated into a vector and passed into several fully connected layers with the ReLU activation function. Since the material sequence is a binary vector, the last fully connected layer has the sigmoid activation function. Similar to BDPa, to enhance prediction accuracy, we constrain the prediction by adding trained DCNN from Section 5.5 after the prediction layer. Similar to the BDPa problem, the weights of modulus-related loss are also three times larger than the weights of

the material sequence-related loss. For the loss function, the material sequence-related loss is calculated based on BCE, and the corresponding modulus-related loss is calculated based on MSE.

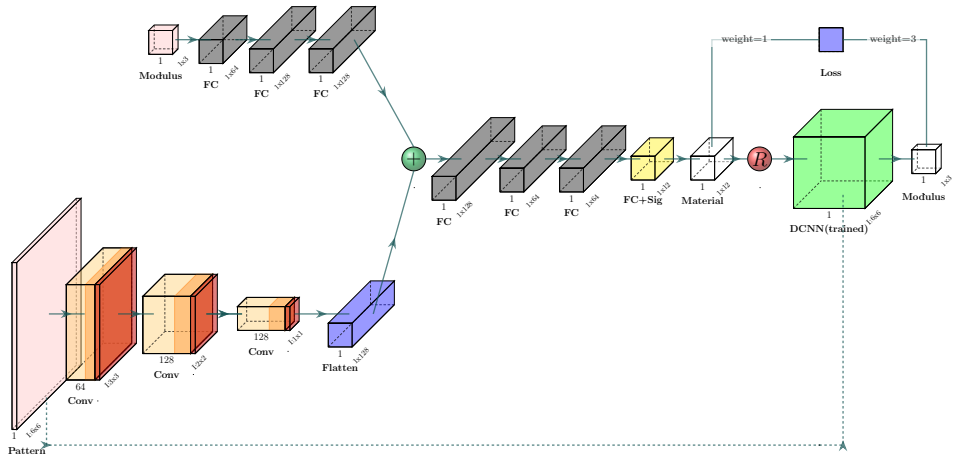

Figure 5.9: Physics-Constraint Neural Network framework for BDPb problem: pick blocks are inputs to the framework; gray blocks are fully connected layers with ReLU as activation function; the yellow block is the fully connected layer with Sigmoid activation function; orange blocks are convolutional layers with ReLU activation function, and brown blocks are batch-normalization layers following the convolutional layers; white blocks are outputs of the framework; the red ball is the rounding layer that round the predicted probability vector into binary values to get the binary material vector; the dark green ball is the concatenation layer that concatenates high-level features from in-plane modulus and pattern; light green block refers to the previously trained DCNN framework.

5.6 Results and Discussion

Overview of Baseline Models Considered

In this research, we use 9000 single-material woven composite models and 9000 bi-material woven models, respectively, to analyze the performance of Machine Learning frameworks. The data are randomly split into a 60% training set, 20% cross-validation set, and 20% testing set. To control the random split method for comparison, we control the random split seed such that different Machine Learning algorithms are evaluated based on the same data set.

To evaluate the Machine Learning framework's performance for the FDP problem, we directly assess the in-plane modulus prediction in terms of mean absolute percentage error (MAPE) defined in Equation 5.3.

$$\text{MAPE} = \frac{1}{n}\sum_{t=1}^{n}\left|\frac{A_t - F_t}{A_t}\right| \tag{5.3}$$

A_t is the actual value, F_t is the predicted value, and n is the total sample size. On the other hand, since BDP problems are more complex than FDP problems, we will evaluate the prediction error based on MAPE and compare our PCNN performance with other popular baseline models. There are three baseline models considered in this paper: (1) Woven-Decoder, which utilizes the Autoencoder structure[6]. Autoencoder framework has been widely used for image-based prediction, like predicting the stress

contours[31, 121, 105]. (2) Woven-GAN, which is developed based on the GAN framework. Here we represent the generator using the Woven-Decoder structure while adding the discriminator after the output to classify the output into a binary value. Such binary values will tell if the generator's result is realistic. The GAN-based framework has been used to predict the checkerboard pattern of bi-material composite or to predict the stress distribution contours of different shapes of cantilever beams under certain loading conditions[19, 67]. (3) Woven-GA, developed based on Genetic Algorithm[147]. The genetic algorithm is a search heuristic from the theory of natural evolution. It generates new generations through crossover and mutations based on a user-defined fitness function by starting from randomly chosen first generations. A genetic algorithm has been used to determine the complex geometry from targeted mechanical properties, like finding the bi-material composite model design with the highest strength[2]. Although BDPa and BDPb problems have different prediction targets, both problems target finding the best pair of patterns and material sequences to match the target modulus. So both BDPa and BDPb are evaluated based on the MAPE between the target in-plane modulus and the predicted architecture's in-plane modulus.

Forward Direction Prediction Results

As mentioned in Section 5.6, the performance of the single-material woven composite is evaluated based on the MAPE values. Since FDP problem

aims to predict the in-plane modulus, the MAPE is calculated based on E_1, E_2, and G_{12}, respectively. We will validate the Neural Network's performance on single-material and bi-material woven composite separately. Table 5.3 shows the prediction results of the single-material and bi-material woven composites. We see that for single material woven composites, our proposed DCNN's prediction error for E_1 and E_2 are below 2%. The prediction error for G_{12} is low as shear modulus does not vary much for single material woven composite, as shown in Figure 5.4. For bi-material woven composites, as each in-plane modulus is more distributed for different models, the prediction error of our proposed DCNN will increase marginally. Our proposed DCNN could achieve prediction error at around 4% for E_1 and E_2 and below 2% for G_{12}. Since woven composite in-plane modulus ranges from around $15GPa \sim 45GPa$, the average error is around $1 \sim 2GPa$. These results indicate that our proposed DCNN effectively represents the relationship between woven architecture and its in-plane modulus.

Table 5.3: FDP prediction error rate

Error Rate	E_1	E_2	G_{12}
Single-Material Woven	1.86%	1.89%	0.25%
Bi-Material Woven	4.08%	3.76%	1.84%

Backward Direction Prediction Results

As discussed, the BDP problem is split into two sub-problems: BDPa and BDPb. To evaluate the performance of our proposed PCNN, we consider the prediction error of BDPa and BDPb problems for single material and bi-material woven composite separately.

Single material woven composite prediction results

For single-material woven composite, we compare our proposed Neural Network framework with three baseline models described in Section 5.6. To compare the prediction between different Machine Learning frameworks, we compare the prediction accuracy and duration, as shown in Table 5.4. From the results, we conclude that:

1. Woven-GA gives the highest prediction accuracy for all models. However, since it is a heuristic searching algorithm, it will take more than one hour for each prediction, and such searching needs to be repeated every time we use it. Also, the performance of heuristic searching largely depends on the data sample. Thus Woven-GA is a costly method and will not be considered.

2. For the rest of the Deep Neural Network-based models, as the models are learned through training-predicting, it takes much less time for each prediction. Compared to Woven-Decoder and Woven-GAN, our PCNN has significantly reduced the prediction error to around

2% for E_1 and E_2. Thus, our PCNN gives the best overall prediction compared to all baseline models.

Table 5.4: BDPa prediction error rate for single material woven composite

Error Rate	E_1	E_2	G_{12}	Prediction Time
Woven-Decoder	7.87%	7.26%	0.33%	«1sec
Woven-GAN	4.34%	5.27%	0.31%	«1sec
Woven-GA	0.05%	0.01%	0.58%	60 mins 18 secs
PCNN	2.38%	1.72%	0.31%	«1sec

Bi-material woven composite prediction results

Since BDP problems for bi-material woven composite consist of three inputs, prediction with Woven-GA will be even more expensive and will not be considered. Table 5.5 shows the prediction results for the BDPa problem, comparing our proposed model and the other two baseline models. Figure 5.10 shows images of the predicted woven patterns for a given in-plane modulus and material sequence. Based on the analysis results, we notice that:

1. Compared to baseline models, PCNN significantly reduces the error rate of E_1 and E_2 predictions from around 10% to 3.6%, and the error rate of G_{12} also decreases to around 1.3%. Thus, PCNN outperforms the baseline models considered.

2. For the predicted pattern, we can find that PCNN gives the closest prediction to the original weave pattern. Furthermore, we show a

detailed quantitative explanation of why PCNN is superior to other models using our proposed GLCM-based feature (in Section 5.8) analysis.

Table 5.5: BDPa prediction error rate for bi-material woven composite

Error Rate	E_1	E_2	G_{12}	Prediction Time
Woven-Decoder	9.31%	9.45%	5.01%	«1sec
Woven-GAN	10.83%	11.71%	10.62%	«1sec
PCNN	3.60%	3.71%	1.34%	«1sec

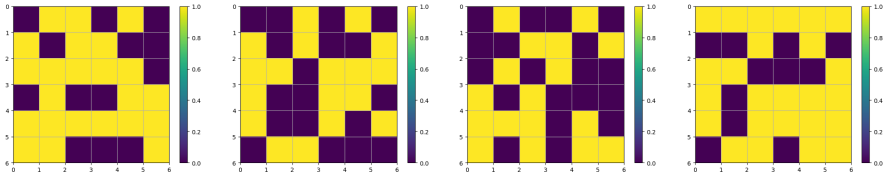

(a) (b) (c) (d)

Figure 5.10: Predicted bi-material weave pattern for BDPa problem: (a) original weave pattern (b) predicted weave pattern from Woven-Decoder (c) predicted weave pattern from Woven-GAN (d) predicted weave pattern from PCNN

We next evaluate the performance of different models for BDPb problems. Table 5.6 shows the prediction result for the BDPb problem, comparing our proposed and baseline models. From these results, we observe that compared to baseline models, Woven-Decoder and Woven-GAN, our proposed PCNN could vastly reduce the prediction error from above 10% to around 5% for all three in-plane moduli. Consequently, we can conclude that for both BDPa and BDPb problems, our proposed PCNN can significantly improve the prediction accuracy for all three in-plane moduli.

Table 5.6: BDPb prediction error rate for bi-material woven composite

Error Rate	E_1	E_2	G_{12}	Prediction Time
Woven-Decoder	11.74%	11.73%	11.50%	«1sec
Woven-GAN	15.28%	12.35%	26.99%	«1sec
PCNN	5.53%	5.65%	4.10%	«1sec

Weave pattern modification by bound relaxation of modulus (for manufacturing purpose)

When predicting the weave pattern in the BDPa problem, we do not add constraints to the predicted pattern. However, during manufacturing, it is usually challenging to weave patterns with continuous yarns or fiber bundles running along the warp and weft directions without crossing yarns in perpendicular directions. Solving this issue requires using pre-preg tapes made from "pre-impregnated" fibers and a partially cured polymer matrix. Alternatively, stitching of fibers is needed. Since this process can be time-consuming and expensive, finding weave patterns that do not have continuous fibers or yarns is essential. To solve this problem, we propose to find weave patterns by modifying the target modulus within specific ranges, which we call as **Modulus Bound Relaxation**.
The expression of Modulus Bound Relaxation can be represented as Equation 5.4.

$$M_{new} = M_{old} + R \times B \tag{5.4}$$

Where M_{old} is the target modulus vector containing E_1, E_2, G_{12}, and M_{new}

is the updated new modulus vector. $R \in [-1, 1]^{d=3}$ is a 3-by-1 vector, with each component randomly generated between -1 and 1. B is a range of scaling factor of R, the upper and lower bound of B can be specified by the user. $R \times B$ determines the maximum relaxation we want for the target modulus vector. We linearly increase the value of B from its lower bound to its upper bound to increase the relaxation until we find a weave pattern without continuous yarn. With this method, we can find a surrogate weave pattern with a modulus vector slightly different than our target, but with no continuous yarn issue.

5.7 PCNN Performance Under Small Dataset

This section tests how PCNN performs when the dataset is small. Specifically, we analyze the performance of PCNN when we select 3000 and 6000 bi-material woven composite samples each from the 9000 dataset. Table 5.7 and Table 5.8 show the prediction error for 3000 and 6000 samples. We observe consistent results compared to the previous analysis using 9000 samples from the results. Thus we conclude that for both BDPa and BDPb problems, PCNN provides better and more stable prediction accuracy than the two baseline models.

Furthermore, Table 5.8 shows the prediction error of BDPa and BDPb problems under the 6000 sample. From the result, we can validate that for both BDPa and BDPb problems, PCNN has much better prediction

Table 5.7: Prediction error rate with 3000 bi-material woven composite samples

	Error Rate	E_1	E_2	G_{12}	Prediction Time
BDPa Problem	Woven-Decoder	10.61%	11.97%	10.30%	<<1sec
	Woven-GAN	8.67%	6.27%	6.87%	<<1sec
	PCNN	4.23%	4.28%	3.63%	<<1sec
BDPb Problem	Woven-Decoder	8.73%	8.84%	10.93%	<<1sec
	Woven-GAN	11.53%	12.55%	11.65%	<<1sec
	PCNN	4.69%	3.70%	1.53%	<<1sec

accuracy compared to the two baseline models.

Table 5.8: Prediction error rate with 6000 bi-material woven composite samples

	Error Rate	E_1	E_2	G_{12}	Prediction Time
BDPa Problem	Woven-Decoder	11.61%	12.20%	12.33%	<<1sec
	Woven-GAN	6.48%	6.91%	6.14%	<<1sec
	PCNN	3.81%	3.93%	3.18%	<<1sec
BDPb Problem	Woven-Decoder	9.24%	9.43%	10.99%	<<1sec
	Woven-GAN	12.20%	11.56%	10.24%	<<1sec
	PCNN	4.10%	4.20%	1.49%	<<1sec

5.8 Feature-based Statistical Optimization

In the previous sections, we proposed DCNN and PCNN to establish the bridge between woven architectures and the corresponding modulus. Our proposed Deep Learning frameworks deliver better predictions for FDP, BDPa, and BDPb problems than baseline models. However, the high-level features extracted by PCNN are challenging to understand and be used for other tasks like optimization. Thus, we want to know what physically or statistically meaningful features control the woven composite in-plane

modulus, and how we can use these features to optimize the woven composite. To that end, we conduct the GLCM-based feature analysis.

Statistical Features from Weave Pattern

Since weave patterns are represented by a checkerboard model, we considered this as a type of texture. Texture features describe the spatial distribution of pixels (cells) that reflect an object's roughness, smoothness, granularity, and randomness. Texture can be used to segment images into regions of interest and classify those regions into regular texture and quasi-regular texture. Regular texture's element follows a specific pattern, whereas quasi-regular texture's element has an arbitrary shape and is distributed based on intensity. Standard texture feature extraction methods include statistical, structural, and spectral methods. This paper utilizes the statistical method and constructs the Gray Level Co-occurrence Matrices (GLCM). GLCM elements are defined in Equation 5.5.

$$C_{\Delta x,\Delta y}(i,j) = \sum_{x=1}^{n}\sum_{y=1}^{m} \mathbb{1}_{[I(x,y)=i,I(x+\Delta x,y+\Delta y)=j]} \tag{5.5}$$

where, I is the grey-level image, i and j are pixel values. n, m is the size of image, (x, y) is the starting position, and $(\Delta x, \Delta y)$ represent the offset from starting position. As our checkerboard models are binary matrices in this paper, the GLCM will be a 2-by-2 matrix, where we consider transitions of $0 \to 0$, $0 \to 1$, $1 \to 0$, and $1 \to 1$. Further, we consider four

different directions (horizontal, vertical, and two diagonal directions) during GLCM calculation. The texture features considered are contrast, correlation, energy, and homogeneity. Thus, for each woven composite pattern matrix, we will extract $4 \times 4 = 16$ features. We can achieve several excellent properties by extracting statistical features from 2-by-2 GLCM in the form $\begin{bmatrix} a & b \\ c & d \end{bmatrix}$, leading to the following propositions:

Proposition Weave pattern GLCM statistical features (Contrast, Correlation, Energy, Homogeneity) correspond to a unique 2-by-2 GLCM.

Proposition Weave pattern GLCM's Energy (with the help of several other statistical features) tells the relative relationship between different pattern transitions ($0 \to 0$, $0 \to 1$, $1 \to 0$, and $1 \to 1$) in the physical space.

Proposition Weave pattern GLCM's Contrast and Homogeneity tell the frequencies of homogeneous transition ($0 \to 0, 1 \to 1$) and in-homogeneous transition ($0 \to 1, 1 \to 0$).

Statistical Features from Weave Material Sequence

Statistical features from woven composite material are only considered for bi-material woven, as the material sequence for single material is a uniform

constant vector. We split the material vector into the vector for the weft and the vector for the warp. First, we extract statistical features for each material vector, including mean, median, and standard deviation from the vector. For each material vector of woven composite, we extract six features. Specifically, as material vectors can be constant, we do not include skewness and kurtosis in this study. Then, to account for the sequence information, we propose another statistical parameter called Vector Energy (VE): for any vector V, the vector energy is defined as $VE = \sum_{i=1}^{L} i * V(i)$. Here L denotes the length of the vector, and $V(i)$ is the value of the i-th component in V.

Regression Analysis of Extracted Features

To understand whether each statistical feature is positively or negatively correlated with in-plane modulus, we use regression analysis to determine the weights of each feature. Specifically, we consider two different cases: (1) how each feature is correlated with the label of the composite model. We group the woven composite models into two groups: one group with an overall better modulus is labeled as '1,' and the other group is labeled as '0'; (2) how each feature is correlated with the value of individual in-plane modulus.

Regression analysis on the overall modulus of model

To understand what features contribute to woven composite's better overall modulus ($E_{all} = E_1 + E_2 + G_{12}$), we utilize the Ridge regression to predict the overall modulus directly from the target statistical features. The regression model is defined as Equation 5.6.

$$\min_{\mathbf{w},\lambda} ||\mathbf{y} - X\mathbf{w}||^2 + \lambda||\mathbf{w}||^2 \tag{5.6}$$

where X is the matrix formed by feature vectors. y is vector containing E_{all} values. Similarly, values in vector $\mathbf{w}$ tell us how each statistical feature is correlated to the woven composite model's E_{all} values.

Weave pattern feature analysis

We first fix the weave material sequence and analyze how the weave pattern features are correlated with the overall composite modulus E_{all}. From the regression analysis results, we observe that the two regression models, one each for single and bi-material, have weights with the same signs, as shown in Table 5.9. From the results, we conclude that: contrast and correlation are negatively correlated with the woven composite's overall modulus, while energy and homogeneity are positively correlated. Furthermore, we prove that the GLCM features can be used to optimize weave patterns and guide the woven composite design by a case study.

Table 5.9: Sign of weights for weave pattern features

	Contrast	Correlation	Energy	Homogeneity	Contrast	Correlation	Energy	Homogeneity
	GLCM 1				GLCM 2			
Single Material	-	-	+	+	-	-	+	+
Bi-Material	-	-	+	+	-	-	+	+
	GLCM 3				GLCM 4			
Single Material	-	-	+	+	-	-	+	+
Bi-Material	-	-	+	+	-	-	+	+

Weave material feature analysis

We further consider how weave material features correlate with its overall modulus E_{all} by fixing the weave pattern. Here we consider two fixed weave patterns. Each weave pattern is combined with 500 randomly distributed binary material vectors for regression analysis. Similarly, we consider the two regression models proposed that correspond to the two fixed weave patterns.

The regression analysis results show that only the material sequence's mean value controls the weave material's modulus. This implies that the sequence of the material vector is much less critical than the number of different materials on the property. From our regression analysis, we show that: for the two materials, Carbon (labeled as '0') and Kevlar (labeled as '1'): (1) in vertical yarns, we want to increase the ratio between material '1' and material '0' and (2) in horizontal yarns, we want to decrease the ratio between material '1' and material '0'. We can optimize the overall modulus for a given weave pattern by changing the material sequence vector.

Regression analysis conclusions

From the regression analysis of the weave pattern and material sequence vector, we can conclude that:

1. For fixed weave material sequence, the relationship between weave pattern and overall in-plane modulus can be described using GLCM features. The regression analysis shows that energy and homogeneity positively correlate with the overall modulus, while contrast and correlation negatively correlate with the overall modulus. Such a conclusion applies to all checkerboard-type models and can be used to optimize the weave pattern.

2. For a fixed weave pattern, the relationship between weave material sequence and overall in-plane modulus can be described by the mean of the material sequence vector in the physical space. The regression analysis shows that for the two materials considered in this paper, we want to increase the ratio between material '1' to material '0' in vertical yarns and decrease the ratio in horizontal yarns. Such a conclusion is found based on the two specific materials considered.

5.9 Discover Optimal Woven Composite Architecture at Initial Design Stage

We have shown that PCNN can predict weave patterns or material sequences with high accuracy, and feature-based optimization could enhance the overall modulus of woven composite models. The proposed optimization strategy can be combined with PCNN to determine the optimal woven composite architecture even at the initial design stage. For example, to design a woven composite model, we assume there are two materials to choose from for each yarn. We can use any weave pattern to find the woven composite with the highest overall modulus. To find out the optimal design, we can follow the steps below:

1. Determine the optimal material sequence through the feature-based optimization strategy, then follow the same procedure as shown in Section 5.8 and Section 5.8.

2. Pick the maximum in-plane modulus (E_1, E_2, G_{12}) within a reasonable range, choose the material sequence vector determined in Step 1, then use PCNN to predict the weave pattern.

3. After obtaining the weave pattern, further utilize a feature-based optimization strategy to optimize the weave pattern to achieve the optimal woven composite designs.

5.10 Conclusions

This paper first focuses on woven composite and establishes the bridge between woven architectures (patterns and material sequences) to the corresponding in-plane modulus through Deep Neural Networks. We classify the prediction into the typical design process (FDP) and inverse design process (BDPa and BDPb). The FDP problem is solved by a Deep Convolutional Neural Network (DCNN). For the much more complex BDP problems, we proposed the Physics-Constraint Neural Network (PCNN) to predict from in-plane modulus to woven composite architecture. We have shown that our proposed DCNN delivers relatively accurate predictions. More importantly, PCNN can make sound predictions for BDP problems and vastly outperforms the baseline models we considered. After that, we further proposed a feature-based optimization strategy to find optimal woven composite architectures. We propose GLCM feature-based optimization strategy for weave patterns and statistical feature-based optimization for weave material sequences. We further prove that the feature-based optimization strategy can accurately and conveniently optimize the woven composite architecture. Finally, we can find the optimal woven composite architecture by combining PCNN with a feature-based optimization strategy.

Key contributions to this paper are:

1. To our knowledge, this is the first attempt toward a bi-direction

design process for woven fabrics and textiles with Deep Neural Networks. That is, predicting mechanical properties from weave architectures (pattern and material sequence) and vice-versa. We primarily focused on woven composites in this paper.

2. To solve the complex backward prediction (BDP) problems, we proposed our Physics-Constraint Neural Network (PCNN) to bridge between the woven composite's modulus and architecture. We have shown that our proposed Neural Network vastly increases the prediction accuracy compared to several popular baseline models.

3. We further proposed feature-based optimization to optimize the woven composite architecture. We proposed Gray Level Co-occurrence Matrix-based optimization strategy for weave pattern optimization and a statistical feature-based optimization strategy for weave material sequence. The feature-based optimization strategy can be combined with PCNN to determine the optimal woven composite architecture even at the initial design stage.

6 ROLE OF MATERIAL DIRECTIONALITY ON THE MECHANICAL RESPONSE OF MIURA-ORI COMPOSITE STRUCTURES

Haotian Feng, Guanjin Yan, Pavana Prabhakar, Role of material directionality on the mechanical response of Miura-Ori composite structures, Composite Structures, Volume 306, 2023.

Abstract

This paper aims to understand the role of directional material properties on the mechanical responses of origami structures. We consider the Miura-Ori structures our target model due to their collapsibility and negative Poisson's ratio (NPR) effects, which are widely used in shock absorbers, disaster shelters, aerospace applications, etc. Traditional Miura-Ori structures are made of isotropic materials (Aluminum, Acrylic), whose mechanical properties like stiffness and NPR are well understood. However, how these responses are affected by directional materials, like Carbon Fiber Reinforced Polymer (CFRP) composites, needs more in-depth understanding. To that end, we study how fiber directions and arrangements in CFRP composites and Miura-Ori's geometric parameters control the stiffness and NPR of such structures. Through finite element analysis, we show

that Miura-Ori structures made of CFRP composites can achieve higher stiffness and Poisson's ratio values than those made of an isotropic material like Aluminum. Then through regression analysis, we establish the relationship between different geometric parameters and the corresponding mechanical responses, which is further utilized to discover the Miura-Ori structure's optimal shape. We also show that the shear modulus is a dominant parameter that controls the mechanical responses mentioned above among the individual composite material properties within the Miura-Ori structure. We demonstrate that we can optimize the Miura-Ori structure by finding geometric and material parameters that result in combined stiffest and most compressible structures. We anticipate our research to be a starting point for designing and optimizing more sophisticated origami structures with composite materials incorporated.

6.1 Introduction

Deployable structures can change their shape such that their size can be significantly altered. This is often achieved by the folding and unfolding process, which provides deployable structures the flexibility to expand or contract based on different geometrical and material properties. Deployable structures are mostly used for easy storage and transport and are deployed into their operational configuration when required[108]. They find applications in astrophysics missions[81], vehicle fairings[114],

and spacecrafts[127] among others. These structures often require to be lightweight, have high stiffness, and occupy less storage space. Among different ways of achieving deployable structures, origami structures, the ancient art of folding paper, have been extended to engineering applications to design deployable structures.

Miura fold[118], a classical origami pattern, is a method of folding a flat surface such as a sheet of paper into a smaller effective area. Miura-Ori patterns are composed of identical unit cells of mountain and valley folds with four-coordinated ridges. Different fold patterns could lead to interesting mechanical responses and material properties, like higher stiffness and contraction ability known as negative Poisson's ratio (NPR)[82]. Materials such as foams and microporous polymers with NPR are often referred to as auxetics[15]. They often possess the high energy-absorbing capability and fracture resistance. Miura-Ori patterns with such unique characteristics have been used in applications at both micro and macro scales, like in solar panels[63], surgical stents[70], and self-deployable robots[96]. The origami or Miura-Ori patterns have also been widely used as impact mitigating systems[153] and impact protectors like the crush box[157] and robotic rotorcraft protectors[117]. Besides these structural applications, recent researchers also utilized the unique shape of Miura-Ori in other fields, including stretchable circuit bands[86], sound absorption[140], aerodynamic drag reduction[159], and stiffness vibration isolators[154]. Past research has focused on exploring the mechanical responses of origami

structures. Fisher et al.[37] explored the stress-strain relationship (through compression and transverse shear tests) of sandwich structures with different types of cores made by folding sheet materials into three-dimensional zigzag patterns. Heimbs et al.[53] investigated both experimental and numerical methods for analyzing folded cores called Ventable Shear Core (VeSCo) in sandwich composites under dynamic compression loading. With regard to Miura-Ori structures, Zhou et al.[166] presented a parametric study on the mechanical responses of a variety of Miura-Ori-based folded core models by virtual testing under quasi-static compression, shear, and bending using the Finite Element Analysis (FEA). Wei et al.[142] characterized the geometry and analyzed the effective elastic response of a simple periodically folded Miura-Ori structure by establishing mathematical expressions for stiffness and Poisson's ratio concerning geometric parameters. Liu et al.[88] performed FEA based study to analyze the deformations of the Miura-Ori patterned sheet and validated the simulation result through tests under the same loading. Moradweysi et al.[97] analyzed the effective properties of Miura-Ori structures with small or significantly large thicknesses. The authors focused on analyzing unit cells of the Miura-Ori pattern under static periodic boundary conditions. They discovered that when the thickness is small, the rigid rotation of facets becomes dominant, and as the thickness value increases, the strict rotation mechanism tends to diminish. Gao et al.[38]proposed a novel design of Miura-Ori honeycomb structure, whose core layer at the mid-

dle is sandwiched by two secondary flange layers at the top and bottom. The model has connectivity with an open channel within the material and a self-locking feature under loading. Zhang et al.[162] proposed a thick panel Miura-Ori structure that uses bistable anti-symmetric carbon fiber reinforced polymer (CFRP) shells to connect and drive the whole structure. The authors proposed an energy-based theoretical model and showed that the proposed structure has superior stability, high reliability, and fast response speed. Besides these works, other researchers also look into the potentialities to design and optimize deployable structures with Machine Learning and Statistical Learning[163, 167].

These previous studies on folded structures, especially Miura-Ori structures, have focused on investigating the relationship between geometric parameters and mechanical responses for isotropic materials. However, few researchers have focused on combining composite materials and origami patterns to harness the benefits of directional properties and high stiffness/strength-to-weight ratios, like in fiber-reinforced composites. Domber et al.[25] studied the dimensional repeatability of elastically folded composite hinges for deployed spacecraft optics. They investigated a new type of folded composite hinge for precision deployable spacecraft structures and showed that viscoelastic recovery is independent of stow duration. Saito et al.[116] focused on manufacturing composite honeycomb cores based on origami patterns. They illustrated a new strategy to construct arbitrary cross-section composite honeycombs by applying 3D

kirigami patterns into honeycombs and generalizing the honeycomb model by corresponding kirigami parameters. The authors further fabricated the kirigami honeycombs using the proposed folding line diagrams (FLD) design method. Cui et al.[24] investigated origami pattern guided morphing for composite sheets, where they demonstrated a new approach to fold origami/kirigami structures based on Gaussian curvature change induced by nonuniform lateral shrinkage and embedded rigid origami skeleton in polymer sheets to create novel 3D structures. Kwon et al.[79] analyzed origami-inspired shape memory dual-matrix composite structures. They developed an analytical model to analyze 3D morphing structures and fabricated woven fabrics based on shape memory polymers. They further showed that morphing structures could be highly flexible depending on temperature based on tensile tests.

However, research on how structures made of composite materials with directional properties and geometric parameters of origami patterns influence their mechanical responses is lacking. Thus, in the current paper, we focus on exploring how the directionality of fiber-reinforced polymer composites and geometric parameters of the patterns impact the optimal shape of the Miura-Ori structure. To evaluate this, we consider mechanical properties - compressive stiffness and Poisson's ratio. We then determine the directional Miura-Ori structure that outperforms the isotropic Miura-Ori structure.

In this paper, we focus on the following three objectives:

1. Understand how fiber directionality influences the mechanical responses of Miura-Ori structures.

   For the directional material, we consider the transversely isotropic material (Carbon Fiber Reinforced Polymer (CFRP) composites[59]). We vary the geometry and fiber arrangements within the Miura-Ori cells. We then perform compression analysis using the finite element method. We use Miura-Ori cells with isotropic material, Aluminium, as a baseline model to compare against the mechanical properties of different CFRP composite arrangements. We consider CFRP composites due to their inherent transversely isotropic material behavior. CFRP composites are extremely strong and lightweight compared to traditional isotropic materials and are widely used in engineering, including aerospace, automotive, marine, and construction[31].

2. Explore how geometric parameters affect Miura-Ori's corresponding mechanical response and determine the optimal design

   We fix the isotropic and directional materials and change the geometric parameters to find the optimal design. Specifically, we perform a regression analysis to determine the relationship between geometric parameters and the corresponding mechanical responses. We then use this relationship to determine the optimal geometric configuration subject to different optimal requirements.

3. Establish how individual material properties affect the overall me-

chanical responses of Miura-Ori structures

After the geometric analysis of Miura-Ori, we vary individual material properties of composite materials to elucidate what properties have a dominant effect on the mechanical responses, like stiffness and NPR. We propose using woven composites for potentially altering a few specific material properties due to the flexibility of selecting different yarn materials and weaving patterns[158, 99, 35].

Although the results shown in this paper are for the Miura-Ori structure, the same methodologies in this paper can be extended to the analysis and optimization of other types of origami structures.

6.2 Miura-Ori Model Setup

Model Geometry and Directionality

Miura-Ori pattern consists of a 2D array of repeating units with four identical parallelograms in each unit, as shown in Figure 6.1(a). l is the crease length, α is the angle between the sides of each parallelogram at the left-top corner, and β is the angle between planes S1 and S2. θ is the angle between planes S1 and S3. Based on the paper by Wei et al.[142], the angles α, β, and θ are correlated with each other and can be expressed

with the Equation 6.1.

$$\begin{aligned} \beta &= 2\sin^{-1}[\zeta \sin(\theta/2)] \\ l &= 2 l_1 \zeta \\ w &= 2 l_2 \xi \\ h &= l_1 \zeta \tan\alpha \cos(\theta/2) \end{aligned} \tag{6.1}$$

where the dimensionless terms width and height can be expressed as: $\xi = \sin\alpha \sin(\theta/2)$ and $\zeta = \cos\alpha\,(1-\xi^2)^{-1/2}$. Thus in this paper, only α and β as considered as independent geometric parameters. We consider α values can vary between $0°$ and $90°$, while β values can vary between $0°$ and $180°$.

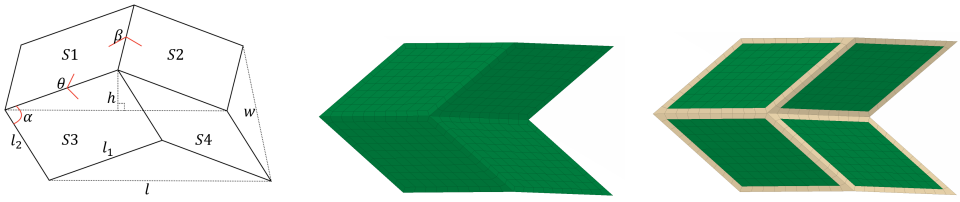

(a) (b) (c)

Figure 6.1: (a) Geometric parameters for a single unit cell of the Miura-Ori pattern (b) Miura-Ori single unit cell without hinge (c) Miura-Ori single unit cell with hinge region (yellow color)

For directional Miura-Ori structures, three different fiber arrangements within each Miura-Ori unit are considered, as shown in Figure 6.2. Fibers are either arranged along the X1 axis or X3 axis in all four parallelograms of a single unit (Figure 6.2(a)), which can be achieved by using unidi-

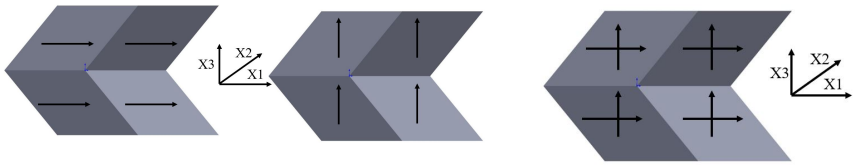

(a) (b)

Figure 6.2: (a) Miura-Ori pattern with fiber direction along X1 axis - Case 1 and along X3 axis - Case 2 (b) Miura-Ori pattern with woven fiber reinforcements (fibers interlaced in two orthogonal directions - X1 and X3

rectional fiber reinforced composites. The third case is where fibers are arranged in both X1 and X3 axes within each parallelogram (Figure 6.2(b)), which can be achieved by a bi-directional woven fiber composite. Woven fiber composites are formed by weaving or interlacing warp and weft fiber bundles. Possible weaving architectures and choices of materials for warp/weft fiber bundles present a large range of possibilities that could influence in-plane mechanical responses, primarily in in-plane normal and shear directions. Due to the transversely isotropic behavior of fiber-reinforced composites in addition to the geometry of Miura-Ori units, the global mechanical properties of these structures are different in different directions. To study how these mechanical responses can be tuned, we study the compressive deformations in two principal directions - X1 and X3.

Miura-Ori patterns we have considered in this paper have dimensions of 10 mm x 10 mm for every parallelogram. These dimensions are based on

that considered in Liu et al.[88], although these dimensions can be scaled. Each pattern consists of two regions: the cell region and the hinge region. We define two different types of arrangements: (1) both cell region and hinge region are made of the same stiff material like CFRP composites (we call it **rigid Miura-Ori**) - Figure 6.1(b); (2) cell region is made of a stiff material while the hinge region is made of soft material like silicone (we call it **flexible Miura-Ori**) - Figure 6.1(c). We compare the global mechanical responses of these two different types of Miura-Ori structures and explore how geometric and material parameters influence their mechanical responses. In this study, we set the width of the hinge region in the flexible Miura-Ori models to be 0.5 mm. For modeling purposes, we assume a perfectly joined connection between the hinge regions and carbon fiber-reinforced laminates in our geometry. From a manufacturing point of view, we can introduce flexible hinges by different methods. These methods are: (1) For a structure with continuous hinges, we can use a dual matrix hand layup approach to arrange the laminate parallelograms with fiber directions along specified directions and locations based on the design. This can be done by placing a stencil on a dry fabric's hinge area and covering it with flexible resin, removing the stencil, and adding epoxy matrix everywhere else. (2) For a structure with discontinuous hinges, we can use mechanical hinges bonded/fastened to the stiff laminates. For rigid hinges, we can perform compression molding of polymer-infused carbon-reinforced fabric between molds of the desired design.

Material Properties

Transversely isotropic linear elastic properties of unidirectional CFRP composites used in the Miura-Ori models shown in Figure 6.2(a) are given in Table 6.1[54, 110]. For those with bi-directional materials shown in Figure 6.2(b), we use the properties of woven fiber reinforced composites given in Table 6.1[17]. In both cases, we consider homogenized laminate in this paper with effective properties given in Table 6.1. We do not explicitly model individual layers or fibers in this paper. To compare the response of our target Miura-Ori models which are made of CFRP or woven fiber composites, we consider a baseline model entirely made of an isotropic material - Aluminum. The Young's modulus and Poisson's ratio of Aluminum are $E = 70GPa$ and $\mu = 0.33$. For flexible Miura-Ori models with soft hinges, we use Young's modulus $E = 3.1$ GPa and Poisson's ratio $\mu = 0.48$[115]. An example of a single Miura-Ori unit with silicone resin in the hinge region is shown in Figure 6.1(c).

Table 6.1: Input material properties of Carbon Fiber Reinforced Polymer (CFRP) and Woven Composites

Material Property	E_1	E_2	E_3	μ_{12}	μ_{23}	μ_{13}	G_{12}	G_{23}	G_{13}
CFRP Composite	155 GPa	12.1 GPa	12.1 GPa	0.248	0.458	0.248	4.4 GPa	3.2 GPa	4.4 GPa
Woven Composite	85 GPa	85 GPa	12.1 GPa	0.3	0.3	0.3	5 GPa	0.765 GPa	0.765 GPa

6.3 Computational Analysis

This section describes the computational modeling of Miura-Ori structures under compression loading. We evaluate their response under external in-plane loading in the two in-plane principal directions.

Model Parameters and Boundary Conditions

For compression analysis, we consider compressive load acting along each of the two orthogonal in-plane directions: X1 and X3. We determine two global mechanical responses of the Miura-Ori models: Poisson's ratio and in-plane stiffness. We select combinations of $\alpha = (15^\circ\ 30^\circ\ 45^\circ\ 60^\circ\ 75^\circ)$ and $\beta = (30^\circ\ 60^\circ\ 90^\circ\ 120^\circ\ 150^\circ)$, and perform 25 simulations for each loading case. Miura-Ori patterns with combinations of extreme angles for α and β - $(15^\circ,30^\circ)$, $(15^\circ,150^\circ)$, $(75^\circ,30^\circ)$, and $(75^\circ,150^\circ)$, are shown in Figure 6.3. Figure 6.4(a) shows a Miura-Ori pattern with external boundaries defined as Γ_1, Γ_2, Γ_3, and Γ_4 for the top, right, bottom, and left edges. The boundary condition on each boundary is described below in terms of u (X1) and v (X3) displacements. Boundary conditions for compressive loading cases along X1 and X3 directions are described in Equation 6.2 and Equation 6.3, respectively. Here, d is the externally applied displacement set to 20% of the domain length along the loading direction. This is to achieve enough transverse displacement to calculate the negative Poisson's ratio, although other displacement percentages can be chosen.

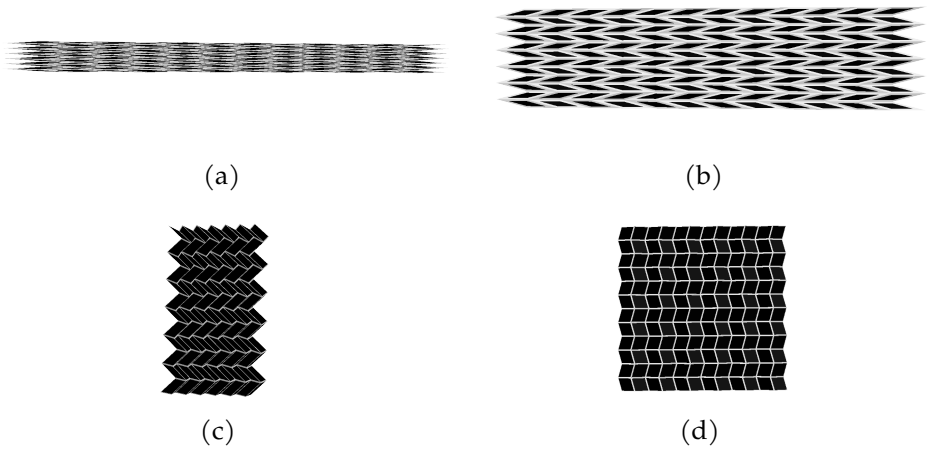

Figure 6.3: Miura-Ori patterns with extreme values of α and β: (a) $\alpha = 15^\circ, \beta = 30^\circ$ (b) $\alpha = 15^\circ, \beta = 150^\circ$ (c) $\alpha = 75^\circ, \beta = 30^\circ$ (d) $\alpha = 75^\circ, \beta = 150^\circ$ (These figures showcase the shape of Miura-Ori patterns, and do not reflect the actual size)

$$\begin{aligned} v &= \text{constant} \quad \text{on} \quad \Gamma_1 \\ u &= -d \quad \text{on} \quad \Gamma_2 \\ v &= 0 \quad \text{on} \quad \Gamma_3 \\ u &= 0 \quad \text{on} \quad \Gamma_4 \end{aligned} \tag{6.2}$$

$$
\begin{aligned}
v &= -d \quad \text{on} \quad \Gamma_1 \\
u &= \text{constant} \quad \text{on} \quad \Gamma_2 \\
v &= 0 \quad \text{on} \quad \Gamma_3 \\
u &= 0 \quad \text{on} \quad \Gamma_4
\end{aligned}
\tag{6.3}
$$

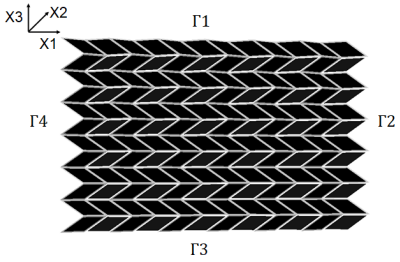

Figure 6.4: Boundary definitions on Miura-Ori model for in-plane compression

Finite Element Modeling and Analysis

Each model is subjected to a compressive displacement along either the vertical or the horizontal direction. Compressive stiffness is represented by a Compressive Stiffness Indicator (CSI) defined in Equation 6.4 as the initial slope of the force-displacement graph.

$$\text{Compressive Stiffness Indicator, } K_C = \frac{\text{Reaction Force at the Loading Edge}}{\text{Loading Edge Displacement}} \tag{6.4}$$

Poisson's ratio is calculated using Equation 6.5.

$$\nu = -\frac{\epsilon_{\text{transverse}}}{\epsilon_{\text{axial}}} \tag{6.5}$$

where, $\epsilon_{\text{transverse}} = \frac{\Delta L_{\text{transverse}}}{L_{\text{transverse}}}$ and $\epsilon_{\text{axial}} = \frac{\Delta L_{\text{axial}}}{L_{\text{axial}}}$. L_{axial} and $L_{\text{transverse}}$ refer to the original length along the loading and the in-plane transverse directions. Correspondingly, ΔL_{axial} and $\Delta L_{transverse}$ are the length changes along these directions.

To determine the physical properties described above, a Miura-Ori model is first discretized by meshing with 3-node (S3) and 4-node (S4R) shell elements in a finite element software - ABAQUS[126]. We perform a mesh convergence analysis to determine the appropriate mesh size. The connections between the hinge and CFRP regions are modeled as a rigid connection in our finite element model. After assigning the corresponding material properties, boundary conditions, and loads, this meshed structure is passed into a numerical analysis solver to determine the nodal displacements and related strain and stress fields.

6.4 Regression Analysis for Optimizing Miura-Ori Structures

To determine optimal geometry that can possess both high stiffness and negative Poisson's ratio, we perform multiple regression analysis to establish a relationship between geometric parameters (α, β) and target effective properties. Multiple regression is a statistical method to determine the relationship between a single dependent variable and several independent variables. A regression coefficient β is calculated by minimizing the sum of squared errors $\sum_i (Y_i - f(X_i, \beta))^2$, given the estimation function f and $\{X_i, Y_i\}$ for each i-th sample from a dataset. In this paper, the independent variables are the geometric parameters (α and β), and the dependent variable is an effective target property (stiffness K or Poisson's ratio ν). Wei et al.[142] established a relationship between effective stiffness K and Poisson's ratio ν as a function of geometric angles in the trigonometric form. They utilized the Miura-Ori structure as our analysis but assumed a uniform material, the same edge length, and spring constant to derive these simplified analytical functions. However, in our analysis, as we consider the entire geometry with complex boundary conditions and directional materials, it is much more challenging to express K and ν in simplified analytical functions. However, K and ν are still functions related to α and β. As trigonometric functions can be represented with Taylor's series expansion, so we have the expression: $(K, \nu) \sim$

$C + F_{0.5}(\alpha^{0.5}, \beta^{0.5}) + F_1(\alpha, \beta) + F_{1.5}(\alpha^{1.5}, \beta^{1.5}) + F_2(\alpha^2, \beta^2) + ... + O(\alpha^n, \beta^n)$. Here, F_i represents the function consisting of the i-th power of geometric parameters including cross-terms, and C is the intercept term. Thus, we can use a linear regression model consisting of different orders of α and β to approximate K and ν.

Grid map interpolation

In order to fit a regression model with higher-order terms, we first expand our data from FEA results using interpolation. We interpolate the original 5-by-5 contour (as discussed in Section 6.3) onto a map with a denser 13-by-13 grid for additional intermediate values of α and β. Figure 6.5 shows the original 5-by-5 FEA grid in blue and the target 13-by-13 denser grid in red. In order to interpolate the original FEA data from the blue to the red grid, we utilize bilinear interpolation[85]. Within bilinear interpolation, the interpolated value for every red grid point is determined by using the blue grid point coordinates and values within the blue square that the red point lies in. The coordinates of the four vertices on a blue grid are denoted as $Q_{11} = (x_1, y_1)$, $Q_{12} = (x_1, y_2)$, $Q_{21} = (x_2, y_1)$, and $Q_{22} = (x_2, y_2)$, and corresponding values are denoted as $f(Q_{11})$, $f(Q_{12})$, $f(Q_{21})$, and $f(Q_{22})$. This bilinear interpolation takes the form shown in Equation 6.6.

$$
\begin{aligned}
f(x,y) &\approx \frac{y_2-y}{y_2-y_1} f(x,y_1) + \frac{y-y_1}{y_2-y_1} f(x,y_2) \\
&= \frac{y_2-y}{y_2-y_1}\left[\frac{x_2-x}{x_2-x_1} f(Q_{11}) + \frac{x-x_1}{x_2-x_1} f(Q_{21})\right] + \frac{y-y_1}{y_2-y_1}\left[\frac{x_2-x}{x_2-x_1} f(Q_{12}) + \frac{x-x_1}{x_2-x_1} f(Q_{22})\right]
\end{aligned} \tag{6.6}
$$

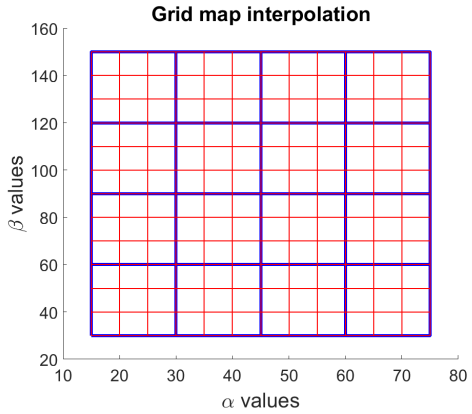

Figure 6.5: Grid map differences: the blue margin is a 5-by-5 grid map formed by simulation results from FEA, and the red margin is the target 13-by-13 grid map

Setup of Regression analysis

With bilinear interpolation, we obtain the stiffness and Poisson's ratio contours with a denser grid and provide more data points for fitting the regression model. Since $(K, \nu) \sim C + F_{0.5}(\alpha^{0.5}, \beta^{0.5}) + F_1(\alpha, \beta) + F_{1.5}(\alpha^{1.5}, \beta^{1.5}) + F_2(\alpha^2, \beta^2) + ... + O(\alpha^n, \beta^n)$, we consider up to a third order polynomial in each variable α and β in order to select a regression model with reasonable complexity. For cross terms, we consider up to a second-order polynomial.

However, the regression model is still complex and overfits the model. Hence, we conduct Stepwise Regression[29] analysis to extract significant features and use adjusted R-squared ($\geqslant 0.75$) and P-values ($\alpha \leqslant 0.05$) as our selection criteria to select significant terms.

6.5 Results and Discussion

We first compare the global mechanical responses of flexible and rigid Miura-Ori structures for isotropic materials in Section 6.5. Then in Section 6.5, we proceed with further in-depth studies on rigid Miura-Ori structures with different values of geometric parameters - α and β and materials - Aluminum and CFRP composite. This helps us understand how CFRP composite models perform compared to Aluminum models, and how the optimal geometry differs. We use regression analysis to explore the relationships between geometric parameters and global mechanical responses. We further optimize the Miura-Ori structures by proposing parameter R that linearly combines different targets (like stiffness and Poisson's ratio), as shown in Section 6.5. Finally in Section 6.5, we analyze woven composite models by changing the weaving patterns to establish how individual material properties control the global mechanical behavior.

Comparison between rigid Miura-Ori and flexible Miura-Ori structures

In order to compare the mechanical responses between rigid and flexible Miura-Ori structures, we subject the two models to two different load conditions: horizontal (X1) and vertical (X3) in-plane compression. Specifically, we choose the origami model with $\alpha = 45^\circ$ and $\beta = 90^\circ$ as a case study and compare the response between origami structures made of Aluminum and CFRP composites.

Table 6.2 shows the comparison between stiffness and Poisson's ratio between rigid and flexible Miura-Ori structures. We observe that adding flexible resin in the Miura-Ori hinges will significantly reduce the stiffness and the absolute value of negative Poisson's ratio (NPR) in specific loading directions. Thus for the remainder of this paper, we primarily consider origami structures without resin, that is, rigid Miura-Ori structures.

Table 6.2: Mechanical properties of Miura-Ori models with (flexible) and without (rigid) resin at the hinges

Loading Direction		Aluminum	Aluminum with Resin	CFRP	CFRP with Resin
In-plane X1 Load	Max K (N/(mm))	8.42	1.59	2.36	0.842
	Max NPR	-0.512	-0.887	-0.351	-0.707
In-plane X3 Load	Max K (N/(mm))	12.99	1.48	6.70	1.26
	Max NPR	-0.395	-0.395	-0.577	-0.399

Influence of geometric parameters on global mechanical responses

Next, we explore how the optimal stiffness and Poisson's ratio change with respect to different geometric angles within rigid Miura-Ori structures with isotropic (Aluminum) and directional (CFRP composite) material. To explore such behavior, we consider the mechanical loading of Miura-Ori models in horizontal in-plane compression (X1) and vertical in-plane compression (X3). We calculate weight normalized properties, effective stiffness, and Poisson's ratio. For different values of angles α and β, the weight normalized value for any property is defined as $S_{norm} = S/m$, where S is the property, and m is the weight of the geometry. We then investigate optimal origami structures by comparing the normalized mechanical properties between isotropic and directional materials.

Weight normalized stiffness and Poisson's ratio in compression along X1 axis

Figure 6.6 and Figure 6.7 show the weight normalized stiffness and Poisson's ratio maps for directional and isotropic Miura-Ori structures when compressed in the X1 direction. Specifically, to represent the negative Poisson's ratio in the Log scale, we calculate the Log scale of the absolute value of the negative Poisson's ratio and then add the negative sign. The horizontal and vertical axes in these figures are the geometric angles - α

and β that control model's shape. From Figure 6.6 and Figure 6.7, we observe the following:

1. Figure 6.6(a) shows the weight normalized stiffness contour for the isotropic case, where we observe that the optimal geometry corresponding to maximum stiffness occurs when α approaches 0° and β approaches 180°. As α decreases, the structure is compact in the X3 direction, which is perpendicular to X1. While, as β increases, the structure approaches a flat surface. Consequently, these two scenarios in combination result in a stiffer structure when compressed along the X1 direction. On the other hand, we notice that the optimal geometry that manifests the maximum value of negative weight normalized Poisson's ratio corresponds to α and β approaching 0°.
2. Compared to the isotropic model, the directional model has a similar optimal shape with respect to both stiffness and Poisson's ratio. Moreover, when fiber direction is in line with the loading direction, as in **case 1** shown in Figure 6.2(a), we observe that the directional model can manifest higher magnitudes of maximum normalized stiffness and negative Poisson's ratio compared to the isotropic model when compressed along X1 direction.

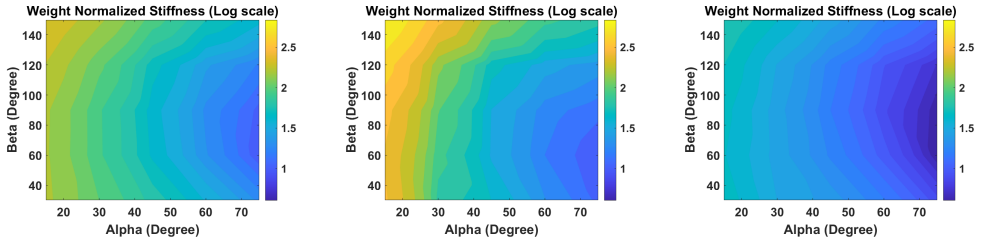

(a) (b) (c)

Figure 6.6: Weight normalized stiffness values $(N/(mm*g))$ of Miura-Ori models when compressed along X1: (a) isotropic case (b) fiber direction Case 1 (c) fiber direction Case 2

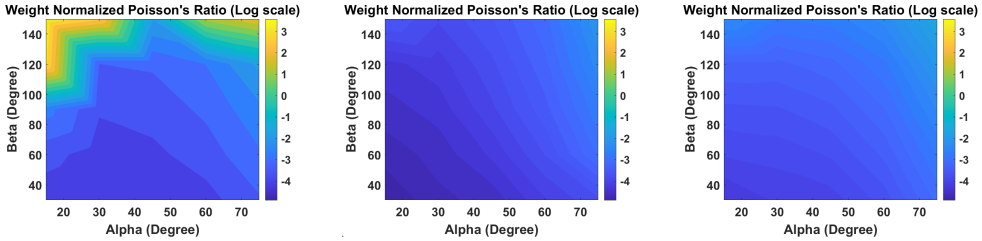

(a) (b) (c)

Figure 6.7: Weight normalized Poisson's ratio values $(1 \times 10^3/g)$ of Miura-Ori models when compressed along X1: (a) isotropic case (b) fiber direction case 1 (c) fiber direction case 2

Weight normalized stiffness and Poisson's ratio in compression along X3 axis

Figure 6.8 and Figure 6.9 show the weight normalized stiffness and Poisson's ratio values for directional and isotropic Miura-Ori structures when compressed along X3 direction.

From Figures 6.8 and 6.9, we observe the following:

1. From the stiffness contour for the isotropic model shown in Fig-

ure 6.8(a), we observe that the optimal geometry that has the maximum stiffness corresponds to α approaching 0° and β approaching 180°. This optimal geometry is similar to that determined for the previous loading direction: compression along X1. Figure 6.3(b) shows an example Miura-Ori structure with very small α (15°) and large β (150°). As for Poisson's ratio, we notice that the optimal geometry to possess a maximum value of negative weight normalized Poisson's ratio corresponds to α approaching 90° and β approaching 60° as shown in Figure 6.9(a).

2. Compared to the isotropic model, the directional model (fiber direction case 1 and case 2) has similar optimal geometric parameters for both stiffness and Poisson's ratio values. However, we notice that the material direction in Miura-Ori structures dramatically influences on the value of weight normalized stiffness and Poisson's ratio. When the fiber direction is in the same direction of load, as in **case 2** shown in Figure 6.2(a), directional Miura-Ori structures can effectively increase both maximum weights normalized stiffness and negative Poisson's ratio in the X3 direction as compared to the isotropic Miura-Ori structure.

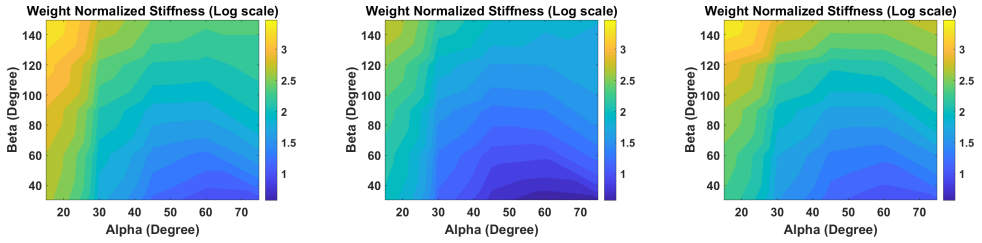

(a) (b) (c)

Figure 6.8: Weight normalized stiffness values $(N/(mm*g))$ of Miura-Ori models when compressed along X3: (a) isotropic case (b) fiber direction case 1 (c) fiber direction case 2

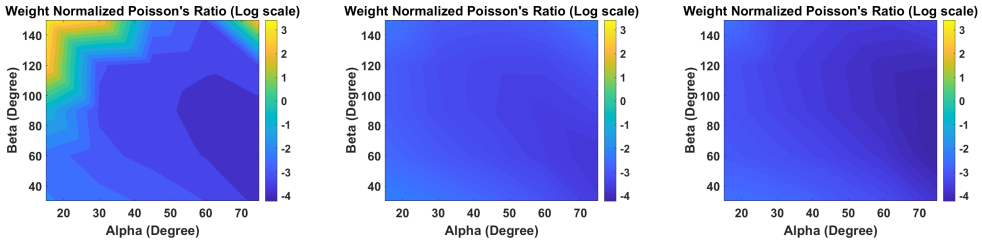

(a) (b) (c)

Figure 6.9: Weight normalized Poisson's ratio values $(1 \times 10^3/g)$ of Miura-Ori models when compressed along X3: (a) isotropic case (b) fiber direction case 1 (c) fiber direction case 2

Miura-Ori structure optimization based on regression analysis

In order to optimize the Miura-Ori structure, we introduce a regression analysis approach to mathematically represent the stiffness and Poisson's ratio of Miura-Ori structures as described in Section 6.4. In this section, we will first validate the accuracy of our proposed regression model by comparing it to FEA results. We will then use our regression model to

establish the optimal geometric parameters of the Miura-Ori structure based on different stiffness and Poisson's ratio values.

Regression model selection and performance prediction

From the Stepwise Regression analysis discussed in Section 6.4, we observe that nine parameters related to α and β are significant for representing the regression model. However, after setting up the regression model, we noticed that parameters related to $\alpha^{0.5}$ could cause large over-fitting issues. Thus we keep seven significant parameters and set up our regression model as Equation 7.1.

$$\begin{aligned} K &= w_{01} + w_{11}\alpha + w_{21}\alpha^2 + w_{31}\alpha^3 + w_{41}\beta + w_{51}\beta^2 + w_{61}\beta^3 + w_{71}\alpha\beta \\ \nu &= w_{02} + w_{12}\alpha + w_{22}\alpha^2 + w_{32}\alpha^3 + w_{42}\beta + w_{52}\beta^2 + w_{62}\beta^3 + w_{72}\alpha\beta \end{aligned} \tag{6.7}$$

where w_{ij} refer to different regression coefficients.

Figure 6.10 and 6.11 show examples of how the regression model predicts the contour compared to our FEA results on stiffness and Poisson's ratio when loading is applied in the X1 direction. Comparing the contours (a)-(b) and (c)-(d) in the two figures, we notice that our regression model could effectively capture the contour trend and the maximum/minimum locations and also provide a good prediction of the nodal values.

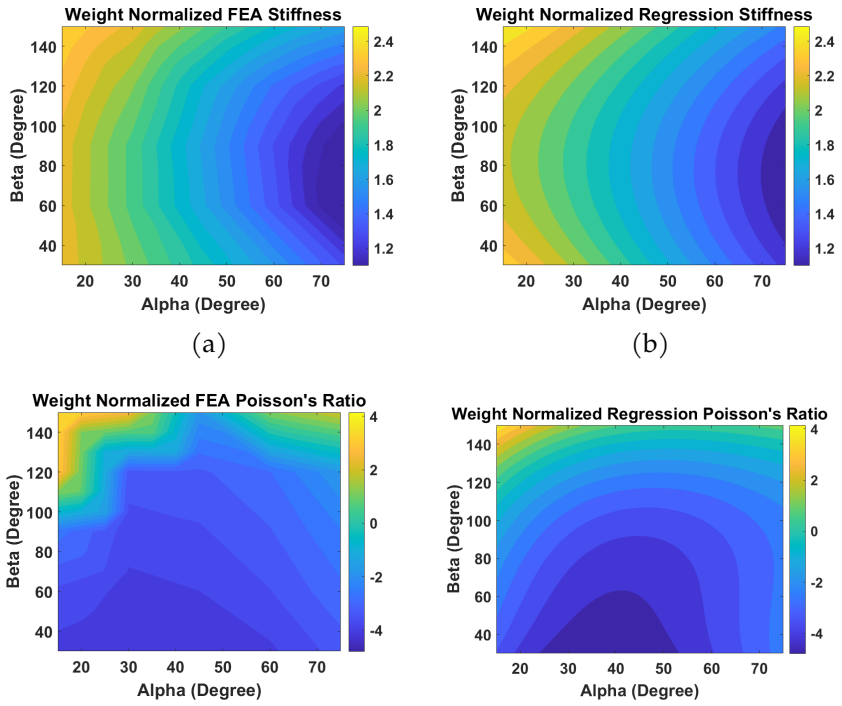

Figure 6.10: Comparison of regression model prediction and FEA results of Miura-Ori structures with isotropic material: (a) FEA contour and (b) regression model predicted contour for weight normalized stiffness $(N/(mm * g))$; (c) FEA contour and (d) regression model predicted contour for weight normalized Poisson's ratio $(1 \times 10^3/g)$. Compressive loading was applied in the X1 direction.

Optimal Miura-Ori structure considering stiffness and Poisson's ratio

After obtaining the regression model, we further utilize the model to determine optimal geometry with respect to the model's stiffness and Poisson's ratio. To set up a model combining different regression models for stiffness and Poisson's ratio, we define an abstract parameter R, which

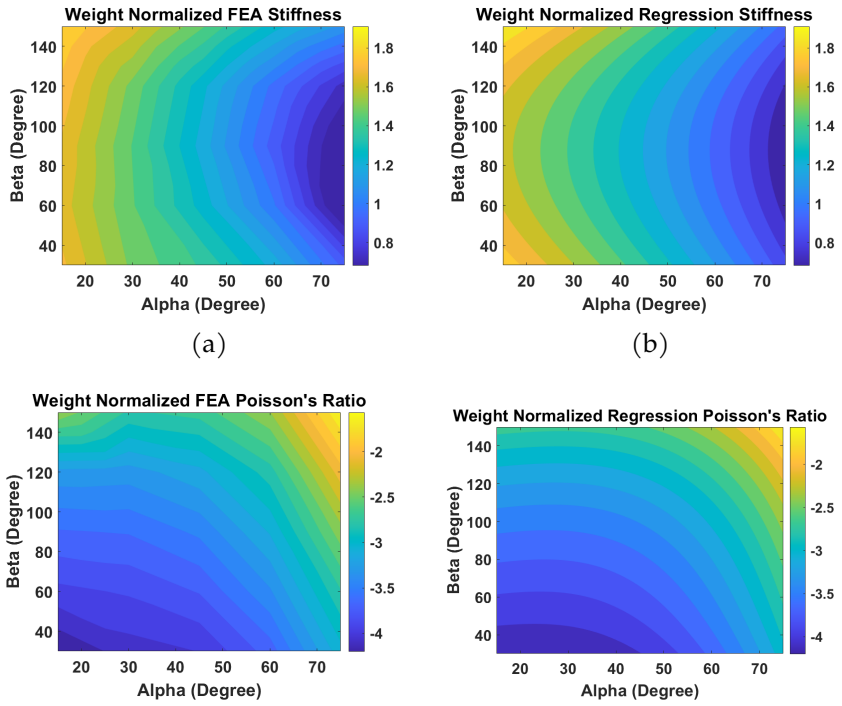

Figure 6.11: Comparison of regression model prediction and FEA results of Miura-Ori structures with directional material: (a) FEA contour and (b) regression model predicted contour for weight normalized stiffness ($N/(mm * g)$); (c) FEA contour and (d) regression model predicted contour for weight normalized Poisson's ratio ($1 \times 10^3/g$). Compressive loading was applied in the X1 direction.

is the linear combination of two normalized parameters: $R = c_1 \frac{K}{|K|_{max}} + (-1)^n (1-c_1) \frac{\nu}{|\nu|_{max}}$, where $c_1 \in [0, 1]$, is a coefficient that reflects the weights between stiffness and Poisson's ratio and can be arbitrarily adjusted. For example, c_1 can be set to a smaller value if we focus on Poisson's ratio's optimization. n is a value that controls the sign of the second term: $n = 1$ when we want maximum stiffness and maximum negative Poisson's ratio,

and $n = 2$ when we want maximum stiffness and maximum positive Poisson's ratio. $|K|_{max}$ and $|\nu|_{max}$ are the max absolute values of the stiffness and Poisson's ratio contours, which are constants and can be set as a value based on FEA analysis or user's knowledge.

To determine the optimal geometry, we take the first derivative of the function R and set it to zero, as shown in Equation 6.8.

$$\begin{aligned} R_\alpha &= \frac{\partial R}{\partial \alpha} = \frac{c_1}{|K|_{max}} \frac{\partial K}{\partial \alpha} + (-1)^n \frac{1-c_1}{|\nu|_{max}} \frac{\partial \nu}{\partial \alpha} = 0 \\ R_\beta &= \frac{\partial R}{\partial \beta} = \frac{c_1}{|K|_{max}} \frac{\partial K}{\partial \beta} + (-1)^n \frac{1-c_1}{|\nu|_{max}} \frac{\partial \nu}{\partial \beta} = 0 \end{aligned} \tag{6.8}$$

Equation 6.8 generates a system of equations with respect to α and β. Pairs of α and β could uniquely determine the Miura-Ori pattern. For example, here, we consider the weights between stiffness and Poisson's ratio to be the same, that is, $c_1 = 0.5$. In Figure 6.12, we plot the contour of R for isotropic and directional Miura-Ori structures (where fiber and compression loading are in X3 direction) and calculate the analytical solution from the expression of R using Equation 6.8; it turns out the analytical solution matches with contour generated from discrete FEA data. This further proves that our proposed construction of abstract parameter R can linearly combine optimization requirements on both stiffness and Poisson's ratio analytically and numerically.

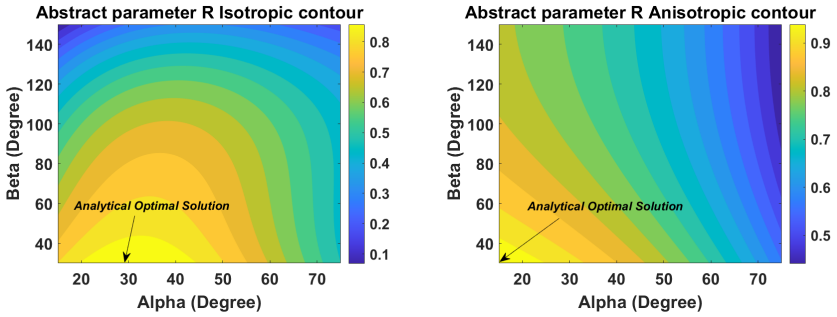

(a) (b)

Figure 6.12: Map of the abstract parameter R for Miura-Ori structures under compression loading in the X3 direction with (a) an isotropic material model and (b) a directional material model (fiber in the X3 direction). Also shown is the optimal geometry determined using the contour and regression model analytical solution.

Influence of individual material property on Miura-Ori structures

To understand how different material properties affect the Miura-Ori structure given fixed geometric parameters α and β, we consider several structures with fixed geometries and test how different materials change the structure's mechanical responses. For example, we consider different combinations of $\alpha = 30^\circ$ $\beta = 60^\circ$, $\alpha = 30^\circ$ $\beta = 90^\circ$, $\alpha = 45^\circ$ $\beta = 90^\circ$, $\alpha = 75^\circ$ $\beta = 60^\circ$ and $\alpha = 75^\circ$ $\beta = 90^\circ$.

Here we show an example of a Miura-Ori structure with $\alpha = 45^\circ$ and $\beta = 90^\circ$, but the same conclusion is valid for other combinations mentioned above. First, we investigate how a composite's individual material property controls the Miura-Ori structure's mechanical response. We consider

six different artificial materials as shown in Table 6.3 where we change individual material properties of the CFRP composites. Here, we envision that the Miura-Ori structure could be made of woven composites since we can change its in-plane responses with different weave patterns and yarn materials. This enables us to investigate how in-plane material property influences the corresponding mechanical responses by generating a series of artificial materials. Hence, Miura-Ori structures are generated based on woven CFRP composite, and we substitute some material properties with Aluminum to consider artificial woven materials. Table 6.4 shows the Miura-Ori structure's mechanical responses for this geometry combination ($\alpha, \beta = 45°, = 90°$) under X1 direction load for different artificial materials.

Table 6.3: Input material properties of artificial woven materials

	E_1 (GPa)	E_2 (GPa)	E_3 (GPa)	ν_{12}	ν_{23}	ν_{13}	G_{12} (GPa)	G_{23} (GPa)	G_{13} (GPa)
CFRP Woven	85	85	12.1	0.3	0.3	0.3	5	0.765	0.765
Artificial Woven 1	70	70	70	0.3	0.3	0.3	5	0.765	0.765
Artificial Woven 2	70	70	70	0.33	0.33	0.33	5	0.765	0.765
Artificial Woven 3	70	70	70	0.3	0.3	0.3	26.9	26.9	26.9
Artificial Woven 4	85	85	12.1	0.3	0.3	0.3	26.9	26.9	26.9
Artificial Woven 5	85	85	12.1	0.33	0.33	0.33	26.9	26.9	26.9
Artificial Woven 6	85	85	12.1	0.4	0.4	0.4	5	0.765	0.765

Table 6.4: Mechanical properties of different woven composites under load in X1 direction

$\alpha = 45°, \beta = 90°$	CFRP Woven	Artificial Woven 1	Artificial Woven 2	Artificial Woven 3	Artificial Woven 4	Artificial Woven 5	Artificial Woven 6
Stiffness K_c (N/mm)	3.15	3.15	3.15	9.14	9.14	10.10	3.37
Poisson's ratio	-0.887	-0.887	-0.887	-0.585	-0.585	-0.520	-0.851

From the results in Table 6.4, we show that: the shear modulus has the

most significant impact on the Miura-Ori structure's compressive stiffness K_c and Poisson's ratio (specifically NPR) compared to other parameters. On the other hand, compression modulus has the least influence, and the same trends are observed under load in the X3 direction.

Moreover, to understand how individual shear modulus (G_{12}, G_{23}, G_{13}) controls the Miura-Ori structure's mechanical responses, we test different combinations of in-plane and out-of-plane shear modules and calculate the Increase Rate (IR) of K_c and NPR for different shear modulus. Here IR is defined as the increase of targeting mechanical property based on the unit increase in shear modulus. We calculate the IR of the Miura-Ori structure with different values of α and β. Table 6.5 shows the IR of some example models, where Model 1 has $\alpha = 30°$, $\beta = 90°$, Model 2 has $\alpha = 45°$, $\beta = 90°$ and Model 3 has $\alpha = 75°$, $\beta = 90°$.

Table 6.5: Miura-Ori structure's mechanical responses Increase Rate (IR) under load in X1 direction

Control material property	Model 1		Model 2		Model 3	
	K_c IR	NPR IR	K_c IR	NPR IR	K_c IR	NPR IR
In-plane shear modulus	0.13	5.26	0.25	22.90	1.52	137.20
Out-of-plane shear modulus	0.15	0.22	0.05	0.35	0.05	0.91

where K_c increase rate has the unit of $N/(mm * GPa)$ and NPR increase rate has the unit of $1/GPa$.

According to the results in Table 6.5, we conclude that: (1) the out-of-plane shear modulus is slightly dominant on the structure's stiffness (K_c) when α is small. As α increases, in-plane shear modulus rapidly becomes more significant for the structure's stiffness. (2) the in-plane shear modulus

always plays a dominant role on NPR compared to the out-of-plane shear modulus. The same trend is also observed under loading in the X3 direction. Thus, we conclude that the in-plane shear modulus generally has the most significant role in controlling the Miura-Ori structure's mechanical response than the out-of-plane shear modulus.

6.6 Conclusions

This paper presents a detailed analysis of isotropic and directional Miura-Ori structures' mechanical responses using Finite Element Analysis. We investigated the Miura-Ori structure's optimal geometry for different materials and loading conditions. We proposed a regression model that can represent the relationship between the structure's geometric parameters (α, β) and its mechanical response and determine the optimal shape analytically. At last, using the notion that flexibility in composite material properties could potentially be achieved using different weave patterns and yarn materials, we analyzed how individual material property is controlling the structure's mechanical responses. The relationship of material and geometric parameters to the Miura-Ori structure's mechanical responses explored in this paper and the regression model to analytically represent the Miura-Ori structure can be further used in the future to guide the Miura-Ori structure design and optimization.

Key contributions to this paper are:

1. This is the first attempt to understand how material properties and geometric parameters influence the Miura-Ori structure, especially for directional Miura-Ori models (like CFRP composite).

2. We analyze isotropic and directional Miura-Ori structures with different geometries. We conclude that composite materials within the Miura-Ori structure could improve the mechanical responses compared to the isotropic model. This leads to more flexibility in Miura-Ori structural design and application.

3. We investigate the relationship between the geometric parameters and mechanical response (stiffness, negative Poisson's ratio) of Miura-Ori structures with isotropic and directional materials. We determine that the optimal geometry is similar for different materials considered.

4. To balance the optimization requirement between different mechanical responses, like stiffness and negative Poisson's ratio, we present a regression analysis to analytically represent the mechanical responses as a function of geometric parameters. The regression models are further used to predict the Miura-Ori structure's mechanical responses analytically and deliver optimal design.

5. We show that shear modulus is dominant in controlling the Miura-Ori structure's stiffness and Poisson's ratio among different material properties. We demonstrate this by using woven composites and

their flexibility in potentially changing the material properties within Miura-Ori structures.

7 DENSIFICATION MECHANICS OF POLYMERIC SYNTACTIC FOAMS

Pavana Prabhakar, Haotian Feng, Sabarinathan P. Subramaniyan, Mrityunjay Doddamani, Densification Mechanics of Polymeric Syntactic Foams, Composites Part B: Engineering 232 (2022): 109597.

Abstract

In this paper, a fundamental understanding of the densification mechanics of polymeric syntactic foams under compressive loading is established. These syntactic foams are closed cell composite foams with thin-walled microballoons dispersed in a matrix (resin) whose closed cell structure provides excellent mechanical properties, like high strength and low density. There are several parameters that can contribute towards their mechanical properties, including, microballoon volume fraction, microballoon wall thickness, bonding between the microballoons and the matrix, and the crushing strength of microballoons. Conducting purely experimental testing by varying these parameters can be very time sensitive and expensive. Also, identification of densification mechanics is challenging using experiments only. Higher densification stress and energy are favorable properties under foam compression or crushing. Hence, the influence of key structural and material parameters associated with syntactic foams

that dictate the mechanics of densification is studied here by implementing micromechanics based computational models and multiple linear regression analysis. Specifically, specific densification stresses and energy, which are densification stresses and energy normalized by weight, are evaluated which are more relevant for a wide variety of weight saving applications. Microballoon crushing strength and volume fraction are identified as the parameters that have the higher influence on densification stress and energy, and their specific counterparts, whereas the interfacial bonding has the least impact. In addition, designing aspects of syntactic foams with specified overall density are discussed by mapping microballoon volume fraction and wall thickness. The regression model allows for establishing wall thicknesses and corresponding volume fractions that result in higher densification properties for a specified overall foam density.

7.1 Parametric Space

Table 7.1 shows the types and range of parameters considered in this study. Four different GMB volume fractions V_{mb} are considered, which includes 0% (pure HDPE resin), 20%, 40% and 60% by volume of GMBs in the model domain. Varying extents of interfacial bonding between GMBs and HDPE resin are modeled by considering coefficient of friction values of $\mu_f = 1$ (perfect bonding), 0.1 (intermediate bonding) and 0.01 (no bonding). Compressive stress-strain responses are first determined

with linear elastic properties of GMBs. This is followed by considering elastic - perfectly plastic properties for the GMBs to model their crushing under compressive loading. The plastic yield strengths (σ_p) considered are 100, 1,000 and 10,000 MPa. In each model, all GMBs are considered to have the same strength values, and a distribution is not considered here. It is worth noting that crushing can initiate at some weaker GMBs first followed by stronger ones. Hence, this is a limitation of our model. Two wall thicknesses (t) of 1.08 μm [66] and 2.16 μm (double that of the first) are considered for the GMBs. The outer radius of the GMBs is maintained constant at 22.5 μm and the wall thickness changes towards the interior of the hollow particle. This ensures that the matrix volume fraction is maintained, while the GMB thickness is varied.

Table 7.1: Parameters considered in this study

Parameter	Parameter Range
GMB Volume Fraction (V_{mb} %)	0, 20, 40, 60
Coefficient of Friction (μ_f)	1.0, 0.1, 0.01
GMB Material Type	Linear Elastic, Perfectly Plastic
GMB Plastic Yield Strength (σ_p MPa)	10^2, 10^3, 10^4
GMB Wall Thickness (t μm)	1.08 , 2.16

7.2 Multiple Linear Regression Analysis

Multiple linear regression analysis explores the relationships between several independent variables ($x_1, x_2, ..., x_n$) and a targeted dependent variable (y) through fitting a linear equation as shown in Equation 7.1.

Coefficients of this linear equation $(a_0, a_1, ..., a_n)$ describe how each independent variable controls the value of the target variable,

$$y = a_0 + a_1x_1 + a_2x_2 + a_3x_3 + a_4x_4 + ... + a_nx_n \tag{7.1}$$

Four different parameters shown in Table 7.1 are used as independent variables (except GMB material type) and four different target variables are considered: densification stress, specific densification stress, densification energy and specific densification energy. Independent variables are re-scaled within the range of [0,1] using min-max scaling defined in Equation 7.2.

$$x' = \frac{x - \min x}{\max x - \min x} \tag{7.2}$$

In this paper, volume fraction (V_{mb}), plastic yield strength (σ_p) and wall thickness (t) are rescaled as $\hat{V}_{mb}$, $\hat{\sigma}_p$ and $\hat{t}$, respectively. Since the minimum value for these three parameters can be zero, we set the minimum value to be zero and maximum value to be the maximum data sample value we obtained. Equation considered for each target variable is shown in Equation 7.3, and details about the *cross terms* will be discussed in

section 7.3.

$$\begin{aligned}
\textit{densification stress} &= a_{01} + a_{11}\hat{t} + a_{21}\hat{\sigma}_p + a_{31}\hat{V}_{mb} + a_{41}\mu_f + \textit{cross terms} \\
\textit{specific densification stress} &= a_{02} + a_{12}\hat{t} + a_{22}\hat{\sigma}_p + a_{32}\hat{V}_{mb} + a_{42}\mu_f + \textit{cross terms} \\
\textit{densification energy} &= a_{03} + a_{13}\hat{t} + a_{23}\hat{\sigma}_p + a_{33}\hat{V}_{mb} + a_{43}\mu_f + \textit{cross terms} \\
\textit{specific densification energy} &= a_{04} + a_{14}\hat{t} + a_{24}\hat{\sigma}_p + a_{34}\hat{V}_{mb} + a_{44}\mu_f + \textit{cross terms}
\end{aligned} \tag{7.3}$$

7.3 Results

Compressive Response of GMB/HDPE Syntactic Foams

The hyperelastic response of HDPE was successfully modeled using the experimental compressive stress-strain response obtained from Jayavardhan and Doddamani [66] as shown in Figure 7.1 (Cyan). The compressive stress-strain response of syntactic foams with varying GMB volume fractions and particle size distributions were modeled first assuming linear elastic properties for the GMBs. The compressive stress-strain responses of syntactic foam models with varying GMB volume fractions, GMB wall thicknesses, and particle size distribution (uniform and polydistribution) are shown in Figure 7.1. GMB volume fractions of 17%, 35%, and 50% are considered in these models to compare against the experimental stress-strain responses from Jayavardhan and Doddamani[66]. The wall thickness (t) considered in the computational model of the thin wall case

(Figure 7.1(a)) matches that of the microballoon wall thickness in the experiments [66].)

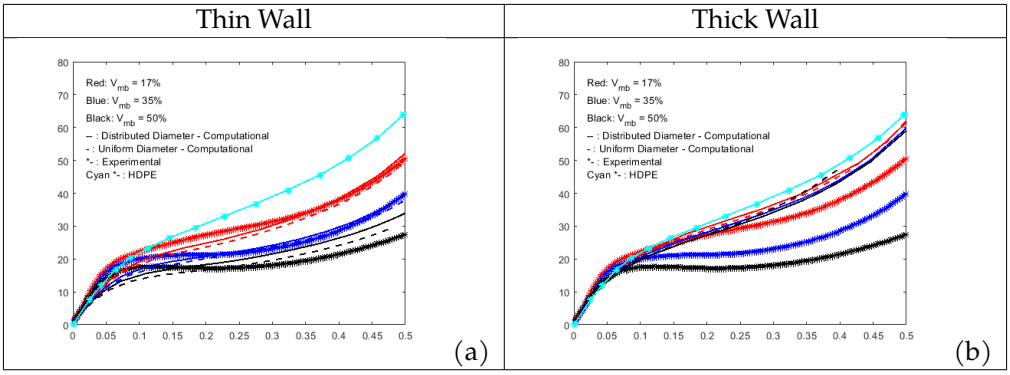

Figure 7.1: Comparison of experimental and computational compressive stress-strain response of foams with varying GMB volume fraction: (a) Thin wall GMBs; (b) Thick wall GMBs.

A general trend in these stress-strain responses is that increasing GMB volume fraction V_{mb} reduces the densification stresses. Densification stress is defined as the stress corresponding to 0.4 mm/mm compressive strain in this study. We also observe that the GMB size distribution has marginal impact on the stress-strain response compared to that with uniform GMB size. Thus, we will consider uniform GMB size for the remainder of this paper.

As compared to experimental stress-strain graphs, the densification stresses computationally determined for the thin wall case are comparable for lower V_{mb} like 17% and 35%, but are higher for higher V_{mb} like in the case of 50%. This is because, as the V_{mb} increases, their collapse has a higher impact on the densification stresses and thus needs to be captured in the

model. Hence, next we considered elastic - perfectly plastic properties for the GMB particles, which will be discussed in the next section. It is worth noting that the difference in the compressive stress-strain responses determined computationally for thick walled GMB models with linear elastic properties have lesser variation with changing V_{mb} as shown in Figure 7.1(b).

Densification Stresses and Energy Absorption of GMB/HDPE Syntactic Foams

Compressive stress-strain response of GMB/HDPE syntactic foam models with elastic - perfectly plastic properties for the GMBs is presented here. The plastic yield strength (σ_p) values are considered to be 10^2, 10^3 and 10^4 MPa, which represent different crushing strengths of the GMBs. Figure 7.2 shows the compressive stress-strain graphs for different GMB volume fractions (V_{mb}), GMB wall thicknesses (t), and interfacial bonding (μ_f) between GMB and HDPE. These are compared against the compressive stress-strain response of pure HDPE.

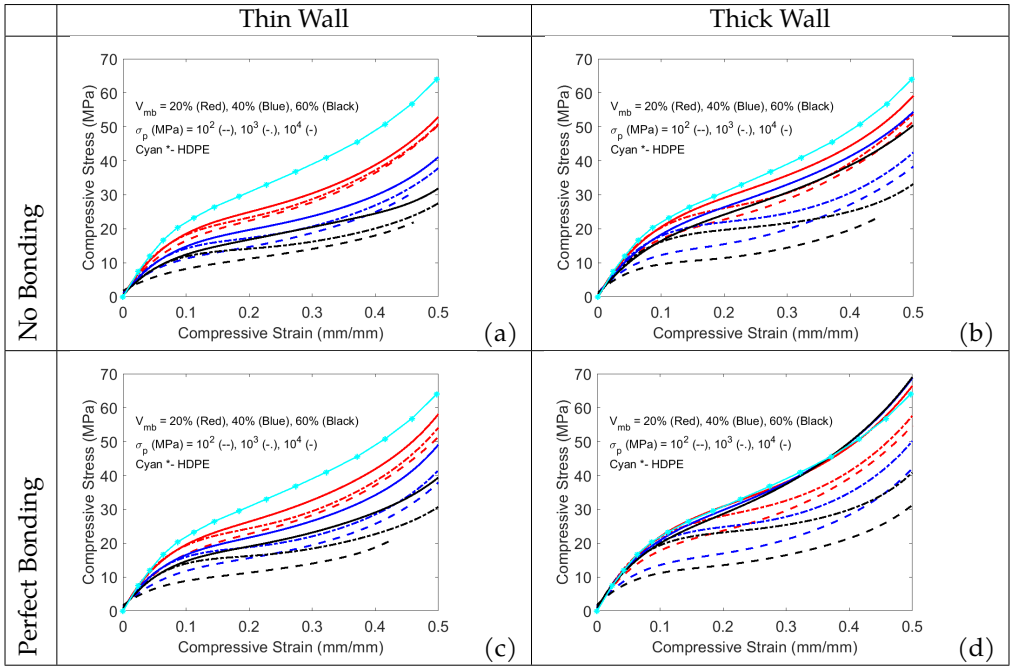

Figure 7.2: Compressive stress-strain response of foams with varying GMB volume fraction V_{mb}. (a) Thin wall thickness and no interfacial bonding; (b) Thick wall thickness and no interfacial bonding; (c) Thin wall thickness and perfect interfacial bonding; (d) Thick wall thickness and perfect interfacial bonding

As expected, increasing the GMB volume fraction V_{mb} decreases the densification stresses. Further, higher GMB σ_p increases the densification stresses as higher stresses are required to crush the GMBs. Higher t improves the compressive response, however, special attention should be paid towards weight gain due to an increase in GMB wall thickness. This is addressed in the following sections by presenting maps of weight normalized densification stress and energy absorption values with varying foam parameters. In general, we observe that better interfacial bonding

μ_f results in a slight improvement in the overall compressive response. This is a manifestation of improved load transfer due to good bonding between the microballoons and matrix in the syntactic foams that prevents microballoons from slipping.

Densification stresses

Next we compare the densification stresses for the complete parametric space that was investigated within this study. Figure 7.3 shows maps of densification stresses which indicate the influence of GMB volume fraction, GMB/HDPE bonding, GMB yield strength, and GMB wall thickness. The densification stresses increase with increasing plastic yield strength for each GMB volume fraction, regardless of interfacial bonding and GMB wall thickness. This is expected as the densification stress depends on the crushing strength of GMB particles.

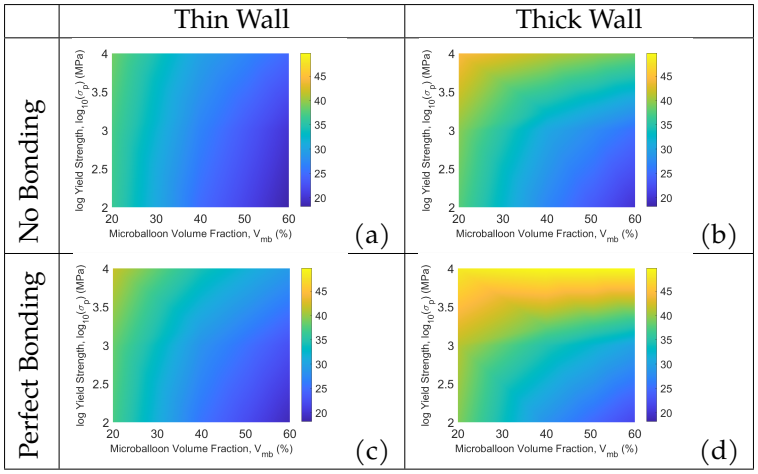

Figure 7.3: Maps of densification stresses with varying GMB volume fraction V_{mb}, plastic yield strength σ_p, wall thickness and GMB/HDPE interfacial bonding

Although densification stress maps shown in Figure 7.3 provide insights into the influence of individual parameters, it is more interesting and valuable to compare the specific densification stresses, that is, weight normalized densification stresses. Note that the weight of syntactic foams decrease with increasing GMB volume fraction, but also increase with increasing wall thickness.

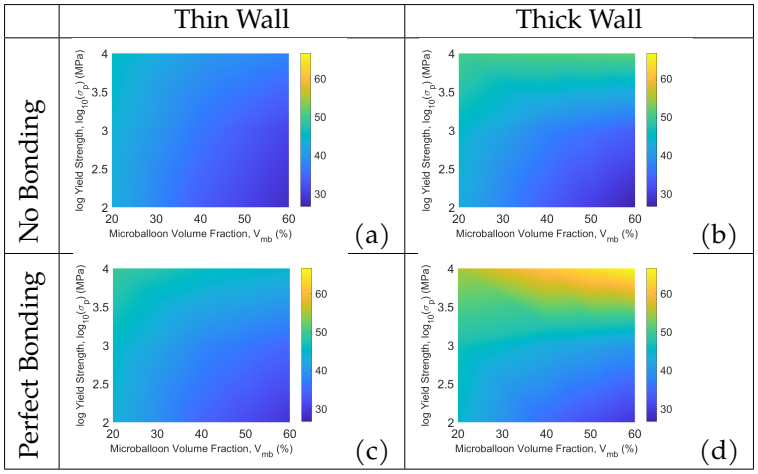

Figure 7.4: Maps of specific densification stresses with varying GMB volume fraction V_{mb}, plastic yield strength σ_p, wall thickness and GMB/HDPE interfacial bonding

Figure 7.4 shows the maps of specific densification stresses with varying GMB volume fraction, plastic yield strength of GMB particles, GMB wall thickness, and GMB/HPDE interfacial bonding. For syntactic foams with thin walled GMBs (Figure 7.4 (a) and (c)), the specific densification stresses decrease with increasing GMB volume fraction for all GMB strength values and the type of GMB/HDPE bonding. Enhanced interfacial bonding does improve the specific densification stresses (Figure 7.4(c)), and its effect is pronounced at higher GMB strengths. For syntactic foams with thick walled GMBs and no bonding at the GMB/HDPE interfaces (Figure 7.4(b)), the trend of specific densification stresses is similar to that of syntactic foams with thin walled GMBs at lower GMB yield strengths. However, a change in this trend is observed at higher GMB yield strengths,

and is pronounced in syntactic foams with thick walled GMBs and perfect bonding at GMB/HDPE interfaces (Figure 7.4(d)). That is, the specific densification stresses decrease with increasing GMB volume fraction with low strength GMBs, however, they increase with increasing GMB volume fraction with high strength GMBs. Mathematical description of such trends using regression analysis is shown later in section 7.3.

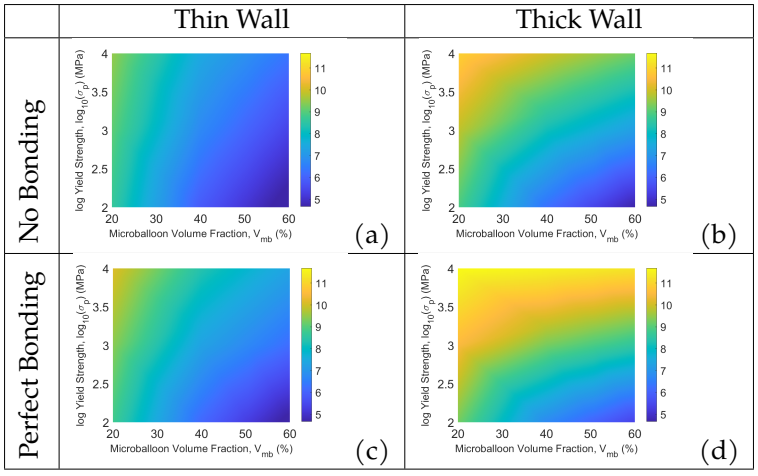

Figure 7.5: Maps of densification energy with varying GMB volume fraction V_{mb}, plastic yield strength σ_p, wall thickness and GMB/HDPE interfacial bonding

Densification Energy

Next we present maps of densification energy similar to that of the densification stresses for all the parameters considered in this study. Densification energy is defined as the area under the compressive stress-strain graphs until a compressive strain of 0.4 mm/mm. Figure 7.5 and Figure 7.6 show the maps of densification energy and specific densification energy. The

trend in these properties are similar to that of densification stresses and specific densification stresses, respectively.

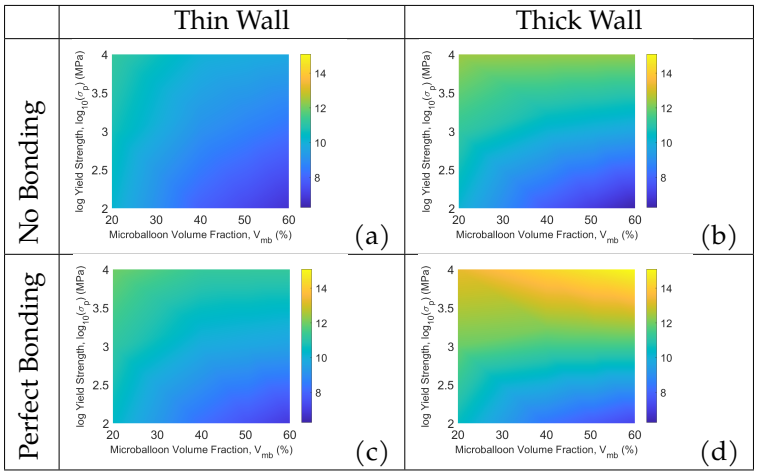

Figure 7.6: Maps of specific densification energy with varying GMB volume fraction V_{mb}, plastic yield strength σ_p, wall thickness and GMB/HDPE interfacial bonding

Deformation of GMB/HDPE Syntactic Foams

Next we visually compare the deformation contour maps of syntactic foams corresponding to a compressive strain of 0.4 mm/mm as shown in Figure 7.7. As compared to Figure 7.7(a), we observe that the walls of the GMB particles are debonded from the matrix (HDPE) in Figure 7.7(b) due to poor or no interfacial bonding. Further, the GMB particles in Figure 7.7(b) are more severely deformed, that is, they have lower stability as compared to those in Figure 7.7(a) when other parameters are held constant. We also observe that GMB particles with higher yield strength and

thicker walls have better structural stability against crushing or collapse.

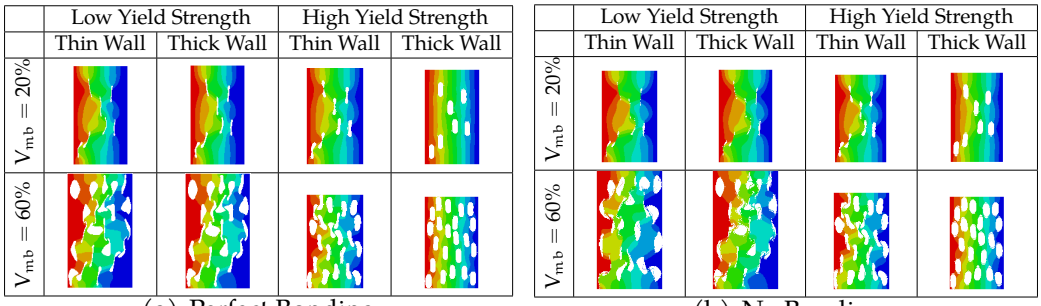

(a) Perfect Bonding (b) No Bonding

Figure 7.7: Displacement field along the x-axis at 0.4 mm/mm compressive strain

Identifying the Influence of Individual Parameters

Although insightful, the maps of densification stresses, energy, and their specific values shown in Figures 7.3 to 7.6 do not provide clear distinction about particular parameters that have the highest or the lowest influence on these properties. Hence, we present here the results from a multiple linear regression analysis that will aid us in identifying the influence of individual parameters considered in this study. We first determine the form of the linear regression models for the four targeted variables (densification stress, specific densification stress, densification energy, and specific densification energy) as shown in Equations 7.3. In addition to wall thickness (t), yield stress (σ_p), microballoon volume fraction (V_{mb}), and coefficient of friction (μ_f), Figures 7.4 and 7.6 reveal that cross terms related to V_{mb} can change the trends in specific densification stress and

specific energy absorption. For instance, in Figure 7.4(d), specific densification stress reduces with increasing volume fraction at yield strength of 100 MPa. However, this property increases with increasing volume fraction at yield strength of 10,000 MPa. This indicates the existence of cross term $\hat{\sigma}_p\hat{V}_{mb}$ that needs to be considered in our regression model. Similarly, comparisons between Figure 7.4(b) and Figure 7.4(d) as well as Figure 7.4(c) and Figure 7.4(d) suggest that cross terms $\hat{t}\hat{V}_{mb}$ and $\mu_f\hat{V}_{mb}$ may have a impact on the regression model. Thus, the expanded expression for Equation 7.3 is shown in Equation 7.4.

$$
\begin{aligned}
ds &= a_{01} + a_{11}\hat{t} + a_{21}\hat{\sigma}_p + a_{31}\hat{V}_{mb} + a_{41}\mu_f + a_{51}\hat{t}\hat{V}_{mb} + a_{61}\hat{\sigma}_p\hat{V}_{mb} + a_{71}\mu_f\hat{V}_{mb} \\
sds &= a_{02} + a_{12}\hat{t} + a_{22}\hat{\sigma}_p + a_{32}\hat{V}_{mb} + a_{42}\mu_f + a_{52}\hat{t}\hat{V}_{mb} + a_{62}\hat{\sigma}_p\hat{V}_{mb} + a_{72}\mu_f\hat{V}_{mb} \\
de &= a_{03} + a_{13}\hat{t} + a_{23}\hat{\sigma}_p + a_{33}\hat{V}_{mb} + a_{43}\mu_f + a_{53}\hat{t}\hat{V}_{mb} + a_{63}\hat{\sigma}_p\hat{V}_{mb} + a_{73}\mu_f\hat{V}_{mb} \\
sde &= a_{04} + a_{14}\hat{t} + a_{24}\hat{\sigma}_p + a_{34}\hat{V}_{mb} + a_{44}\mu_f + a_{54}\hat{t}\hat{V}_{mb} + a_{64}\hat{\sigma}_p\hat{V}_{mb} + a_{74}\mu_f\hat{V}_{mb}
\end{aligned}
\tag{7.4}
$$

We obtained the coefficients for each dependent variable by performing multiple linear regression analysis in Matlab and Python. The coefficients are shown in Figure 7.8. Note that the sign of a_{3i} is negative. The values of coefficients are further validated with bootstrapping method, which expands the data set and delivers more stable statistical properties. Relatively high values of cross-term coefficients support the necessity of introducing cross-terms into the regression model. The signs of the first four coefficients (a_{1i}, a_{2i}, a_{3i} and a_{4i}, where i=1,4), can be visually veri-

fied in Figures 7.3 to 7.6. For instance, in Figure 7.3(a)-(d), densification stress decreases with increasing V_{mb} (horizontally) while increases with increasing σ_p (vertically), indicating that densification stress is negatively correlated with V_{mb} and positively correlated with σ_p. A comparison between Figure 7.3(a) and (b) proves that the sign for $\hat{t}$ is positive, and that between (b) and (d) proves that the sign for μ_f is also positive. To summarize how these four independent parameters and cross-terms influence our target variables quantitatively, we group our target variables into 1) densification terms and 2) specific densification terms.

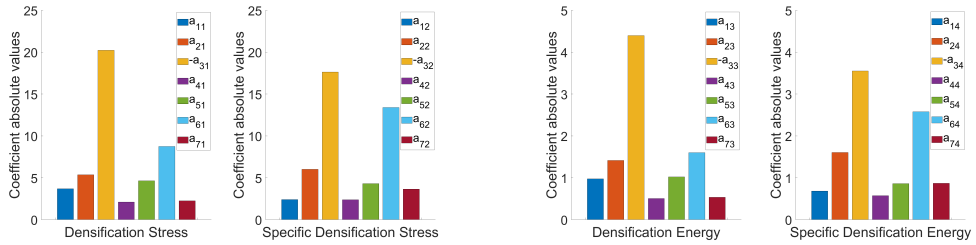

Figure 7.8: Coefficients from multiple linear regression analysis

- Densification terms

  Coefficients of densification stress have trends similar to that of densification energy as discussed previously in section 7.3. $\hat{V}_{mb}$ (a_{31} and a_{33}) has the highest influence on these targets, followed by the cross term $\hat{\sigma}_p\hat{V}_{mb}$ (a_{61} and a_{63}) and $\hat{\sigma_p}$ (a_{21} and a_{23}), indicating that microballoon volume fraction and yield strength are the two parameters

that have the highest influence over the values of densification stress and energy absorption in the normalized scale. Among all other terms, μ_f and its corresponding cross term have the least influence. The influence of the coefficients corresponding to variables $\hat{t}$, $\hat{\sigma}_p$, $\hat{V}_{mb}$, and μ_f can be visually inspected from the contour maps shown in Figures 7.3 and 7.5. For instance, in Figure 7.3, color changes in the horizontal direction (volume fraction) in each plot is more significant than that along the vertical direction (yield strength). A comparison between maps Figure 7.3(a)-(b) and Figure 7.3(a)-(c) indicate that the influence of wall thickness is higher than the extent of bonding. This corroborates our finding from the regression analysis, where the absolute value of coefficient corresponding to volume fraction is the highest followed by yield strength and their corresponding cross term, while the coefficient corresponding to μ_f has the lowest value. This observation is in-line with that established experimentally by prior researchers [122, 66, 10, 106] that the influence of interface is lower on the compressive response of syntactic foams compared to that of tensile response.

- Specific densification terms

  Coefficients of specific densification stress also have trends similar to that of specific densification energy. $\hat{V}_{mb}$ has the highest influence on these targets, followed by cross term $\hat{\sigma}_p\hat{V}_{mb}$ and variable $\hat{\sigma}_p$.

However, when compared to the coefficients in the corresponding densification terms, the relative significance of $\hat{t}$, $\hat{V}_{mb}$ and $\hat{t}\hat{V}_{mb}$ are reduced. An intuitive understanding of this phenomenon is that the specific values are evaluated by per unit mass, where the total mass is a function of $\hat{V}_{mb}$ and $\hat{t}$. Hence, the coefficients of $\hat{t}$ (a_{12} and a_{14}), $\hat{V}_{mb}$ (a_{32} and a_{34}) and $\hat{t}\hat{V}_{mb}$ (a_{52} and a_{54}) are expected to reduce their influence on the specific densification quantities as compared to the coefficients of the densification terms. As a result, the significance of $\hat{\sigma}_p\hat{V}_{mb}$ (a_{62} and a_{64}) and $\hat{\sigma_p}$ (a_{22} and a_{24}) increased. Thus, we further confirmed our visual observation with our regression model.

To summarize, GMB volume fraction and crushing strength have higher influence over the densification and specific densification stress and energy terms. These parameters can be controlled during fabrication by choosing the material of GMB for their strength and the amount of particles added to achieve a particular volume fraction.

Design Aspects - Syntactic Foams with Specified Overall Density

Syntactic foams can be designed with different GMB volume fractions and wall thicknesses. However, it is possible to achieve the same overall density of syntactic foam with multiple different pairs of volume fraction and wall thickness. In this section, we will discuss how the densification

and specific densification stresses change for syntactic foams with the same overall density. The conclusions can be extended to densification energy terms as well.

The overall density (ρ_o) of syntactic foam is a function of the volume fraction and wall thickness as shown in Equation 7.5.

$$\rho_o = \frac{M_o}{Vol_o} = \frac{\rho_m Vol_m + \rho_{mb} Vol_{mb}}{Vol_o} = \rho_m(1 - V_{mb}) + \rho_{mb} V_{mb} \frac{r^2 - (r-t)^2}{r^2} \tag{7.5}$$

where, subscript m is for matrix, mb is for microballoon, and o is for the overall syntactic foam. ρ is the density. V_{mb} is the GMB volume fraction in the syntactic foam. M is the mass and Vol is the volume. r is the outer radius of GMBs, and t is the wall thickness.

By rearranging Equation 7.5, we can derive a relationship between GMB volume fraction and wall thickness as shown in Equation 7.6.

$$V_{mb} = \frac{\rho_o - \rho_m}{\rho_{mb} \frac{r^2-(r-t)^2}{r^2} - \rho_m} \tag{7.6}$$

We can graph Equation 7.6 for different values of overall syntactic foam densities as shown in Figure 7.9, which is a visualization of the relation between the two parameters for several constant overall densities of syntactic foams. Each curve in this figure is an isoline for density with varying pair of V_{mb} and t.

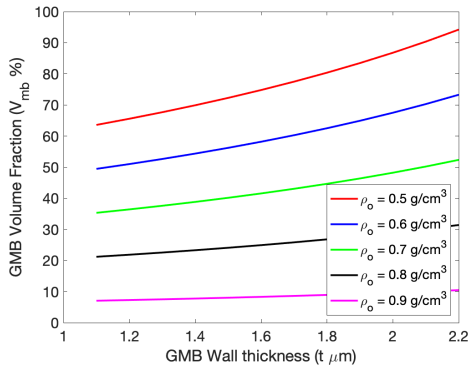

Figure 7.9: Variation of GMB volume fraction with wall thickness for several specified syntactic foam densities

From Figure 7.9, we observe that for a fixed overall foam density (that is, a particular curve), the GMB volume fraction increases as the wall thickness increases. That is, syntactic foams with lower volume fractions and thinner GMB walls can have the same overall density as that of foams with higher volume fractions and thicker GMB walls.

To understand how different combinations of GMB wall thicknesses and volume fractions impact the densification and specific densification stresses, we utilize our trained regression model from Section 7.3 to estimate theses quantities. For demonstration, we pick the perfect bonding syntactic foam as our test case and a requirement of overall foam density to be $\rho_o = 0.66 g/cm^3$. Density of HDPE matrix and GMBs are considered to be $\rho_m = 0.95 g/cm^3$ and $\rho_r = 2.54 g/cm^3$, respectively. Outer radius of the GMBs is 22.5 μm. Discrete yield strength (σ_p) values of 100 MPa, 1000 MPa, 3000 MPa, 6000 MPa, and 10000 MPa are considered for the GMBs.

Wall thickness t is allowed to continuously vary from 1.1μm to 2.2μm. Based on Equation 7.6, the GMB wall thickness changes will result in V_{mb} to change from 40% to 60%.

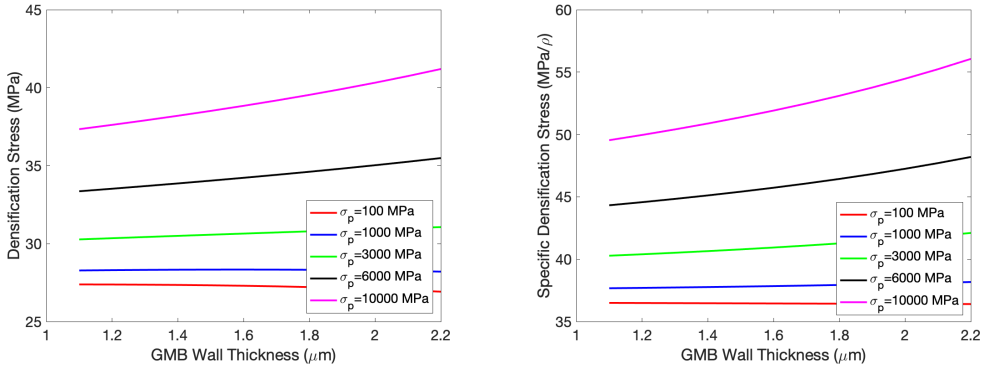

(a) (b)

Figure 7.10: (a) Densification stress and (b) specific densification stress with varying GMB wall thickness

By applying min-max normalization to these new parameters and using our regression model, we obtain the densification stress and specific densification stress plots as a function of wall thickness t as shown in Figure 7.10. From Figure 7.10, we can conclude that for different syntactic foams with the same overall density: (1) both densification stress and specific densification stress will in general increase as the wall thickness increases (and consequently volume fraction increases). (2) higher GMB strength leads to more significant changes in both quantities as the wall thickness increases. Such trends can also be visualized and validated from Figure 7.3 and 7.4. Thus, if we want higher densification and specific densification stresses,

but keeping the syntactic foam density constant, we should choose GMBs with larger wall thickness and at higher volume fractions. Higher strength of the GMBs will further increase these quantities. It is worth noting that the GMBs with thicker walls can have higher crushing strength, adding further to the overall increase in densification quantities.

7.4 Conclusion

In this paper, we presented the mechanisms of densification in syntactic foams with GMBs embedded in HDPE resin. We developed computational models to understand the influence of key syntactic foam parameters including, microballoon volume fraction (V_{mb}), wall thickness (t), yield strength (σ_p), and the extent of interfacial bonding between microballoons and matrix (μ_f). We elucidated the influence of these parameters on densification stress and energy, and their corresponding specific (weight normalized) values. Further, we developed a multiple regression model to identify the influence of parameters that have higher influence on these properties. Finally, we also performed a case study to explore design aspects of syntactic foams with specified foam density, and the influence of wall thickness and volume fraction on densification properties. Key conclusions from our study are summarized here:

- Densification stress and energy increase with increasing plastic yield strength for all GMB volume fractions, regardless of interfacial bond-

ing and GMB wall thickness. This is reflective of the dependence of densification stress and energy on the crushing strength of GMB particles.

- Although densification properties provide insights into the influence of individual parameters, it is more interesting and valuable to compare the specific densification properties, that is, densification property divided by the weight of the corresponding syntactic foam. The weight of syntactic foams decreases with increasing GMB volume fraction, but increases with increasing wall thickness.

- In general, specific densification stress and energy decrease with increasing microballoon volume fraction, and increase with increasing microballoon yield strength for thin walled GMBs. However, we observe a change in this trend for syntactic foams thick walled GMBs at higher yield strength GMBs. Note that wall thickness influences the weight of syntactic foams, but also increase crushing strength of microballoons. Hence, the specific densification stress and energy increase with increasing GMB volume fraction in syntactic foams with high crushing strength and thick walled GMBs.

- The regression analysis performed in this study corroborated the above-mentioned observations. That is, GMB crushing strength and volume fraction showed higher influence over the values of specific densification stress and specific densification energy, whereas in-

terfacial bonding has the least influence. These parameters can be controlled during fabrication by choosing the material and wall thickness of GMB for their strength, and the amount of particles added to achieve a specified microballoon volume fraction.

- We further investigated the design aspects for syntactic foams with a specified overall density. For a specified overall syntactic foam density, there exists a one-to-one mapping between the GMB volume fraction and GMB wall thickness. Based on our regression model, we show that a syntactic foam with higher GMB wall thickness and higher volume fraction is preferred over one with lower GMB wall thickness and lower volume fraction, although they could have the same overall foam density. This is because the former case results in higher densification properties. Moreover, higher strength GMBs will further improve these quantities.

8 ONGOING PROJECTS

In addition to the research presented in this dissertation, I am currently working on several ongoing projects in the field of composite material analysis and optimization, using a variety of machine learning techniques. These projects include:

Robust Physics-informed neural network (PINN) for composite material design In this project, the focus is on developing a robust Physics-Informed Neural Network (PINN) to solve the heterogeneous Poisson equation, which governs the behavior of composite materials. While PINNs have shown promise in solving various partial differential equations (PDEs), their performance can be limited in the presence of large behavior transitions resulting from material transitions in composite materials. This project aims to address this issue by developing a more robust PINN for solving the heterogeneous Poisson equation. Additionally, the project extends to an inverse PINN problem, where the goal is to discover the governing parameters within the Poisson equation using measured scatter data.

Detecting microplastics using image segmentation and classification This project focuses on using image segmentation and classification techniques to detect defects in composite materials, specifically microplastics in water flow. The first step is to use clustering and the Masked R-CNN

algorithm to identify the location of microplastics. Then, the microplastics are classified based on the reflected color from different wavelength lights.

Prediction of mechanical properties for 3D syntactic foam composite My previous research primarily focused on analyzing 2D composite materials. However, in this project, I am utilizing machine learning methods to predict the mechanical properties of 3D syntactic foam composites based on their microstructure and composition.

Optimizing composite material using Reinforcement Learning In my previous work, I demonstrated that reinforcement learning algorithms can help find optimal composite material designs by making simple geometric changes to micromechanical models[33]. This project extends that research to more complex syntactic foam composite models with random variables such as microballoon size, number, and location within the matrix.

Summary Overall, these ongoing research projects highlight the potential of machine learning techniques to revolutionize the field of composite material analysis and optimization. By combining the power of deep learning with knowledge-based models and optimization algorithms, we can develop more efficient and accurate approaches to designing composite materials with tailored mechanical properties for specific applications.

9.1 Key Contributions

My research investigates the potential of machine learning techniques for composite material analysis and optimization. Specifically, I propose knowledge-based machine learning frameworks that integrate existing knowledge with machine learning to enhance prediction accuracy, particularly when data is limited. The key contributions of my research are as follows:

1. I proposed a method to incorporate knowledge in the input, within neural network architecture, and in the loss function to improve the accuracy of predicting mechanical properties of composite materials. This approach is especially useful when data is limited, and can enhance the effectiveness of machine learning algorithms in composite material analysis.

2. I investigated the use of statistical learning and reinforcement learning methods to optimize composite materials, which is a novel approach in the field. This exploration reveals the potential of machine learning algorithms to enhance composite material properties beyond the current state-of-the-art methods.

3. The proposed frameworks can be applied to improve the design of a wide range of composite material systems, with potential appli-

cations in industries such as aerospace, automotive, and renewable energy. The findings of this research can inspire further investigation in this area and lead to the development of even more advanced techniques for optimizing the performance of composite materials.

Overall, the key contributions of this research demonstrate the potential of machine learning in composite material analysis and optimization. These findings contribute to the ongoing development of advanced techniques for improving the performance of composite materials.

9.2 Future Research

While this dissertation has made significant progress in using machine learning for composite material analysis and optimization, there are still many avenues for future research in this area. Here are some potential directions for further study:

Transfer learning : Machine learning models trained on one composite material system may not be directly applicable to another system. Future research could explore the use of transfer learning techniques to adapt machine learning models trained on one composite material system to new systems, potentially reducing the amount of data required.

Robustness and generality : Our framework focuses on optimizing the mechanical properties of composite materials, but there are other factors

to consider, such as their robustness and reliability under different loading conditions. Future research could explore the use of machine learning to optimize composite materials for these additional factors.

Real-time optimization : The optimization process in our framework requires significant computational resources, which may be impractical in some real-world scenarios. Future research could explore the use of machine learning to develop real-time optimization algorithms that can quickly optimize composite materials on the fly.

Data-driven material design : Our framework requires a large amount of data to develop accurate machine learning models. Future research could explore the use of generative models, such as generative adversarial networks (GANs), to generate synthetic data that can be used to train machine learning models for composite material design.

Overall, these possible future research directions suggest that machine learning has the potential to revolutionize the design of composite materials, and we hope that this dissertation will inspire further research in this exciting and rapidly evolving field.

BIBLIOGRAPHY

[1] J. Wang A. Khadilkar and R. Rai. Deep learning–based stress prediction for bottom-up sla 3d printing process. *The International Journal of Ad-vanced Manufacturing Technology*, pages 1–15, 2019.

[2] DW Abueidda, M Almasri, R Ammourah, U Ravaioli, IM Jasiuk, and NA Sobh. Prediction and optimization of mechanical properties of composites using convolutional neural networks. *Composite Structures*, 227:111264, 2019.

[3] Y. Afshar, S. Bhatnagar, S. Pan, K. Duraisamy, and S. Kaushik. Prediction of aerodynamic flow fields using convolutional neural networks. 05 2019.

[4] I. Amidror. Scattered data interpolation methods for electronic imaging systems: A survey. *Journal of Electronic Imaging*, 11, 04 2002.

[5] M. J. Atalla and D. J. Inman. On model updating using neural networks. *Mechanical Systems and Signal Processing*, 12(1):135 – 161, 1998.

[6] V Badrinarayanan, A Kendall, and R Cipolla. Segnet: A deep convolutional encoder-decoder architecture for image segmentation. *IEEE transactions on pattern analysis and machine intelligence*, 39(12):2481–2495, 2017.

[7] HT Bang, S Park, and H Jeon. Defect identification in composite materials via thermography and deep learning techniques. *Composite Structures*, 246:112405, 2020.

[8] E. Barbero. *Finite Element Analysis of Composite Materials*. 01 2008.

[9] Y. Bengio and Y. Lecun. Convolutional networks for images, speech, and time-series. 11 1997.

[10] B.R. Bharath Kumar, M. Doddamani, S.E. Zeltmann, N. Gupta, M.R. Ramesh, and S. Ramakrishna. Processing of cenosphere/HDPE syntactic foams using an industrial scale polymer injection molding machine. *Materials and Design*, 92:414–423, 2016.

[11] L. Bottou. *On-line Learning and Stochastic Approximations*, page 9–42. Publications of the Newton Institute. Cambridge University Press, 1999.

[12] K Bousmalis, N Silberman, D Dohan, D Erhan, and D Krishnan. Unsupervised pixel-level domain adaptation with generative adversarial networks. In *Proceedings of the IEEE conference on computer vision and pattern recognition*, pages 3722–3731, 2017.

[13] P. Breunig, V. Damodaran, K. Shahapurkar, S. Waddar, M. Doddamani, P. Jeyaraj, and P. Prabhakar. Dynamic impact behavior of syntactic foam core sandwich composites. *Journal of Composite Materials*, 54(4):535–547, 2020.

[14] G.X. Gu C. Chen. Machine learning for composite materials. *MRS Communications*, 9(2):556–566, 2019.

[15] B. D. Caddock and K. E. Evans. Microporous materials with negative poisson's ratios. i. microstructure and mechanical properties. *Journal of Physics D: Applied Physics*, 22(12):1877–1882, dec 1989.

[16] JP Carey, GW Melenka, AJ Hunt, and C Ayranci. Introduction to braided composite material behavior. In *Handbook of Advances in Braided Composite Materials*, pages 207–237. Elsevier, 2017.

[17] AG Castellanos, Md S Islam, E Tarango, Y Lin, and P Prabhakar. Interlaminar reinforcement for enhancing low-velocity impact response of woven composites. *Textile Research Journal*, 88(15):1710–1720, 2018.

[18] CC Chamis. Mechanics of composite materials: Past, present, and future. *Journal of Composites Technology and Research*, 11(1):3–14, 1989.

[19] CT Chen and GX Gu. Generative deep neural networks for inverse materials design using backpropagation and active learning. *Advanced Science*, 7(5):1902607, 2020.

[20] K. Cho, v. M. Bart, D. Bahdanau, and Y. Bengio. On the properties of neural machine translation: Encoder-decoder approaches. 09 2014.

[21] D. Choqueuse and P. Davies. Ageing of composites in underwater applications. *Ageing Compos*, pages 467–498, 2008.

[22] A Conneau, H Schwenk, L Barrault, and Y Lecun. Very deep convolutional networks for natural language processing. *arXiv preprint arXiv:1606.01781*, 2(1), 2016.

[23] A. Creswell, T. White, V. Dumoulin, K. Arulkumaran, B. Sengupta, and A.A. Bharath. Generative adversarial networks: An overview. *IEEE Signal Processing Magazine*, 35(1):53–65, 2018.

[24] Jianxun Cui, Felipe R Poblete, and Yong Zhu. Origami/kirigami-guided morphing of composite sheets. *Advanced Functional Materials*, 28(44):1802768, 2018.

[25] Jeanette L Domber, Jason D Hinkle, Lee D Peterson, and Peter A Warren. Dimensional repeatability of an elastically folded composite hinge for deployed spacecraft optics. *Journal of spacecraft and rockets*, 39(5):646–652, 2002.

[26] K Dong, K Liu, Q Zhang, B Gu, and B Sun. Experimental and numerical analyses on the thermal conductive behaviors of carbon fiber/epoxy plain woven composites. *International Journal of Heat and Mass Transfer*, 102:501–517, 2016.

[27] M.L. du Bos, F. Balabdaoui, and J.N. Heidenreich. Modeling stress-strain curves with neural networks: a scalable alternative to the return mapping algorithm. *Computational Materials Science*, 178:109629, 2020.

[28] Y. Efendiev, J. Galvis, and T. Y. Hou. Generalized multiscale finite element methods (gmsfem). *Journal of Computational Physics*, 251:116 – 135, 2013.

[29] M. A. Efroymson. Multiple regression analysis. *Mathematical methods for digital computers*, pages 191–203, 1960.

[30] J. D. Emerson, editor. *Mathematical aspects of transformation*, pages 247–282. John Wiley, New York, 1983.

[31] H. Feng and P. Prabhakar. Difference-based deep learning framework for stress predictions in heterogeneous media. *Composite Structures*, 269:113957, 2021.

[32] H Feng, SP Subramaniyan, and P Prabhakar. Deep learning framework for woven composite analysis. In *Proceedings of the American Society for Composites—Thirty-Sixth Technical Conference on Composite Materials*, 2021.

[33] HAOTIAN FENG and PAVANA PRABHAKAR. Deep reinforcement learning for composite material optimization. In *Proceedings of the American Society for Composites â€" Thirty-fifth Technical Conference*, 2020.

[34] Haotian Feng and Pavana Prabhakar. Parameterization-based neural network: Predicting non-linear stress-strain response of composites. *arXiv preprint arXiv:2212.12840*, 2022.

[35] Haotian Feng, Sabarinathan P Subramaniyan, and Pavana Prabhakar. Physics-constrained neural network for the analysis and feature-based optimization of woven composites. *arXiv preprint arXiv:2209.09154*, 2022.

[36] Haotian Feng, Guanjin Yan, and Pavana Prabhakar. Role of material directionality on the mechanical response of miura-ori composite structures. *Composite Structures*, 306:116606, 2023.

[37] Sebastian Fischer, SEBASTIAN Heimbs, Sebastian Kilchert, Michael Klaus, and CHRISTOPH Cluzel. Sandwich structures with folded core: manufacturing and mechanical behavior. In *International SAMPE Europe Conference, Paris*, 2009.

[38] Jianyu Gao and Zhong You. Origami-inspired miura-ori honeycombs with a self-locking property. *Thin-Walled Structures*, 171:108806, 2022.

[39] Y Gao, C Xie, and Z Zheng. Textile composite electrodes for flexible batteries and supercapacitors: opportunities and challenges. *Advanced Energy Materials*, 11(3):2002838, 2021.

[40] C. D. Garcia, K. Shahapurkar, M. Doddamani, G. C. M. Kumar, and P. Prabhakar. Effect of arctic environment on flexural behavior of fly ash cenosphere reinforced epoxy syntactic foams. *Composites Part B: Engineering*, 151:265–273, 2018.

[41] G.M. Gladysz and K.K. Chawla. Syntactic and composite foams: Proceedings of an engineering conferences international (eci) conference. *Journal of Materials Science*, 41(13):3959–3960, 2006.

[42] Y Gowayed. Types of fiber and fiber arrangement in fiber-reinforced polymer (frp) composites. In *Developments in Fiber-Reinforced Polymer (FRP) Composites for Civil Engineering*, pages 3–17. Elsevier, 2013.

[43] GX Gu, CT Chen, DJ Richmond, and MJ Buehler. Bioinspired hierarchical composite design using machine learning: simulation, additive manufacturing, and experiment. *Materials Horizons*, 5(5):939–945, 2018.

[44] X. Guo, W. Li, and F. Iorio. Convolutional neural networks for steady flow approximation. In *Proceedings of the 22nd ACM SIGKDD International Conference on Knowledge Discovery and Data Mining*, KDD '16, page 481–490, New York, NY, USA, 2016. Association for Computing Machinery.

[45] N. Gupta and E. Woldesenbet. Microballoon wall thickness effects on properties of syntactic foams. *Journal of Cellular Plastics*, 40(6):461–480, 2004.

[46] N. Gupta, E. Woldesenbet, and P. Mensah. Compression properties of syntactic foams: effect of cenosphere radius ratio and specimen aspect ratio. *Composites Part A: applied science and manufacturing*, 35(1):103–111, 2004.

[47] N. Gupta, S.E. Zeltmann, V.C. Shunmugasamy, and D. Pinisetty. Applications of polymer matrix syntactic foams. *Jom*, 66(2):245–254, 2014.

[48] M Hall-Beyer. Glcm texture: A tutorial v. 3.0 march 2017. 2017.

[49] RM Haralick, K Shanmugam, and IH Dinstein. Textural features for image classification. *IEEE Transactions on systems, man, and cybernetics*, (6):610–621, 1973.

[50] F.E. Harrell Jr, K.L. Lee, R.M. Califf, D.B. Pryor, and R.A. Rosati. Regression modelling strategies for improved prognostic prediction. *Statistics in medicine*, 3(2):143–152, 1984.

[51] Y.M.A. Hashash, S. Jung, and J. Ghaboussi. Numerical implementation of a neural network based material model in finite element analysis. *International Journal for numerical methods in engineering*, 59(7):989–1005, 2004.

[52] K. He, X. Zhang, S. Ren, and J. Sun. Deep residual learning for image recognition. pages 770–778, 06 2016.

[53] Sebastian Heimbs, Peter Middendorf, Sebastian Kilchert, Alastair F Johnson, and Martin Maier. Experimental and numerical analysis of composite folded sandwich core structures under compression. *Applied Composite Materials*, 14(5):363–377, 2007.

[54] Carl T Herakovich. Mechanics of fibrous composites. *New York: John Wiley & Sons, Inc, 1998.*, 1998.

[55] E. Hille. *Analytic Function Theory*, volume 1. Chelsea Publishing Company, New York, 2 edition, 1982. footnote 1.

[56] T. Y. Hou and X. Wu. A multiscale finite element method for elliptic problems in composite materials and porous media. *Journal of Computational Physics*, 134(1):169 – 189, 1997.

[57] J. Hu, L. Shen, and G. Sun. Squeeze-and-excitation networks. 2018.

[58] T. Hughes. *The Finite Element Method: Linear Static and Dynamic Finite Element Analysis*, volume 78. 01 2000.

[59] M. W. Hyer and S. R. White. *Stress analysis of fiber-reinforced composite materials*. DEStech Publications, Inc, 2009.

[60] T Ishikawa and TW Chou. One-dimensional micromechanical analysis of woven fabric composites. *AIAA journal*, 21(12):1714–1721, 1983.

[61] P. Isola, J. Y. Zhu, T. Zhou, and A. A. Efros. Image-to-image translation with conditional adversarial networks. *CoRR*, abs/1611.07004, 2016.

[62] N. Japkowicz and S. Shaju. The class imbalance problem: A systematic study. *Intell. Data Anal.*, 6:429–449, 11 2002.

[63] B. Jasim and P. Taheri. An origami-based portable solar panel system. In *2018 IEEE 9th Annual Information Technology, Electronics and Mobile Communication Conference (IEMCON)*, pages 199–203. IEEE, 2018.

[64] M. L. Jayavardhan and D. Mrityunjay. Quasi-static compressive response of compression molded glass microballoon/hdpe syntactic foam. *Composites Part B Engineering*, 149, 06 2018.

[65] M.L. Jayavardhan and M. Doddamani. Quasi-static compressive response of compression molded glass microballoon/hdpe syntactic foam. *Composites Part B: Engineering*, 149:165–177, 2018.

[66] M.L. Jayavardhan and M. Doddamani. Quasi-static compressive response of compression molded glass microballoon/hdpe syntactic foam. *Composites Part B: Engineering*, 149:165 – 177, 2018.

[67] Haoliang Jiang, Zhenguo Nie, Roselyn Yeo, Amir Barati Farimani, and Levent Burak Kara. Stressgan: A generative deep learning model for two-dimensional stress distribution prediction. *Journal of Applied Mechanics*, 88(5), 2021.

[68] YP Jiang, WL Guo, and ZF Yue. Investigation of the three-dimensional micromechanical behavior of woven-fabric composites. *Mechanics of Composite Materials*, 42(2):141–150, 2006.

[69] L. Jing and Y. Tian. Self-supervised visual feature learning with deep neural networks: A survey. *IEEE transactions on pattern analysis and machine intelligence*, 43(11):4037–4058, 2020.

[70] Meredith Johnson, Yue Chen, Sierra Hovet, Sheng Xu, Bradford Wood, Hongliang Ren, Junichi Tokuda, and Zion Tsz Ho Tse. Fabricating biomedical origami: a state-of-the-art review. *International journal of computer assisted radiology and surgery*, 12(11):2023–2032, 2017.

[71] R. M. Jones. Mechanics of composite materials, second edition. CRC Press, 1999.

[72] P. Juszczak, D. Tax, and R. Duin. Feature scaling in support vector data description. 05 2002.

[73] AD Kelkar, JS Tate, and R Bolick. Structural integrity of aerospace textile composites under fatigue loading. *Materials Science and Engineering: B*, 132(1-2):79–84, 2006.

[74] J. F. Kenney and E. S. Keeping, editors. *Mathematics of Statistics*. second edition. Van Nostrand, New York, 1951.

[75] HA Khan, A Hassan, MB Saeed, F Mazhar, and IA Chaudhary. Finite element analysis of mechanical properties of woven composites through a micromechanics model. *Science and Engineering of Composite Materials*, 24(1):87–99, 2017.

[76] Z. S. Khozani, H. Bonakdari, and A. H. Zaji. Estimating the shear stress distribution in circular channels based on the randomized neural network technique. *Applied Soft Computing*, 58:441 – 448, 2017.

[77] V. Košmerl, I. Štajduhar, and M. Čanadija. Predicting stress–strain behavior of carbon nanotubes using neural networks. *Neural Computing and Applications*, pages 1–16, 2022.

[78] A. Krizhevsky, I. Sutskever, and G.E. Hinton. Imagenet classification with deep convolutional neural networks. *Advances in neural information processing systems*, 25, 2012.

[79] O. H. Kwon and J. H. Roh. Origami-inspired shape memory dual-matrix composite structures. *Journal of Intelligent Material Systems and Structures*, 30(17):2639–2647, 2019.

[80] C. Martin L. Liang and S. Sun. A deep learning approach to estimate stress distribution: a fast and accurate surrogate of finite-element analysis. *Journal of The Royal Society Interface, 15, 01*, 01 2018.

[81] A. Barton L. Puig and N. Rando. A review on large deployable structures for astrophysics missions. *Acta Astronautica*, 67(1):12 – 26, 2010.

[82] Roderic Lakes. Foam structures with a negative poisson's ratio. *Science*, 235(4792):1038–1040, 1987.

[83] P. Li, N. Petrinic, C.R. Siviour, R. Froud, and J.M. Reed. Strain rate dependent compressive properties of glass microballoon epoxy syntactic foams. *Materials Science and Engineering: A*, 515(1-2):19–25, 2009.

[84] S Li and A Wongsto. Unit cells for micromechanical analyses of particle-reinforced composites. *Mechanics of Materials*, 36(7):543–572, 2004.

[85] X. Li and M. T. Orchard. New edge-directed interpolation. *IEEE transactions on image processing*, 10(10):1521–1527, 2001.

[86] Yongkai Li, Weixuan Liu, Yang Deng, Wei Hong, and Hongyu Yu. Miura-ori enabled stretchable circuit boards. *npj Flexible Electronics*, 5(1):1–9, 2021.

[87] H Lin, LP Brown, and AC Long. Modelling and simulating textile structures using TexGen. *Advanced Materials Research*, 331:44–47, 2011.

[88] Sicong Liu, Guoxing Lu, Yan Chen, and Yew Wei Leong. Deformation of the miura-ori patterned sheet. *International Journal of Mechanical Sciences*, 99:130–142, 2015.

[89] X Liu, F Gasco, J Goodsell, and W Yu. Initial failure strength prediction of woven composites using a new yarn failure criterion constructed by deep learning. *Composite Structures*, 230:111505, 2019.

[90] AC Long. *Design and manufacture of textile composites*. Elsevier, 2005.

[91] R. Longadge and S. Dongre. Class imbalance problem in data mining review. *CoRR*, abs/1305.1707, 2013.

[92] P. L'Ecuyer. *Pseudorandom Number Generators*. 05 2010.

[93] J. Irizarry M. Nourbakhsh and J. Haymaker. Generalizable surrogate model features to approxi-mate stress in 3d trusses. *Engineering Applications of Artificial Intelligence*, pages 15–27, 01 2018.

[94] Z Mao, AD Jagtap, and GE Karniadakis. Physics-informed neural networks for high-speed flows. *Computer Methods in Applied Mechanics and Engineering*, 360:112789, 2020.

[95] A. Mardt, L. Pasquali, H. Wu, and F. Noé. Vampnets: Deep learning of molecular kinetics. *Nature Communications*, 9, 10 2017.

[96] Stefano Mintchev, Ludovic Daler, Géraud L'Eplattenier, Louis Saint-Raymond, and Dario Floreano. Foldable and self-deployable pocket sized quadrotor. In *2015 IEEE International Conference on Robotics and Automation (ICRA)*, pages 2190–2195. IEEE, 2015.

[97] P Moradweysi, PM Santucci, G Carta, T Goudarzi, MM Aghdam, A Baldi, and M Brun. Design and analysis of a thick miura-ori folded structure with large negative poisson's ratio. *Mechanics of Advanced Materials and Structures*, pages 1–19, 2022.

[98] AP Mouritz, MK Bannister, PJ Falzon, and KH Leong. Review of applications for advanced three-dimensional fibre textile composites. *Composites Part A: applied science and manufacturing*, 30(12):1445–1461, 1999.

[99] N. K. Naik and P. S.Shembekar. Elastic behavior of woven fabric composites: I—lamina analysis. *Journal of composite materials*, 26(15):2196–2225, 1992.

[100] NK Naik and VK Ganesh. Prediction of on-axes elastic properties of plain weave fabric composites. *Composites Science and Technology*, 45(2):135–152, 1992.

[101] D Nardi and J Sinke. Design analysis for thermoforming of thermoplastic composites: Prediction and machine learning-based optimization. *Composites Part C: Open Access*, 5:100126, 2021.

[102] Z. Nie, H. Jiang, and L. Kara. Stress field prediction in cantilevered structures using convolutional neural networks. *Journal of Computing and Information Science in Engineering*, page 1, 06 2019.

[103] A. Oishi and G. Yagawa. Computational mechanics enhanced by deep learning. *Computer Methods in Applied Mechanics and Engineering*, 327, 09 2017.

[104] SJ Pan and Q Yang. A survey on transfer learning. *IEEE Transactions on knowledge and data engineering*, 22(10):1345–1359, 2009.

[105] GD Pang, YC Lin, YL Qiu, YQ Jiang, YW Xiao, and MS Chen. Dislocation density–based model and stacked auto-encoder model for ti-55511 alloy with basket-weave microstructures deformed in α+ β region. *Advanced Engineering Materials*, 23(4):2001307, 2021.

[106] Balu Patil, B.R. Bharath Kumar, and Mrityunjay Doddamani. Compressive behavior of fly ash based 3d printed syntactic foam composite. *Materials Letters*, 254:246–249, 2019.

[107] F. Pedregosa, G. Varoquaux, A. Gramfort, V. Michel, B. Thirion, O. Grisel, M. Blondel, P. Prettenhofer, R. Weiss, V. Dubourg, J. Vanderplas, A. Passos, D. Cournapeau, M. Brucher, M. Perrot, and E. Duchesnay. Scikit-learn: Machine learning in Python. *Journal of Machine Learning Research*, 12:2825–2830, 2011.

[108] S. Pellegrino. *Deployable Structures in Engineering*, pages 1–35. Springer Vienna, Vienna, 2001.

[109] P. Prabhakar, H. Feng, S.P. Subramaniyan, and M. Doddamani. Densification mechanics of polymeric syntactic foams. *Composites Part B: Engineering*, 232:109597, 2022.

[110] P. Prabhakar and A. M. Waas. Interaction between kinking and splitting in the compressive failure of unidirectional fiber reinforced laminated composites. *Composite Structures*, 98:85 – 92, 2013.

[111] P. Prabhakar and A. M. Waas. Micromechanical modeling to determine the compressive strength and failure mode interaction of multidirectional laminates. *Composites Part A: Applied Science and Manufacturing*, 50:11 – 21, 2013.

[112] P. Prabhakar and A. M. Waas. Upscaling from a micro-mechanics model to capture laminate compressive strength due to kink banding instability. *Computational Materials Science*, 67:40 – 47, 2013.

[113] JL Raheja, S Kumar, and A Chaudhary. Fabric defect detection based on glcm and gabor filter: A comparison. *Optik*, 124(23):6469–6474, 2013.

[114] J. Reiman and P. Heppel. Deployable vehicle fairing structure, October 5 2004. US Patent 6,799,791.

[115] F. Haupert R.Medina and A. K. Schlarb. Improvement of tensile properties and toughness of an epoxy resin by nanozirconium-dioxide reinforcement. *Journal of Materials Science*, 43(9):3245–3252, 05 2008. Copyright - Journal of Materials Science is a copyright of Springer, (2008). All Rights Reserved; Last updated - 2019-07-19.

[116] Kazuya Saito, Sergio Pellegrino, and Taketoshi Nojima. Manufacture of arbitrary cross-section composite honeycomb cores based on origami techniques. *Journal of Mechanical Design*, 136(5):051011, 2014.

[117] Pooya Sareh, Pisak Chermprayong, Marc Emmanuelli, Haris Nadeem, and Mirko Kovac. Rotorigami: A rotary origami protective system for robotic rotorcraft. *Science Robotics*, 3(22):eaah5228, 2018.

[118] M. Schenk and S. D. Guest. Geometry of miura-folded metamaterials. *Proceedings of the National Academy of Sciences*, 110(9):3276–3281, 2013.

[119] T Schlegl, P Seeböck, SM Waldstein, U Schmidt-Erfurth, and G Langs. Unsupervised anomaly detection with generative adversarial networks to guide marker discovery. In *International conference on information processing in medical imaging*, pages 146–157. Springer, 2017.

[120] B Sebastian V, A Unnikrishnan, and K Balakrishnan. Gray level co-occurrence matrices: generalisation and some new features. *arXiv preprint arXiv:1205.4831*, 2012.

[121] R. Sepasdar, A. Karpatne, and M. Shakiba. A data-driven approach to full-field damage and failure pattern prediction in microstructure-dependent composites using deep learning. *arXiv preprint arXiv:2104.04485*, 2021.

[122] K. Shahapurkar, C. D. Garcia, M. Doddamani, G. C. M. Kumar, and P. Prabhakar. Compressive behavior of cenosphere/epoxy syntactic foams in arctic conditions. *Composites Part B: Engineering*, 135(June 2017):253–262, 2018.

[123] K. Shahapurkar, C.D. Garcia, M. Doddamani, G.M. Kumar, and P. Prabhakar. Compressive behavior of cenosphere/epoxy syntactic foams in arctic conditions. *Composites Part B: Engineering*, 135:253–262, 2018.

[124] V.C. Shunmugasamy, N. Gupta, N.Q. Nguyen, and P.G. Coelho. Strain rate dependence of damage evolution in syntactic foams. *Materials Science and Engineering: A*, 527(23):6166–6177, 2010.

[125] D Singh and K Kaur. Classification of abnormalities in brain mri images using glcm, pca and svm. *International Journal of Engineering and Advanced Technology (IJEAT)*, 1(6):243–248, 2012.

[126] Michael Smith. *ABAQUS/Standard User's Manual, Version 6.9*. Dassault Systèmes Simulia Corp, United States, 2009.

[127] W. M. Sokolowski and S. C. Tan. Advanced self-deployable structures for space applications. *Journal of Spacecraft and Rockets*, 44(4):750–754, 2007.

[128] B. Song, W. Chen, T. Yanagita, and D.J. Frew. Confinement effects on the dynamic compressive properties of an epoxy syntactic foam. *Composite Structures*, 67(3):279–287, 2005.

[129] N Souly, C Spampinato, and M Shah. Semi supervised semantic segmentation using generative adversarial network. In *Proceedings of the IEEE international conference on computer vision*, pages 5688–5696, 2017.

[130] A. E. Standage and R. Prescott. High elastic modulus carbon fibre. *Nature*, page 211, 07 1966.

[131] G. P. H. Styan. Hadamard products and multivariate statistical analysis. *Linear Algebra and its Applications*, 6:217 – 240, 1973.

[132] P. N. SubbaNarasimha, B. Arinze, and M. Anandarajan. The predictive accuracy of artificial neural networks and multiple regression in the case of skewed data: exploration of some issues. *Expert Systems with Applications*, 19(2):117 – 123, 2000.

[133] I. Sutskever, O. Vinyals, and Q. Le. Sequence to sequence learning with neural networks. *Advances in Neural Information Processing Systems*, 4, 09 2014.

[134] ABAQUS (2011) Dassualt Systèmes. Abaqus documentation. 2011.

[135] T. Schröppel T. Spruegel and S. Wartzack. Generic approach to plausibility checks for structural mechanics with deep learning. 08 2017.

[136] G. Tribello, M. Ceriotti, and M. Parrinello. A self-learning algorithm for biased molecular dynamics. *Proceedings of the National Academy of Sciences of the United States of America*, 107:17509–17514, 01 2010.

[137] E. Ulu, R. Zhang, and L. Kara. A data-driven investigation and estimation of optimal topologies under variable loading configurations. *Computer Methods in Biomechanics and Biomedical Engineering: Imaging & Visualization*, 4:1–12, 08 2015.

[138] N. Umetani. Exploring generative 3d shapes using autoencoder networks. pages 1–4, 11 2017.

[139] P. Wang, S. Zhong, K. Yan, B. Liao, and J. Zhang. Influence of a batch of hollow glass microspheres with different strength grades on the compression strength of syntactic foam. *Composites Science and Technology*, 223:109442, 2022.

[140] Yixin Wang, Jingwen Guo, Yi Fang, Xin Zhang, and Hongyu Yu. Ultralight metamaterial for sound absorption based on miura-ori tessellation structures. *Advanced Engineering Materials*, 23(12):2100563, 2021.

[141] H Wei, S Zhao, Q Rong, and H Bao. Predicting the effective thermal conductivities of composite materials and porous media by machine learning methods. *International Journal of Heat and Mass Transfer*, 127:908–916, 2018.

[142] Zhiyan Y Wei, Zengcai V Guo, Levi Dudte, Haiyi Y Liang, and Lakshminarayanan Mahadevan. Geometric mechanics of periodic pleated origami. *Physical review letters*, 110(21):215501, 2013.

[143] K. Weiss, T. Khoshgoftaar, and D. Wang. A survey of transfer learning. *Journal of Big data*, 3(1):1–40, 2016.

[144] J Whitcomb, G Kondagunta, and K Woo. Boundary effects in woven composites. *Journal of composite materials*, 29(4):507–524, 1995.

[145] J Whitcomb, K Woo, and S Gundapaneni. Macro finite element for analysis of textile composites. *Journal of composite materials*, 28(7):607–618, 1994.

[146] JD Whitcomb. Three-dimensional stress analysis of plain weave composites. *Composite materials: Fatigue and fracture.*, 3:417–438, 1991.

[147] D Whitley. A genetic algorithm tutorial. *Statistics and computing*, 4(2):65–85, 1994.

[148] E. Woldesenbet, N. Gupta, and A. Jadhav. Effects of density and strain rate on properties of syntactic foams. *Journal of Materials Science*, 40(15):4009–4017, 2005.

[149] P. Wriggers. *Nonlinear Finite Element Methods*, volume 4. 01 2008.

[150] G. Xavier and B. Yoshua. Understanding the difficulty of training deep feedforward neural networks. In *In Proceedings of the International Conference on Artificial Intelligence and Statistics (AISTATS'10). Society for Artificial Intelligence and Statistics*, 2010.

[151] L. Xu, J. Ren, C. Liu, and J. Jia. Deep convolutional neural network for image deconvolution. In Z. Ghahramani, M. Welling, C. Cortes, N. D. Lawrence, and K. Q. Weinberger, editors, *Advances in Neural Information Processing Systems 27*, pages 1790–1798. Curran Associates, Inc., 2014.

[152] C. Yang, Y. Kim, S. Ryu, and G.X. Gu. Prediction of composite microstructure stress-strain curves using convolutional neural networks. *Materials & Design*, 189:108509, 2020.

[153] Hiromi Yasuda, Yasuhiro Miyazawa, Efstathios G Charalampidis, Christopher Chong, Panayotis G Kevrekidis, and Jinkyu Yang. Origami-based impact mitigation via rarefaction solitary wave creation. *Science advances*, 5(5):eaau2835, 2019.

[154] Kan Ye and JC Ji. An origami inspired quasi-zero stiffness vibration isolator using a novel truss-spring based stack miura-ori structure. *Mechanical Systems and Signal Processing*, 165:108383, 2022.

[155] R Ying, R He, K Chen, P Eksombatchai, WL Hamilton, and J Leskovec. Graph convolutional neural networks for web-scale recommender systems. In *Proceedings of the 24th ACM SIGKDD international conference on knowledge discovery & data mining*, pages 974–983, 2018.

[156] L Yu, W Zhang, J Wang, and Y Yu. Seqgan: Sequence generative adversarial nets with policy gradient. In *Proceedings of the AAAI conference on artificial intelligence*, volume 31, 2017.

[157] Lin Yuan, Haoyuan Shi, Jiayao Ma, and Zhong You. Quasi-static impact of origami crash boxes with various profiles. *Thin-Walled Structures*, 141:435–446, 2019.

[158] D. Š. Penava Ž. Penava and M. Nakić. Woven fabrics behavior in pure shear. *Journal of Engineered Fibers and Fabrics*, 10(4):155892501501000405, 2015.

[159] Ji Zhang, WANG Changguo, and Lamei Zhang. Deployment of smp miura-ori sheet and its application: Aerodynamic drag and rcs reduction. *Chinese Journal of Aeronautics*, 35(8):121–131, 2022.

[160] L. Zhang, D. Townsend, N. Petrinic, and A. Pellegrino. The dependency of compressive response of epoxy syntactic foam on the strain rate and temperature under rigid confinement. *Composite Structures*, 280:114853, 2022.

[161] W Zhang, R Li, H Deng, L Wang, W Lin, S Ji, and D Shen. Deep convolutional neural networks for multi-modality isointense infant brain image segmentation. *NeuroImage*, 108:214–224, 2015.

[162] Zheng Zhang, Weili Ma, Helong Wu, Huaping Wu, Shaofei Jiang, and Guozhong Chai. A rigid thick miura-ori structure driven by bistable carbon fibre-reinforced polymer cylindrical shell. *Composites Science and Technology*, 167:411–420, 2018.

[163] Zheng Zhang, Huping Zhou, Jingya Ma, Libin Xiong, Shouzhi Ren, Min Sun, Huaping Wu, and Shaofei Jiang. Space deployable bistable composite structures with c-cross section based on machine learning and multi-objective optimization. *Composite Structures*, 297:115983, 2022.

[164] J Zhao, M Mathieu, and Y LeCun. Energy-based generative adversarial network. *arXiv preprint arXiv:1609.03126*, 2016.

[165] Haosu Zhou, Qingfeng Xu, Zhenguo Nie, and Nan Li. A study on using image-based machine learning methods to develop surrogate models of stamp forming simulations. *Journal of Manufacturing Science and Engineering*, 144(2), 2022.

[166] Xiang Zhou, Hai Wang, and Zhong You. Mechanical properties of miura-based folded cores under quasi-static loads. *Thin-Walled Structures*, 82:296–310, 2014.

[167] Yi Zhu and Evgueni T Filipov. Harnessing interpretable machine learning for origami feature design and pattern selection. *arXiv preprint arXiv:2204.07235*, 2022.

[168] N Zulpe and V Pawar. Glcm textural features for brain tumor classification. *International Journal of Computer Science Issues (IJCSI)*, 9(3):354, 2012.